

The Iron Yield of Normal Type II Supernovae

Ó. Rodríguez,^{1*} N. Meza,² J. Pineda-García³ and M. Ramirez³

¹*School of Physics and Astronomy, Tel Aviv University, Tel Aviv 69978, Israel*

²*Department of Physics, University of California, 1 Shields Avenue, Davis, CA 95616, USA*

³*Departamento de Ciencias Físicas, Universidad Andres Bello, Avda. Republica 252, Santiago, Chile*

Accepted XXX. Received YYY; in original form ZZZ

ABSTRACT

We present ^{56}Ni mass estimates for 110 normal Type II supernovae (SNe II), computed here from their luminosity in the radioactive tail. This sample consists of SNe from the literature, with at least three photometric measurements in a single optical band within 95–320 d since explosion. To convert apparent magnitudes to bolometric ones, we compute bolometric corrections (BCs) using 15 SNe in our sample having optical and near-IR photometry, along with three sets of SN II atmosphere models to account for the unobserved flux. We find that the I - and i -band are best suited to estimate luminosities through the BC technique. The ^{56}Ni mass distribution of our SN sample has a minimum and maximum of 0.005 and $0.177 M_{\odot}$, respectively, and a selection-bias-corrected average of $0.037 \pm 0.005 M_{\odot}$. Using the latter value together with iron isotope ratios of two sets of core-collapse (CC) nucleosynthesis models, we calculate a mean iron yield of $0.040 \pm 0.005 M_{\odot}$ for normal SNe II. Combining this result with recent mean ^{56}Ni mass measurements for other CC SN subtypes, we estimate a mean iron yield $< 0.068 M_{\odot}$ for CC SNe, where the contribution of normal SNe II is > 36 per cent. We also find that the empirical relation between ^{56}Ni mass and steepness parameter (S) is poorly suited to measure the ^{56}Ni mass of normal SNe II. Instead, we present a correlation between ^{56}Ni mass, S , and absolute magnitude at 50 d since explosion. The latter allows to measure ^{56}Ni masses of normal SNe II with a precision around 30 per cent.

Key words: supernovae: general – nuclear reactions, nucleosynthesis, abundances

1 INTRODUCTION

Supernovae (SNe) explosions are important astrophysical objects for a wide range of research fields. Among them we mention their use to measure distances and cosmological parameters, their connection with stellar evolution, and their contribution to the energetics and chemical enrichment of the interstellar medium. Indeed, regarding the latter, SNe synthesize the bulk of all the mass in the Universe residing in elements from oxygen to the iron group. Therefore, to understand chemical evolution, it is critical to determine how much elements are produced by every kind of SN: Type Ia and core-collapse (CC) SNe (see [Hoefflich 2017](#) and [Burrows & Vartanyan 2021](#) for current reviews of their explosion mechanisms). In the case of CC SNe, almost all α -elements have been produced in those explosions, while their contribution to the cosmic iron budget is comparable to that of SNe Ia (e.g. [Maoz & Graur 2017](#)).

CC SNe are grouped into two classes: H-rich envelope SNe, historically known as Type II SNe (SNe II,

[Minkowski 1941](#)), and stripped-envelope (SE) SNe. The latter group includes H-poor Type IIb and H-free Type Ib, Ic, and broad-line Ic (Ic-BL) SNe (see [Gal-Yam 2017](#) for a current review of the SN classification). Among SNe II, some events are grouped into subtypes based on spectral and photometric characteristics: those showing narrow H emission lines in the spectra, indicative of ejecta-circumstellar material interaction (SNe IIn; [Schlegel 1990](#))¹, and those having long-rising light curves similar to SN 1987A ([Hamuy et al. 1988](#); [Taddia et al. 2016](#)); while a few SNe II are recognized as having peculiar characteristics (e.g. OGLE14-073, [Terreran et al. 2017](#); iPTF14hls, [Arcavi et al. 2017](#); ASASSN-15nx, [Bose et al. 2018](#); DES16C3cje, [Gutiérrez et al. 2020](#); SN 2018ivc, [Bostroem et al. 2020](#)). For the rest of SNe II (about 90 per cent, e.g. [Shivvers et al. 2017](#)), in order not to use the same name of the class that contains other SN II subtypes and peculiar events, we will refer as normal

¹ In this group we also include SNe IIn/II and LLEV SNe II, described in [Rodríguez et al. \(2020\)](#).

* E-mail: olrodrig@gmail.com

SNe II. The latter are found to form a continuum group² (e.g. Anderson et al. 2014; Sanders et al. 2015; Valenti et al. 2016; Gutiérrez et al. 2017b; de Jaeger et al. 2019), where the photometric and spectroscopic diversity depends mainly on the amount of H in the envelope at the moment of the explosion, the synthesized ^{56}Ni mass ($M_{56\text{Ni}}$), and the explosion energy (e.g. Gutiérrez et al. 2017b).

Progenitors of normal SNe II have been directly detected on pre-explosion images. They correspond to red supergiant (RSG) stars with zero-age main-sequence (ZAMS) mass, M_{ZAMS} , in the range 8–18 M_{\odot} (e.g. Smartt 2009, 2015). In the case of SE SNe, evidence points toward progenitors with M_{ZAMS} similar to those of normal SNe II but evolving in binary systems, and some cases with a more massive and isolated progenitor (e.g. Anderson 2019 and references therein). The ^{56}Ni mass produced by CC SNe depends on the explosion properties and the core structure of the progenitor (e.g. Suwa et al. 2019). Therefore, $M_{56\text{Ni}}$ estimates are important to contrast the progenitor scenarios and explosion mechanisms of different CC SNe. The mean ^{56}Ni mass ($\langle M_{56\text{Ni}} \rangle$) of normal SNe II is lower than that of SE SNe (e.g. Anderson 2019; Meza & Anderson 2020). On the other hand, normal SNe II account for around 60 per cent of all CC SNe in a volume-limited sample (e.g. Shivvers et al. 2017). The latter makes normal SNe II significant contributors to the ^{56}Ni and iron budget of CC SNe (e.g. see Section 4.4).

Normal SNe II are characterized by having an optically thick photosphere during the first 60–120 d after the explosion (e.g. Anderson et al. 2014; Faran et al. 2014a; Sanders et al. 2015; de Jaeger et al. 2019). In this so-called photospheric phase, the V -band absolute magnitudes (M_V) range between around -14.5 and -18.5 mag (e.g. Anderson et al. 2014; de Jaeger et al. 2019). In particular, normal SNe II having $M_V \gtrsim -15.5$ mag are referred as sub-luminous SNe II (e.g. Pastorello et al. 2004; Spiro et al. 2014), while those having $M_V \lesssim -17$ mag are referred as moderately-luminous SNe II (e.g. Inserra et al. 2013). The aforementioned phase is also characterized by a period of 30–70 d where the V -band magnitude remains nearly constant or declines linearly with time (e.g. Anderson et al. 2014). During this period, called plateau phase, light curves are powered by H recombination. Then, the brightness decreases by around 1.0–3.5 mag in a lapse of about 15–30 d, indicating that all H has recombined. After this transition phase, the luminosity starts to decrease exponentially with time. In this phase, the energy sources are the γ -rays and positrons produced by the radioactive decay of the unstable cobalt isotope ^{56}Co (daughter of the unstable nickel isotope ^{56}Ni) into the stable iron isotope ^{56}Fe (e.g. Weaver & Woosley 1980). Therefore the luminosity in this phase, called radioactive tail, is a good estimate of the ^{56}Ni mass ejected in the explosion.

The luminosity is given by the inverse-square law of light and the bolometric flux. The latter can be computed through the direct integration technique (e.g. Lusk & Baron 2017). In this method, the available x -band magnitudes are converted to monochromatic fluxes (\bar{f}_x) and associated

to x -band effective wavelengths ($\bar{\lambda}_x$). The set of ($\bar{\lambda}_x, \bar{f}_x$) points defines the photometric spectral energy distribution (pSED) which, integrated over wavelength, provides the quasi-bolometric flux. For normal SNe II in the radioactive tail, the quasi-bolometric flux in the wavelength range 0.46–2.16 μm typically accounts for 90 per cent of the bolometric flux (e.g. see Section 3.3). To estimate the unobserved flux, some authors extrapolate fluxes assuming a Planck function (e.g. Hamuy 2001; Pejcha & Prieto 2015a), while others do not include the unobserved flux in the bolometric flux (e.g. Bersten & Hamuy 2009; Maguire et al. 2010). In practice, the application of the direct integration technique is limited because the low number of normal SNe II with IR photometry during the radioactive tail.

An alternative method to compute bolometric fluxes for SNe without IR photometry is the bolometric correction (BC) technique (e.g. Lusk & Baron 2017). In this method, the magnitude in a given band (m_x) is related to the bolometric magnitude (m_{bol}) through $m_{\text{bol}} = m_x + \text{BC}_x$. Here, BC_x is calibrated using SNe with m_{bol} computed with the direct integration technique. Based on the *BVIJHK* photometry of the normal SN II 1999em and the long-rising SN 1987A, Hamuy (2001) reported a constant BC_V for SNe II in the radioactive tail. Similar constant BC_V values were later reported by other authors (e.g. Bersten & Hamuy 2009; Maguire et al. 2010; Pejcha & Prieto 2015a).

The two main weaknesses in the BC_V values reported in previous works are: (1) not accounting for the unobserved flux or assuming a Planck function to estimate it, and (2) the low number of SNe used to compute BC_V . At present, thanks to the development of non-local thermodynamic equilibrium (non-LTE) radiative transfer codes (e.g. Dessart & Hillier 2011; Jerkstrand et al. 2011), it is possible to estimate the flux outside the optical/near-IR range for normal SNe II through theoretical spectral models. From the observational side, the number of normal SNe II observed during the radioactive tail with optical and near-IR filters had increased over time. Therefore, it is possible to improve the BC determination with the current available data.

The goal of this work is to estimate the mean iron yield (\bar{y}_{Fe}) of normal SNe II. For this, we use all normal SNe II in the literature with useful photometry during the radioactive tail. To improve the determination of the radioactive tail luminosity through the BC technique, we also aim to enhance the BC calibration. The paper is organized as follows. In Section 2 we outline the relevant information on the data we use. The methodology to compute BCs, ^{56}Ni and iron masses is described in Section 3. In Section 4 we present new BC calibrations, the $M_{56\text{Ni}}$ distribution of our SN sample, the $\langle M_{56\text{Ni}} \rangle$ and \bar{y}_{Fe} values for normal SNe II, and a new method to estimate $M_{56\text{Ni}}$. Comparisons with previous works, discussions about systematics, and future improvements are in Section 5. Finally, our conclusions are summarized in Section 6.

2 DATA SET

2.1 Supernova sample

For this work we select normal SNe II from the literature, having photometry in the radioactive tail (1) in at least one

² Some authors, however, suggest a separation into distinct groups (e.g. Arcavi et al. 2012; Faran et al. 2014b).

of the following bands: Johnson–Kron–Cousins *VRI* or Sloan *ri*; (2) in the range 95–320 d since the explosion, corresponding to the time range where our BC calibrations are valid (Section 4.2.2); and (3) with at least 3 photometric epochs in order to detect possible γ -ray leakage from the ejecta (Section 3.4). The final sample of 110 normal SNe II fulfilling our selection criteria is listed in Table L1. This includes the SN name (Column 1), the host galaxy name (Column 2), the Galactic colour excess E_{B-V}^G (Column 3), the heliocentric SN redshift $z_{\text{helio}}^{\text{SN}}$ (Column 4), the distance modulus (Column 5, see Section 3.6.1), the host galaxy colour excess E_{B-V}^h (Column 6, see Section 3.6.2), the explosion epoch t_0 (Column 7, see Section 3.7) and the references for the photometry (Column 8). Among the SNe in our set, 15 have *BV(r)R(i)IJHK* photometry in the radioactive tail. We use the latter sample to compute bolometric fluxes and BCs. Galactic colour excesses are taken from Schlafly & Finkbeiner (2011) (except for SN 2002hh, see Section 3.6.2), which have associated a random error of 16 per cent (Schlegel et al. 1998). Throughout this work, for our Galaxy and host galaxies, we assume the extinction curve given by Fitzpatrick (1999) with $R_V = 3.1$ (except for SN 2002hh, see Section 3.6.2).

2.2 Theoretical models

We use SN II atmosphere models to compute the contribution of the flux at $\lambda < \bar{\lambda}_B$ and $\lambda > \bar{\lambda}_K$ to the bolometric one. We also employ CC nucleosynthesis models to estimate the contribution of iron stable isotopes other than ^{56}Fe to the total ejected iron mass (M_{Fe}). Among the available models from the literature, we select those using progenitors of $M_{\text{ZAMS}} \leq 18 M_{\odot}$ to be consistent with observations of normal SNe II (e.g. Smartt 2009, 2015). Those models were exploded with energies $\sim 10^{50}$ – 10^{51} erg, corresponding to the typical range for normal SNe II (e.g. Förster et al. 2018; Morozova et al. 2018). The ^{56}Ni masses of the selected models range between 0.003 and $0.12 M_{\odot}$ which is consistent with observations of normal SNe II (e.g. Müller et al. 2017).

2.2.1 Atmosphere models

We use the SN II atmosphere model sets given by Dessart et al. (2013, hereafter D13), Jerkstrand et al. (2014, hereafter J14), and Lisakov et al. (2017, hereafter L17). Those models were generated evolving ZAMS stars with $M_{\text{ZAMS}} \geq 12 M_{\odot}$ until the RSG stage before the CC. The explosions were simulated using a piston, while the spectra were computed through 1D non-LTE radiative transfer codes. In particular, L17 used the same methodology as D13 but with different progenitors and explosion energies.

The selected D13 set consists on six models (8–11 spectra each) with $M_{\text{ZAMS}} = 15 M_{\odot}$ and $M_{56\text{Ni}} = 0.036$ – $0.121 M_{\odot}$. The selected J14 set consists on three models (3–5 spectra each) with M_{ZAMS} of 12, 15, and $19 M_{\odot}$, and $M_{56\text{Ni}} = 0.062 M_{\odot}$. The selected L17 set consists on seven models (9–10 spectra each) with $M_{\text{ZAMS}} = 12 M_{\odot}$, and $M_{56\text{Ni}} = 0.007$ – $0.010 M_{\odot}$.

2.2.2 Nucleosynthesis yields

We use the 1D CC nucleosynthesis yields presented in Kobayashi et al. (2006, hereafter K06) and Sukhbold et al. (2016, hereafter S16), which are updated versions of the works of Nomoto et al. (1997) and Woosley & Weaver (1995), respectively. The selected K06 models were calibrated to be consistent with observations of normal SNe II, where the yields are estimated using a mass cut such that $M_{\text{Fe}} \sim 0.07 M_{\odot}$. The S16 models were calibrated to be consistent with the Crab SN (for $M_{\text{ZAMS}} \leq 12 M_{\odot}$) and SN 1987A (for $M_{\text{ZAMS}} > 12 M_{\odot}$), while the yields were estimated using the “special trajectory” to represent the mass cut (see S16 for more details).

The selected K06 set consists on 12 models with M_{ZAMS} of 13, 15, and $18 M_{\odot}$, and $M_{56\text{Ni}} = 0.07$ – $0.09 M_{\odot}$. The selected S16 set consist on 13 models with $M_{\text{ZAMS}} = 9$ – $12 M_{\odot}$ and $M_{56\text{Ni}} = 0.003$ – $0.03 M_{\odot}$, and 89 models with M_{ZAMS} between 12 and $18 M_{\odot}$ and $M_{56\text{Ni}} = 0.05$ – $0.09 M_{\odot}$.

3 METHODOLOGY

3.1 Light-curve interpolation

To compute bolometric fluxes and BCs, we first need to evaluate the *BV(r)R(i)IJHK* photometry of the 15 SNe in the calibration sample at the same set of epochs $\{t_i\}$. To determine these epochs, for each band we select the epochs covered simultaneously by the photometry in the other bands. Then, we adopt the epochs of the band with less observations as $\{t_i\}$. If the rest of bands do not have photometry at the t_i epochs, then we interpolate them using the ALR code³ (Rodríguez et al. 2019). The ALR performs loess non-parametric regressions (Cleveland et al. 1992) to the input photometry, taking into account observed and intrinsic errors, along with the presence of possible outliers. If the ALR is not able to perform a loess fit (e.g. only few data points are available), then the ALR just performs a linear interpolation between points. In the case of SN 1995ad, we extrapolate the *BI* photometry to the epoch of the *JHK* photometry using a straight-line fit. Fig. 1 shows the result of this process.

3.2 Quasi-bolometric correction

In the BC calibration sample, only 6 out of 15 SNe have *ri* photometry. Therefore, we only use the *BVRIJHK* photometry in order to compute quasi-bolometric fluxes with an homogeneous data set. We construct pSEDs and compute quasi-bolometric fluxes F_i^{BVRJHK} (in $\text{erg s}^{-1} \text{cm}^{-2}$) using the prescription provided in Appendix B. We define the *x*-band quasi BC (qBC) as

$$\text{qBC}_{x,i} = -2.5 \log(F_i^{BVRJHK}) - m_{x,i}^{\text{cor}}, \quad (1)$$

where

$$m_{x,i}^{\text{cor}} = m_{x,i} - R_{\bar{\lambda}_x}(E_{B-V}^G + E_{B-V}^h), \quad (2)$$

being $m_{x,i}$ the *x*-band magnitude at epoch t_i , and $R_{\bar{\lambda}_x}$ the total-to-selective extinction ratio for $\bar{\lambda}_x$, listed in Table A1.

³ <https://github.com/olrodrig/ALR>

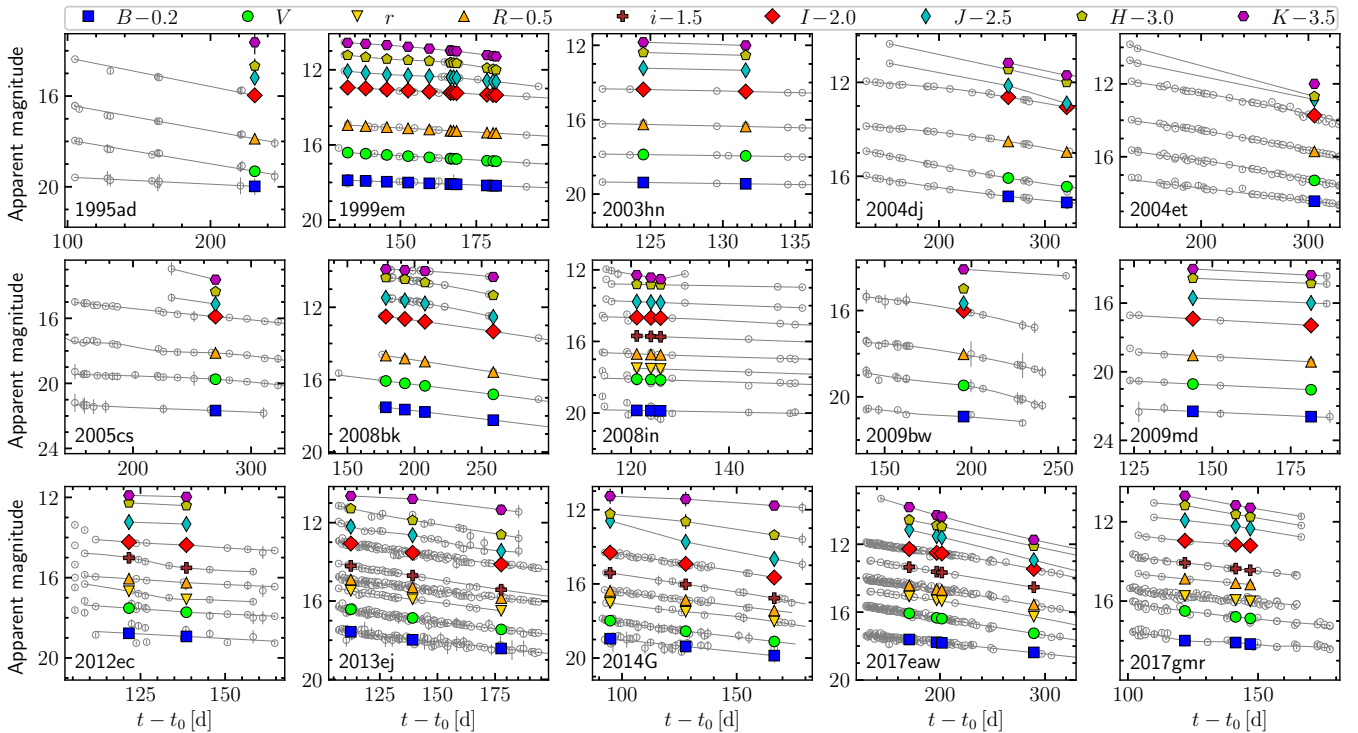


Figure 1. Light curves of the 15 SNe in the BC calibration sample. Colour-filled symbols correspond to the interpolated photometry, where bands and magnitude shifts with respect to the original values are indicated in the legend. Grey empty circles correspond to the photometry from the literature, and grey lines are the light-curve fits.

3.3 Bolometric correction and luminosity

The flux from a pSED defined in a wavelength range λ_1 – λ_2 is only an approximation of the real flux computed integrating the SED in the same wavelength range, $F_i^{\lambda_1-\lambda_2}$. In our case, to quantify the relative difference between $F_i^{BVRJIHK}$ and $F_i^{\lambda_B-\lambda_K}$, we compute α_i such that

$$F_i^{\lambda_B-\lambda_K} = (1 + \alpha_i) F_i^{BVRJIHK}. \quad (3)$$

For this task we use the **D13**, **J14**, and **L17** spectral models. To obtain $F_i^{BVRJIHK}$ from models, we first compute their synthetic magnitudes (see Appendix A) and then we compute $F_i^{BVRJIHK}$ with the recipe given in Appendix B.

Fig. 2 shows the α_i values computed with the three model sets. Since we do not find any correlation with colour indices, in the figure we plot α_i as a function of the time since explosion. For the **D13**, **J14**, and **L17** models, the mean α values and their sample standard deviation ($\hat{\sigma}$) errors are -3.2 ± 1.8 , 4.6 ± 3.0 , and 1.1 ± 1.4 per cent, respectively. There is a difference of at least $2.6 \hat{\sigma}$ between the mean α values from **D13** and **J14** models. Based on late-time optical spectra of 38 normal SNe II, [Silverman et al. \(2017\)](#) found that the **J14** models fit better to the observations than the **D13** ones. This evidence favour the scenario where $F_i^{\lambda_B-\lambda_K}$ is ~ 5 per cent greater than $F_i^{BVRJIHK}$ instead of ~ 3 per cent lower. To be conservative, we adopt the average of the mean α values of the three models, i.e., $\alpha = 0.8 \pm 3.9$ per cent ($1 \hat{\sigma}$ error). This value is consistent within $\pm 1 \hat{\sigma}$ with the results obtained for the three model sets.

To compute the bolometric flux F^{bol} , we have to correct

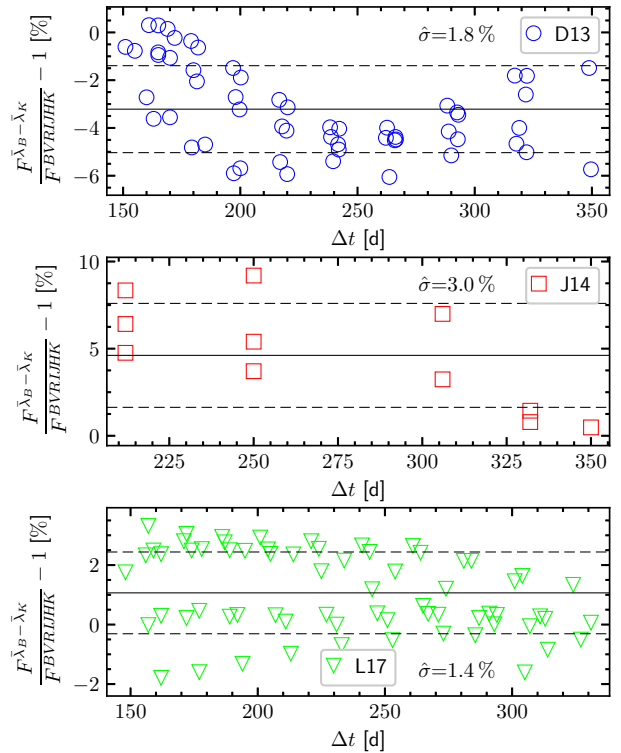


Figure 2. Relative differences between the flux computed with the pSED and the SED using the **D13** (top panel), **J14** (middle panel), and **L17** (bottom panel) models. Solid and dashed lines correspond to mean values and $\pm 1 \hat{\sigma}$ limits, respectively.

Table 1. Parameters for the flux corrections.

Correction	Colour	a_0 (%)	a_1 (%)	a_2 (%)	$\hat{\sigma}$ (%)
α	–	0.80	–	–	3.90
$c^{\lambda < \bar{\lambda}_B}$	$B - V$	-3.11	4.30	6.72	0.59
$c^{\bar{\lambda}_K - 2.48\mu\text{m}}$	$V - K$	0.32	0.55	–	0.23
$c^{2.48 - 3.0\mu\text{m}}$	$V - K$	0.31	1.09	-0.14	0.19
$c^{\lambda > 3\mu\text{m}}$	$V - K$	1.87	0.52	–	0.24
$c^{\lambda > \bar{\lambda}_K}$	$V - K$	2.50	2.16	-0.14	0.38

Note: $c^{\lambda > \bar{\lambda}_K} = c^{\bar{\lambda}_K - 2.48\mu\text{m}} + c^{2.48 - 3.0\mu\text{m}} + c^{\lambda > 3\mu\text{m}}$.

$F_i^{\bar{\lambda}_B - \bar{\lambda}_K}$ for the unobserved flux. In our case,

$$F_i^{\text{bol}} = F_i^{\bar{\lambda}_B - \bar{\lambda}_K} + F_i^{\lambda < \bar{\lambda}_B} + F_i^{\lambda > \bar{\lambda}_K}, \quad (4)$$

where $F_i^{\lambda < \bar{\lambda}_B}$ and $F_i^{\lambda > \bar{\lambda}_K}$ are the unobserved fluxes at wavelengths below $\bar{\lambda}_B$ and beyond $\bar{\lambda}_K$, respectively.

For the unobserved flux below $\bar{\lambda}_B$, we write

$$F_i^{\lambda < \bar{\lambda}_B} = F_i^{\bar{\lambda}_B - \bar{\lambda}_K} c_i^{\lambda < \bar{\lambda}_B}, \quad (5)$$

where

$$c_i^{\lambda < \bar{\lambda}_B} = F_i^{0.1\mu\text{m} - \bar{\lambda}_B} / F_i^{\bar{\lambda}_B - \bar{\lambda}_K} \quad (6)$$

is the flux correction relative to $F_i^{\bar{\lambda}_B - \bar{\lambda}_K}$. We choose $0.1\mu\text{m}$ as lower λ value because it is the minimum wavelength in common for the three model sets. This value is also low enough to consider the flux negligible at shorter wavelengths.

Fig. 3(a) shows the $c_i^{\lambda < \bar{\lambda}_B}$ values as a function of $B - V$. As visible in the figure, there is a correlation between both quantities. The flux correction is lower than 2 per cent for $B - V > 1.7$ and can be greater than 10 per cent for $B - V < 0.9$. Within the colour range in common between the **D13**, **J14**, and **L17** models ($1.0 \leq B - V \leq 1.45$), we see that values for the three model sets are in good agreement. We parametrize the dependence of $c_i^{\lambda < \bar{\lambda}_B}$ on $B - V$ as

$$c_i^{\lambda < \bar{\lambda}_B} = \sum_{j=0}^2 \frac{a_j}{(B - V)_i^j}, \quad (7)$$

where the quadratic order was determined using the model selection described in Appendix C. Table 1 lists the fit parameters along with the $\hat{\sigma}$ around the fit, which covers the colour range $0.79 \leq B - V \leq 2.02$. Among the $B - V$ colours of the SNe in our BC calibration set (marked as magenta ticks in the figure), four are below the lower limit (two of SN 2014G, one of SN 1995ad, and one of SN 2004dj). In order to prevent a misestimation on $c_i^{\lambda < \bar{\lambda}_B}$ due to extrapolations, for $B - V$ colours bluer than 0.79 mag we adopt the $c^{\lambda < \bar{\lambda}_B}$ correction for $B - V = 0.79$.

For the unobserved flux at $\lambda > \bar{\lambda}_K$ we use

$$F_i^{\lambda > \bar{\lambda}_K} = F_i^{\bar{\lambda}_B - \bar{\lambda}_K} c_i^{\lambda > \bar{\lambda}_K}, \quad (8)$$

where, since the model sets do not cover the same wavelength range, we write

$$c_i^{\lambda > \bar{\lambda}_K} = c_i^{\bar{\lambda}_K - 2.48\mu\text{m}} + c_i^{2.48 - 3.0\mu\text{m}} + c_i^{\lambda > 3\mu\text{m}}, \quad (9)$$

being

$$c_i^{\bar{\lambda}_K - 2.48\mu\text{m}} = F_i^{\bar{\lambda}_K - 2.48\mu\text{m}} / F_i^{\bar{\lambda}_B - \bar{\lambda}_K}, \quad (10)$$

$$c_i^{2.48 - 3.0\mu\text{m}} = F_i^{2.48 - 3.0\mu\text{m}} / F_i^{\bar{\lambda}_B - \bar{\lambda}_K}, \quad (11)$$

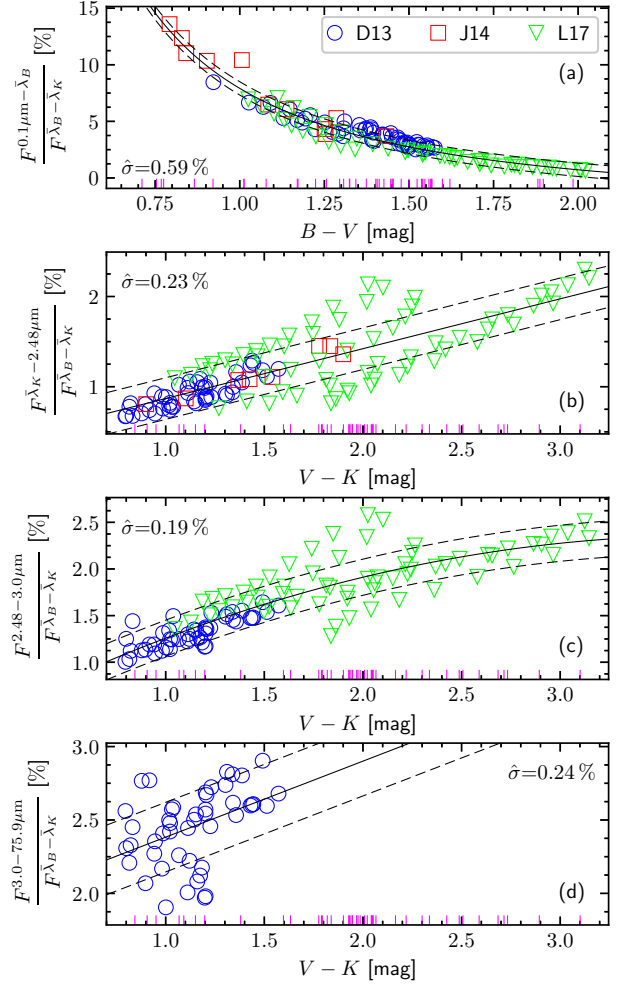


Figure 3. Corrections to account for the unobserved flux in the ranges $0.1\mu\text{m} - \bar{\lambda}_B$ (a), $\bar{\lambda}_K - 2.48\mu\text{m}$ (b), $2.48 - 3.0\mu\text{m}$ (c), and $3.0 - 75.9\mu\text{m}$ (d), relative to the flux in the range $\bar{\lambda}_B - \bar{\lambda}_K$, using the **D13**, **J14**, and **L17** models. Magenta ticks mark the colours of the SNe in the BC calibration set. Solid lines indicate the fits to the models, while dashed lines are the $\pm 1\hat{\sigma}$ limits around the fit.

and

$$c_i^{\lambda > 3\mu\text{m}} = F_i^{3.0 - 75.9\mu\text{m}} / F_i^{\bar{\lambda}_B - \bar{\lambda}_K}. \quad (12)$$

Here, the values 2.48 and $3.0\mu\text{m}$ correspond to the maximum λ in common for the **{D13, J14, L17}** and **{D13, L17}** model sets, respectively, while $75.9\mu\text{m}$ is the maximum λ for the **D13** models.

Figs. 3(b) and 3(c) show $c_i^{\bar{\lambda}_K - 2.48\mu\text{m}}$ and $c_i^{2.48 - 3.0\mu\text{m}}$, respectively, as a function of $V - K$. Those flux corrections, as expected, are greater for red colours than for blue ones. We express the dependence of $c_i^{\bar{\lambda}_K - 2.48\mu\text{m}}$ and $c_i^{2.48 - 3.0\mu\text{m}}$ on $V - K$ through polynomials, i.e.,

$$c_i^{\lambda_1 - \lambda_2} = \sum_{j=0}^{\mathcal{O}_{\lambda_1, \lambda_2}} a_j (V - K)_i^j, \quad (13)$$

being the orders $\mathcal{O}_{\lambda_1, \lambda_2}$ determined with the model selection described in Appendix C. The fit parameter values are summarized in Table 1. As in the case of $c_i^{\lambda < \bar{\lambda}_B}$, we find a good agreement between models within the ranges in common.

Fig. 3(d) shows the $c_i^{\lambda > 3\mu\text{m}}$ values as a function of

$V-K$, where only the **D13** models provide spectral information for $\lambda > 3\ \mu\text{m}$. In this case the best fit is a straight-line, whose parameters are reported in Table 1. Since the **D13** models do not cover all the $V-K$ colours of the SNe in the BC calibration set, the straight-line fit could introduce errors due to extrapolation. However, we find that $c_i^{\lambda > 3\ \mu\text{m}}$ at $V-K = 3.1$ (the reddest colour in the BC calibration set) is only 1 per cent (in value) greater than the correction for the reddest colour in the **D13** models ($V-K = 1.57$). Therefore, we adopt the linear parametrization of $c_i^{\lambda > 3\ \mu\text{m}}$ for all the $V-K$ colour range ($0.80 \leq V-K \leq 3.15$).

Based on equation (9), $c_i^{\lambda > \bar{\lambda}_K}$ is a polynomial given by equation (13), where the coefficients a_j are the sum of those of $c_i^{\bar{\lambda}_K - 2.48\ \mu\text{m}}$, $c_i^{2.48 - 3.0\ \mu\text{m}}$, and $c_i^{\lambda > 3\ \mu\text{m}}$. Parameters for $c_i^{\lambda > \bar{\lambda}_K}$ are given in Table 1.

Once α , $c_i^{\lambda < \bar{\lambda}_B}$, and $c_i^{\lambda > \bar{\lambda}_K}$ are determined, we define the apparent bolometric magnitude and the x -band BC as

$$m_{\text{bol},i} = -2.5 \log(F_i^{\text{BVRILJHK}}) - \kappa_i \quad (14)$$

and

$$\text{BC}_{x,i} = m_{\text{bol},i} - m_{x,i}^{\text{cor}} = \text{qBC}_{x,i} - \kappa_i, \quad (15)$$

respectively. The model-based correction, κ_i , is given by

$$\kappa_i = 2.5 \log(1 + \alpha) + 2.5 \log\left(1 + c_i^{\lambda < \bar{\lambda}_B} + c_i^{\lambda > \bar{\lambda}_K}\right), \quad (16)$$

where the error in κ_i is dominated by the error in α (see Table 1). For the SNe in the BC calibration set, the model-based correction ranges between 0.09 mag (SN 2005cs) and 0.22 mag (SN 2014G), with a median of 0.11 mag. Therefore, during the radioactive tail, the observed F^{BVRILJHK} typically corresponds to 90 per cent of the bolometric flux.

Once BC_x values are calibrated with observations (section 4.2), luminosities (L , in $10^{43}\ \text{erg s}^{-1}$) can be estimated through the BC technique, given by

$$\log L_i = (\mu - \text{BC}_{x,i} - m_{x,i}^{\text{cor}})/2.5 - 2.922, \quad (17)$$

where the constant provides the conversion from magnitude to cgs units.

3.4 ^{56}Ni Mass

During the radioactive tail, the energy sources powering the ejecta are the γ -rays and positrons produced in the radioactive decay of ^{56}Co into ^{56}Fe . The latter deposit energy in the ejecta at a rate Q_{dep} . Using equations (10)–(12) of Wygoda et al. (2019), and assuming that the deposited energy is immediately emitted, we can write the relation between Q_{dep} (in $10^{43}\ \text{erg s}^{-1}$) and $M_{56\text{Ni}}$ (in M_{\odot}) as

$$\log Q_{\text{dep},i} = \log M_{56\text{Ni}} - 0.39 \left[\frac{\Delta t_i}{100\ \text{d}} \right] + 0.154 + D_i. \quad (18)$$

Here, $\Delta t_i = (t_i - t_0)/(1 + z_{\text{helio}}^{\text{SN}})$ is the time since explosion in the SN rest frame, and

$$D_i = \log(0.97f_{\text{dep},i} + 0.03), \quad (19)$$

where f_{dep} is the γ -ray deposition function, which describes the fraction of the generated γ -ray energy deposited in the ejecta. Knowing the deposition function, $\log M_{56\text{Ni}}$ can be inferred by equating equations (17) and (18).

If all the γ -ray energy is deposited in the ejecta, then

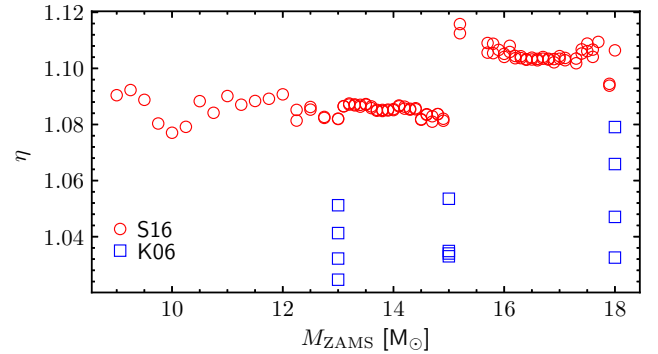


Figure 4. $M_{\text{Fe}}/M_{56\text{Fe}}$ against M_{ZAMS} . Blue squares and red circles correspond to **K06** and **S16** models, respectively.

$f_{\text{dep},i} = 1$ ($D_i = 0$), otherwise $f_{\text{dep},i} < 1$ ($D_i < 0$). In the first case, we expect the $\log M_{56\text{Ni}}$ estimates (one for each $\log L_i$ measurement) to be consistent with a constant value. In the second case, the $\log M_{56\text{Ni}}$ estimates decrease with time as the ejecta becomes less able to thermalize γ -rays (Section 4.3.1), which makes it necessary to correct for f_{dep} . For the latter we adopt the model of Jeffery (1999):

$$f_{\text{dep},i} = 1 - \exp[-(T_0/\Delta t_i)^2], \quad (20)$$

where T_0 is a characteristic time-scale (in d) that represents the γ -ray escape time. This parameter is estimated such that the $\log M_{56\text{Ni}}$ estimates are consistent with a constant value.

To detect possible γ -ray leakage from the ejecta, we need at least three photometric points as we have to infer T_0 and $\log M_{56\text{Ni}}$. The detailed recipe to compute $\log M_{56\text{Ni}}$ and check if it is necessary to correct for f_{dep} is provided in Appendix D⁴. In order to properly convert $\log M_{56\text{Ni}}$ into $M_{56\text{Ni}}$, we use the formalism provided in Appendix E.

3.5 Iron mass

The inferred $M_{56\text{Ni}}$ provides a good estimate of the ejected ^{56}Fe mass ($M_{56\text{Fe}}$). The M_{Fe} value, however, is greater than $M_{56\text{Fe}}$ since it is also composed of the stable isotopes $^{54,57,58}\text{Fe}$ (e.g. Curtis et al. 2019). Using the relation

$$\eta = M_{\text{Fe}}/M_{56\text{Ni}} = 1 + M_{54,57,58\text{Fe}}/M_{56\text{Fe}} \quad (21)$$

and the CC nucleosynthesis yield models of Iwamoto et al. (1999), Blanc & Greggio (2008) computed $\eta = 1.08$.

Fig. 4 shows the η values obtained with the **K06** and **S16** models. Since we do not find any correlation with model parameters, in the figure we plot η against M_{ZAMS} . The η values range between 1.03 and 1.11, where the **S16** values for $M_{\text{ZAMS}} \leq 15 M_{\odot}$ are around 0.02 lower than those for $M_{\text{ZAMS}} > 15 M_{\odot}$. The η values computed with the **K06** models are up to 0.06 lower than those from **S16** models. Since neither model is preferred, to be conservative we adopt $\eta = 1.07 \pm 0.04$ (the mid-point between 1.03 and 1.11, with the error being half the range). This value, consistent with that reported in Blanc & Greggio (2008), indicates that the measured $M_{56\text{Ni}}$ accounts to about 93 per cent of M_{Fe} .

⁴ The code implementing this algorithm (`SNII_nickel`) is available at https://github.com/olrodrig/SNII_nickel.

3.6 Host galaxy distance moduli and colour excesses

The error on $\log M_{56\text{Ni}}$ is mainly dominated by uncertainties on μ and E_{B-V}^h (e.g. [Pejcha & Prieto 2015b](#)). To reduce their errors, we measure μ and E_{B-V}^h with various methods.

3.6.1 Distance moduli

To estimate μ for the SN host galaxies, we use distance moduli obtained with the Cepheids period-luminosity relation (μ_{CPL}), the Tip of the Red Giant Branch method (μ_{TRGB}), and the Tully-Fisher relation (μ_{TF}). We compile μ_{CPL} and μ_{TRGB} values from the literature, and μ_{TF} from the Extragalactic Distance Database⁵ (EDD, [Tully et al. 2009](#)). If a host galaxy does not have μ_{CPL} nor μ_{TRGB} , then we include distances (1) computed with the Hubble-Lemaître law (D_{HLL}) using a local Hubble-Lemaître constant (H_0) of $74.03 \pm 1.42 \text{ km s}^{-1} \text{ Mpc}^{-1}$ ([Riess et al. 2019](#)) and including a velocity dispersion of 382 km s^{-1} to account for the effect of peculiar velocities over D_{HLL} ; and (2) from distance-velocity calculators based on smoothed velocity fields (D_{SVF}) given by [Shaya et al. \(2017\)](#) for $D_{\text{SVF}} < 38 \text{ Mpc}$ and [Graziani et al. \(2019\)](#) for $D_{\text{SVF}} < 200 \text{ Mpc}$. These calculators are available on the EDD website⁵ and described in [Kourkchi et al. \(2020\)](#). Since the latter do not provide distance uncertainties, we adopt the typical distance error of the neighbouring galaxies as a conservative estimate, or a 15 per cent error if the host galaxy is isolated (Ehsan Kourkchi, private communication). We convert D_{HLL} (D_{SVF}) into μ_{HLL} (μ_{SVF}) using the recipe provided in Appendix E.

Table L2 summarizes the aforementioned distance moduli. From this compilation, we adopt as μ the weighted average of μ_{CPL} , μ_{TRGB} , and μ_{TF} , if the first ones are available, otherwise we adopt the weighted average of μ_{TF} , μ_{HLL} , and μ_{SVF} . In the case of SN 2006my, whose host galaxy is within the Virgo Cluster, we include the distance modulus reported in [Foster et al. \(2014\)](#) based on the planetary nebula luminosity function. The μ values are in Column 5 of Table L1. The typical μ error is of 0.18 mag.

3.6.2 Colour excesses

To calculate E_{B-V}^h we use the following methods:

1. The colour-colour curve (C3) method ([Rodríguez et al. 2014, 2019](#)). This technique assumes that, during the plateau phase, all normal SNe II have similar linear $V-I$ versus $B-V$ C3s. Under this assumption, the E_{B-V}^h value of an SN can be inferred from the vertical displacement of its observed C3 with respect to a reddening-free C3 (for a graphical representation, see Fig. 3 of [Rodríguez et al. 2014](#)). Using the C3 method (Appendix F), implemented in the C3M code⁶, we measure the colour excesses ($E_{B-V}^{\text{h,C3}}$) of 71 SNe in our set. Those values are reported in Column 2 of Table L3. The typical $E_{B-V}^{\text{h,C3}}$ uncertainty is of 0.085 mag.

2. The colour method (e.g. [Olivares E. et al. 2010](#)). This technique assumes that all normal SNe II have the same intrinsic $V-I$ colour at the end of the plateau phase.

[Olivares E. et al. \(2010\)](#) defined this epoch as 30 d before the middle of the V -band transition phase ($t_{\text{PT},V}$, see Section 4.5). The prescription provided by [Olivares E. et al. \(2010\)](#) to compute colour excesses can be written as

$$E_{B-V}^{\text{h},V-I} = 0.812[(V-I)_{-30} - 0.656], \quad (22)$$

$$\sigma_{E_{B-V}^{\text{h},V-I}} = 0.812\sqrt{\sigma_{(V-I)_{-30}}^2 + 0.079^2}. \quad (23)$$

Here, $(V-I)_{-30}$ is the $V-I$ colour measured at $t_{\text{PT},V} - 30$ d corrected for E_{B-V}^G and K -correction (e.g. [Rodríguez et al. 2019](#)). We compute $E_{B-V}^{\text{h},V-I}$ values for 59 SNe in our sample. For SNe 2012aw and 2013am we adopt the values provided in the literature. Column 3 of Table L3 lists the $E_{B-V}^{\text{h},V-I}$ values, which have a typical uncertainty of 0.074 mag.

3. Spectrum-fitting method (e.g. [Dessart et al. 2008; Olivares E. et al. 2010](#)). This technique consists on inferring the colour excess ($E_{B-V}^{\text{h,spec}}$) of an SN from the comparison between its spectra and those of reddening-corrected SNe or spectral models. We compile $E_{B-V}^{\text{h,spec}}$ values from the literature for 22 SNe in our set. We also compute $E_{B-V}^{\text{h,spec}}$ for 36 SNe in our sample, using the prescription given in Appendix G. The $E_{B-V}^{\text{h,spec}}$ are collected in Column 4 of Table L3. The typical $E_{B-V}^{\text{h,spec}}$ uncertainty is of 0.091 mag.

Fig 5 shows residuals about the one-to-one relation between $E_{B-V}^{\text{h,C3}}$ and $E_{B-V}^{\text{h},V-I}$ (r_{V-I}^{C3} , top panel), $E_{B-V}^{\text{h},V-I}$ and $E_{B-V}^{\text{h,spec}}$ ($r_{\text{spec}}^{\text{h},V-I}$, middle panel), and between $E_{B-V}^{\text{h,spec}}$ and $E_{B-V}^{\text{h,C3}}$ ($r_{\text{C3}}^{\text{spec}}$, bottom panel) for the 44 SNe in our set having $E_{B-V}^{\text{h,C3}}$, $E_{B-V}^{\text{h},V-I}$, and $E_{B-V}^{\text{h,spec}}$. For r_{V-I}^{C3} we obtain a mean, $\hat{\sigma}$, and typical error of 0.02, 0.09, and 0.10 mag, respectively. For $r_{\text{spec}}^{\text{h},V-I}$ we compute a mean, $\hat{\sigma}$, and typical error of 0.00, 0.14, and 0.12 mag, respectively. For $r_{\text{C3}}^{\text{spec}}$ we calculate a mean, $\hat{\sigma}$, and typical error of -0.02 , 0.13, and 0.12 mag, respectively. Since the $\hat{\sigma}$ values are quite similar to the typical residual errors, the observed dispersion is mainly due to colour excess errors. The mean offsets are statistically consistent with zero within $\pm 1.3\hat{\sigma}/\sqrt{N}$. Therefore, we do not detect systematic differences between the colour excesses inferred with the three aforementioned methods. Based on the latter, for the 77 SNe in our set having $E_{B-V}^{\text{h,C3}}$, $E_{B-V}^{\text{h},V-I}$, and/or $E_{B-V}^{\text{h,spec}}$ estimates, we adopt the weighted mean of those values as E_{B-V}^h . For SNe 1980K, 2006my, 2008gz, 2014cx, and 2017it we obtain negative E_{B-V}^h values (see Column 6 of Table L1). The values of the first four objects are consistent with zero within 1.3σ , while for SN 2017it the offset is of -2.1σ . Although negative E_{B-V}^h values have no physical meaning, we keep those values as we do not have evidence to discard them.

For SNe in our sample without E_{B-V}^h estimates, we evaluate to use colour excesses inferred from the pseudo-equivalent width of the host galaxy NaID absorption line (pEW_{NaID}). We compile pEW_{NaID} values from the literature⁷ for 89 SNe in our sample. With those values, we compute colour excesses ($E_{B-V}^{\text{h,NaID}}$) using the relation of [Poznanski et al. \(2012\)](#), and adopting a relative E_{B-V} error of 68 per cent ([Phillips et al. 2013](#)). The pEW_{NaID} becomes insensitive to estimate the colour excess

⁵ <http://edd.ifa.hawaii.edu/>

⁶ <https://github.com/olrodrig/C3M>

⁷ If pEW_{NaID} is not reported but E_{B-V}^h is, then we recover pEW_{NaID} using the corresponding E_{B-V} (pEW_{NaID}) calibration.

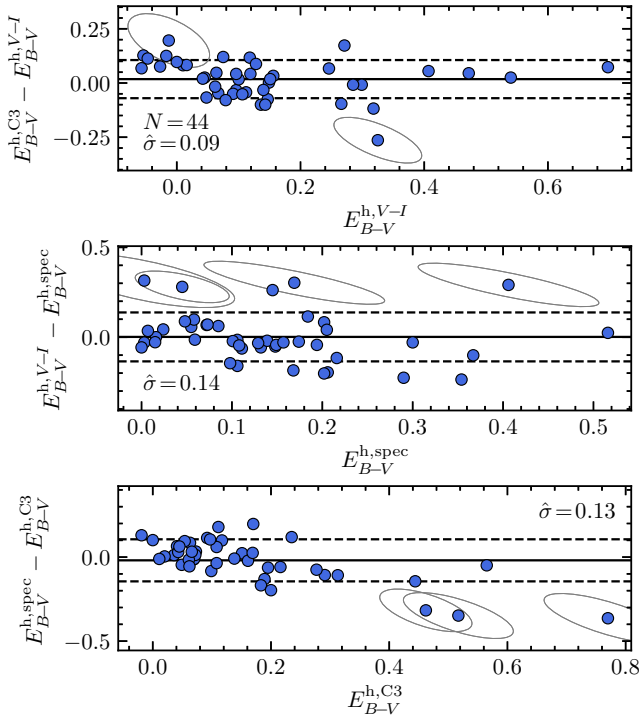


Figure 5. Residuals about the one-to-one relation between E_{B-V}^h values computed with the C3 method and the colour method (top panel), the colour method and the spectrum-fitting technique (middle panel), and the spectrum-fitting technique and the C3 method (bottom panel). Solid lines are mean values and dashed lines are $\pm 1 \hat{\sigma}$ limits. Ellipses are 1σ confidence regions, which for clarity are drawn only for SNe outside $\pm 2 \hat{\sigma}$ from the mean.

for $\text{pEW}_{\text{NaID}} > 0.1$ nm (e.g. Phillips et al. 2013), equivalent to $E_{B-V} > 0.21 \pm 0.14$ mag in the Poznanski et al. (2012) relation. Therefore, we assume the latter lower limit for all SNe with pEW_{NaID} greater than 0.1 nm. The $E_{B-V}^{\text{h,NaID}}$ values are listed in Column 4 of Table L3.

Fig 6(a) shows $E_{B-V}^{\text{h,NaID}}$ against E_{B-V}^h (54 SNe). Fitting a straight line with a slope of unity, we measure an offset and $\hat{\sigma}$ value of -0.09 and 0.11 mag, respectively. The offset is equivalent to $-6.0 \hat{\sigma} / \sqrt{N}$, which means that the $E_{B-V}^{\text{h,NaID}}$ values are systematically lower than E_{B-V}^h . Therefore, for the 24 SNe in our sample without E_{B-V}^h estimates but with $E_{B-V}^{\text{h,NaID}}$ values we adopt $E_{B-V}^h = E_{B-V}^{\text{h,NaID}} + 0.09$ mag, including in quadrature an error of 0.11 mag.

For the highly reddened SNe 2002hh and 2016ija (both without E_{B-V}^h and with $E_{B-V}^{\text{h,NaID}} > 0.21$ mag) we adopt the E_{B-V}^h values reported by Pozzo et al. (2006) and Tartaglia et al. (2018), respectively. In the case of SN 2002hh, the colour excess has two components: $E_{B-V} = 1.065$ mag (which includes E_{B-V}^{G}) with $R_V = 3.1$, and $E_{B-V} = 1.545 \pm 0.182$ mag with $R_V = 1.1$. For simplicity in the forthcoming analyses, we consider the first component as E_{B-V}^{G} and the second one as E_{B-V}^h .

Fig. 6(b) shows the histogram of E_{B-V}^h . To identify extreme values in the E_{B-V}^h distribution, we use the Chauvenet (1863) criterion. We find that SNe 2002hh, 2009hd, and 2016ija have E_{B-V}^h values greater than the Chauvenet upper rejection limit ($E_{B-V}^h = 1$ mag), so we consider them as outliers. The E_{B-V}^h distribution (removing the extreme values)

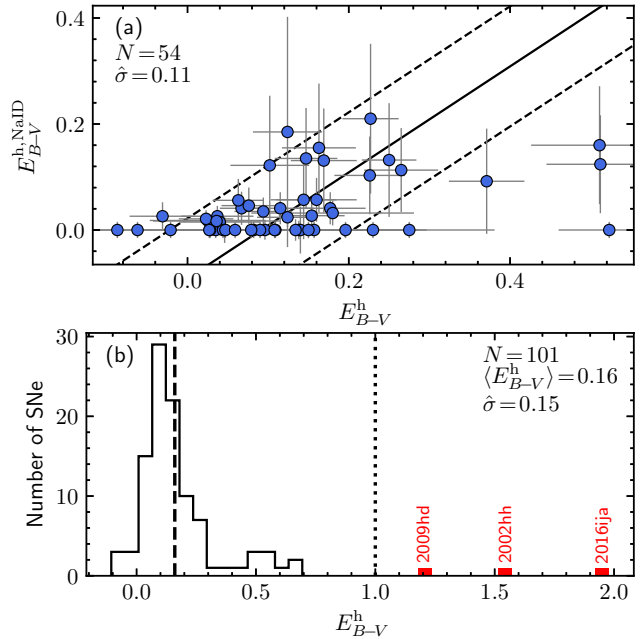


Figure 6. Panel (a): colour excesses computed from pEW_{NaID} versus the E_{B-V}^h values adopted in this work. The solid line is a straight line fit with a slope of unity, and dashed lines are the $\pm 1 \hat{\sigma}$ limits around the fit. Error bars are 1σ errors. Panel (b): histogram of E_{B-V}^h . The dotted line is the Chauvenet upper rejection limit ($E_{B-V}^h = 1$ mag). The dashed line indicates the mean E_{B-V}^h of the 101 SNe with $E_{B-V}^h < 1$ mag. Red bins are outliers.

has a mean and $\hat{\sigma}$ of 0.16 and 0.15 mag, respectively. For the six SNe in our set without E_{B-V}^h (SNe 2004eg, PTF11go, PTF11htj, PTF11izt, PTF12grj, and LSQ13dpa) we adopt the mean and $\hat{\sigma}$ of the latter distribution as E_{B-V}^h and its error, respectively.

The adopted E_{B-V}^h values are in Column 6 of Table L1. The typical E_{B-V}^h error is of 0.08 mag.

3.7 Explosion epochs

The SN explosion epoch is typically estimated as the midpoint between the last non-detection t_{ln} and the first SN detection t_{fd} . In order to improve the t_0 estimates for the SNe in our set, we use the SNII_ETOS code⁸ (Rodríguez et al. 2019). The latter computes t_0 given a set of optical spectra as input and a uniform prior on t_0 provided by t_{ln} and t_{fd} (for more details, see Rodríguez et al. 2019). If SNII_ETOS is not able to compute t_0 for an SN, then we adopt the midpoint between t_{ln} and t_{fd} if $t_{\text{fd}} - t_{\text{ln}} < 20$ d, otherwise we use the t_0 value reported in the literature.

Table L4 lists the t_{ln} (Column 2), t_{fd} (Column 3), and the adopted t_0 (Column 4) values (also reported in Column 7 of Table L1) for our SN set. The typical t_0 error is of 3.8 d.

⁸ https://github.com/olrodrig/SNII_ETOS

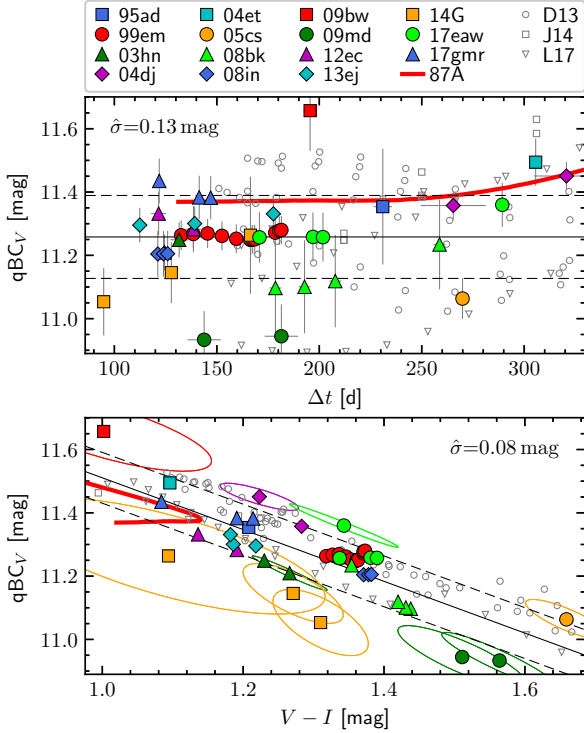


Figure 7. qBC_V values for the SNe in the BC calibration set (filled symbols), the D13, J14, and L17 models (empty symbols), and the long-rising SN 1987A (red thick line), as a function of time since explosion (top panel) and $V - I$ colour (bottom panel). Solid lines are the best polynomial fit to the observed data, while dashed lines indicate the $\pm 1\sigma$ limits around the fit. Error bars are 1σ errors and ellipses indicate 1σ confidence regions, which for clarity are drawn only for SNe outside the $\pm 1\sigma$ limits.

4 ANALYSIS

4.1 Quasi-bolometric and bolometric corrections

The top panel of Fig. 7 shows the qBC_V values for the 15 SNe in the BC calibration set against the time since explosion. For comparison we include the D13, J14, and L17 models, along with the long-rising SN 1987A, which is typically used to estimate BC_V for normal SNe II (e.g. Hamuy 2001; Bersten & Hamuy 2009; Maguire et al. 2010). In the figure we see that, except for SN 2014G, the four SNe with three or more points at $\Delta t < 250$ d and a time baseline greater than 30 d (SNe 1999em, 2008bk, 2013ej, and 2017eaw) seems to be consistent with a constant qBC_V value, as in the case of SN 1987A. For SNe 2017eaw and 2008bk we notice that the qBC_V values at $\Delta t > 250$ d are 0.1–0.15 mag greater than the values at $\Delta t < 210$ d. This could be due to the effect of newly formed dust. We also notice differences in qBC_V of around 0.3–0.7 mag between the sub-luminous SNe 2005cs, 2008bk, 2009md (e.g. Spiro et al. 2014) and the moderately-luminous SNe 2004et and 2009bw (e.g. Inserra et al. 2013).

The bottom panel of Fig. 7 shows qBC_V versus $V - I$. We detect a correlation between both quantities, in the sense that the redder the SN the lower the qBC_V . This correlation is also displayed by models (empty symbols), which are consistent with the linear fit to the observations (solid line) within $\pm 1\sigma$ (dashed lines). Since the errors in E_{B-V}^h , E_{B-V}^G , and V -band photometry affect the qBC_V and $V - I$ values,

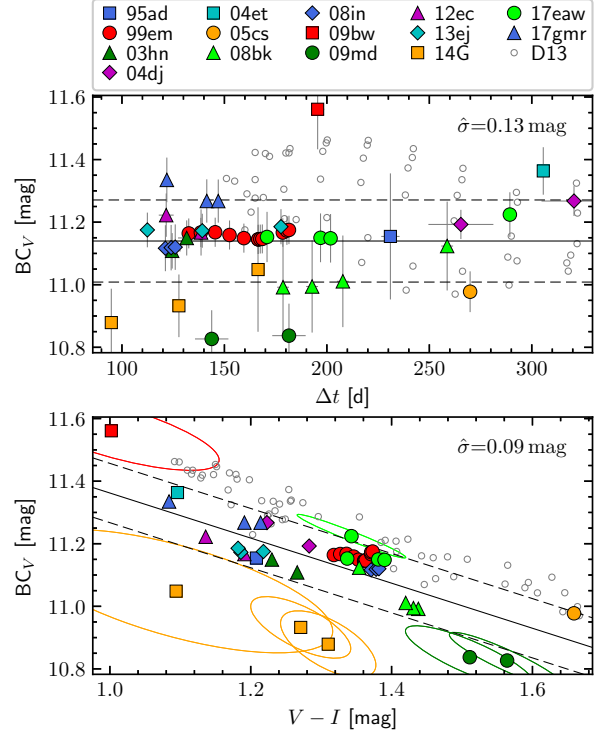


Figure 8. BC_V values as a function of time since explosion (top panel) and $V - I$ (bottom panel). Symbols, lines, error bars, and ellipses have the same meaning than in Fig. 7.

the confidence region of each observation is an elongated ellipse. We see that the confidence regions are nearly oriented in the direction of the qBC_V versus $V - I$ correlation. Therefore, the errors in E_{B-V}^G , E_{B-V}^h , and V -band photometry are not the main sources of the observed dispersion.

Fig. 8 shows BC_V against the time since explosion (top panel) and $V - I$ (bottom panel). As we can see in the figure, the behaviour of BC_V is the same as that of qBC_V .

4.2 BC calibration

4.2.1 BC_V versus $V - I$

To calibrate the dependence of BC_V on $V - I$ displayed in the bottom panel of Fig. 8, we use the expression

$$BC_x = ZP_x^{BC} + \Psi_x(X). \quad (24)$$

Here, ZP_x^{BC} is the zero-point for the x -band BC calibration, and Ψ_x is a polynomial function (without the zero-order term) representing the dependence of BC_x on the independent variable X (in our case, $X = V - I$). To compute the polynomial parameters, we minimize

$$s^2 = \sum_{SN} \sum_i \left[BC_{V,i}^{SN} + \delta^{SN} - \Psi_V \left((V - I)_i^{SN} \right) \right]^2, \quad (25)$$

where δ^{SN} is an additive term to normalize the BC_V values of each SN to the same scale, and the polynomial order is determined with the model selection described in Appendix C.

The top panel of Fig. 9 shows the result of the aforementioned process, where we exclude SNe 1995ad, 2004et, 2005cs, and 2009bw because they have only one BC_V esti-

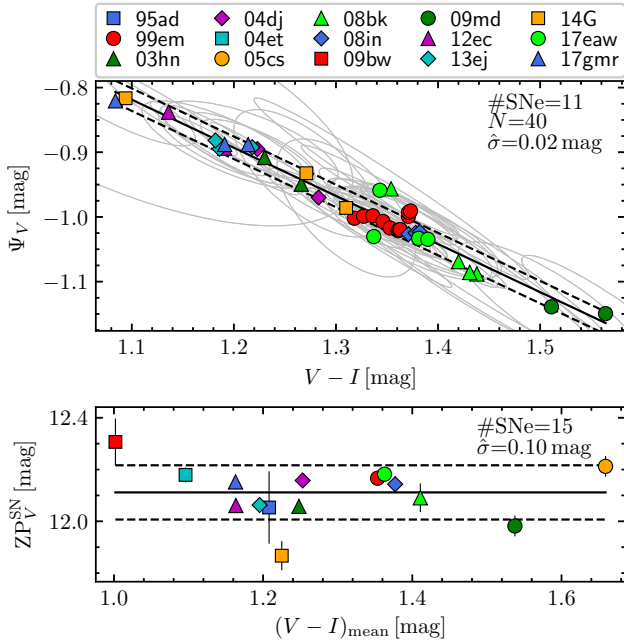


Figure 9. Top panel: Ψ_V against $V-I$, where the solid line is a linear fit and ellipses are the 1σ confidence regions. Bottom panel: ZP_V^{SN} as a function of the mean $V-I$ colour, where the solid line indicates the mean value. Dashed lines are the $\pm 1\hat{\sigma}$ limits.

mate. From this analysis we obtain that data are well represented by a straight line with slope (β_V) of -0.745 ± 0.002 .

To compute the ZP_V^{BC} value for each SN (ZP_V^{SN}), we arrange equations (24), (15), and (2), obtaining

$$ZP_V^{\text{SN}} = (m_{\text{bol},i} - (1 + \beta_V)V_i + \beta_V I_i) + (E_{B-V}^G + E_{B-V}^h)\xi, \quad (26)$$

where $\xi = (1 + \beta_V)R_{\lambda_V} - \beta_V R_{\lambda_I} = 2.01$ (using the R_{λ_x} values provided in Table A1). The angle brackets in equation (26) denote a weighted mean with weights

$$w_i = \left[\sigma_{m_{\text{bol},i}}^2 + (1 + \beta_V)^2 \sigma_{V_i}^2 + \beta_V^2 \sigma_{I_i}^2 \right]^{-1}, \quad (27)$$

where $\sigma_{m_{\text{bol},i}}$ only includes the error on photometry. The random error for each ZP_V^{SN} value is given by

$$\sigma_{ZP_V^{\text{SN}}} = \left[\frac{1}{\sum_i w_i} + (\sigma_{E_{B-V}^G}^2 + \sigma_{E_{B-V}^h}^2)\zeta^2 \right]^{1/2}, \quad (28)$$

where $\zeta = \xi - R_p$, being R_p the pSED total-to-selective extinction ratio (see Appendix B). For our BC calibration set $R_p = 1.68$, so the E_{B-V}^G and E_{B-V}^h errors are scaled by 0.33. For example, an E_{B-V}^h uncertainty of 0.08 mag (the typical value for our sample) induces an error on ZP_V^{SN} of 0.03 mag.

The bottom panel of Fig. 9 shows the ZP_V^{SN} values for the SNe in the BC calibration set. To verify whether a residual correlation between ZP_V^{SN} and $V-I$ exists, in the figure we plot the ZP_V^{SN} values against mean $V-I$ colours. Using the model selection given in Appendix C, we find that data are consistent with ZP_V^{SN} being constant, meaning that all the dependence of ZP_V^{SN} on $V-I$ was captured by Ψ_V . We compute a mean and $\hat{\sigma}$ value of 12.11 and 0.10 mag, respectively. The typical ZP_V^{SN} error is about 0.03 mag, so the observed $\hat{\sigma}$ value is mainly due to intrinsic differences between SNe. Therefore we adopt $ZP_V^{\text{BC}} = 12.11 \pm 0.10$ mag.

Table 2. BC calibrations.

x	X	β_x	ZP_x^{BC} (mag)
V	$V-I$	-0.745 ± 0.002	12.11 ± 0.10
r	$r-I$	-0.837 ± 0.004	12.35 ± 0.10
R	$R-I$	-0.755 ± 0.007	12.35 ± 0.10
i	$i-I$	-0.963 ± 0.005	12.42 ± 0.10
I	$\Delta t/(100 \text{ d})$	0.036 ± 0.002	12.37 ± 0.10
V	–	–	11.15 ± 0.18
r	–	–	11.89 ± 0.16
R	–	–	12.07 ± 0.14
i	–	–	11.91 ± 0.12
I	–	–	12.44 ± 0.11

Notes. $\text{BC}_x = ZP_x^{\text{BC}} + \beta_x X$, valid for Δt between 95 and 320 d. ZP_x^{BC} errors do not include the uncertainty due to the α error.

4.2.2 BCs for other combinations

In addition to BC_V as a function of $V-I$, we also calibrate the dependence of BC_x for the $VrRiI$ bands as a function of different independent variables. In the BC calibration set there are only six SNe having ri photometry in the radioactive tail (namely SNe 2008in, 2012ec, 2013ej, 2014G, 2017eaw, and 2017gmr). For the remaining nine SNe we convert the RI magnitudes to ri ones (see Appendix H).

To calibrate the dependence of BC_x on a given X variable, we perform the same analysis as in Section 4.2.1. As independent variables, we consider the ten colour indices that can be defined with the $VrRiI$ bands along with Δt . We find that the BC calibrations providing the lowest $\hat{\sigma}$ values are BC_V as a function of $V-I$, BC_r as a function of $r-I$, BC_R as a function of $R-I$, BC_i as a function of $i-I$, and BC_I as a function of Δt . In all cases the dependence of BC_x on the X variable is linear. The slopes of the linear relations (β_x) are reported in Column 3 of Table 2.

The left-hand side of Fig. 10 shows the ZP_x^{SN} values for the aforementioned calibrations. For each one we find that the ZP_x^{SN} estimates are consistent with a constant value (using the model selection given in Appendix C). As for BC_V as a function of $V-I$, for $rRiI$ bands we adopt the mean and $\hat{\sigma}$ value as ZP_x^{BC} and its error, respectively. Those values are listed in Column 4 of Table 2. Given the domain of the data (top panel of Fig. 7), our BC calibrations are valid for Δt between 95 and 320 d. Since the BC calibration set includes sub-luminous (SNe 2005cs, 2008bk, and 2009md) and moderately-luminous (e.g. SNe 2004et, 2009bw, and 2017gmr) SNe II, we assume that our BC_x calibrations are valid for all normal SNe II.

We also compute BC_x calibrations assuming they are constant. The ZP_x^{BC} values are given in Column 4 of Table 2, while the ZP_x^{SN} estimates are shown in the right-hand side of Fig. 10. Since BC_x is not actually constant but depends on a specific X variable, there is a dependence of ZP_x^{SN} on the mean X values. The latter, as we can see in right-hand side of Fig. 10, is more evident for VrR bands.

The BCs with the best precision are those including the I -band in the calibration ($\hat{\sigma} = 0.10$ – 0.11 mag), followed by BC_i as a constant ($\hat{\sigma} = 0.12$ mag). The latter means that, among the $VrRiI$ bands, the I - and i -band magnitudes are more correlated with the bolometric one. In order to compare luminosities through the BC technique (equation 17), the I -band photometry along with BC_I as a function of Δt must be preferred. If the I -band photometry is not avail-

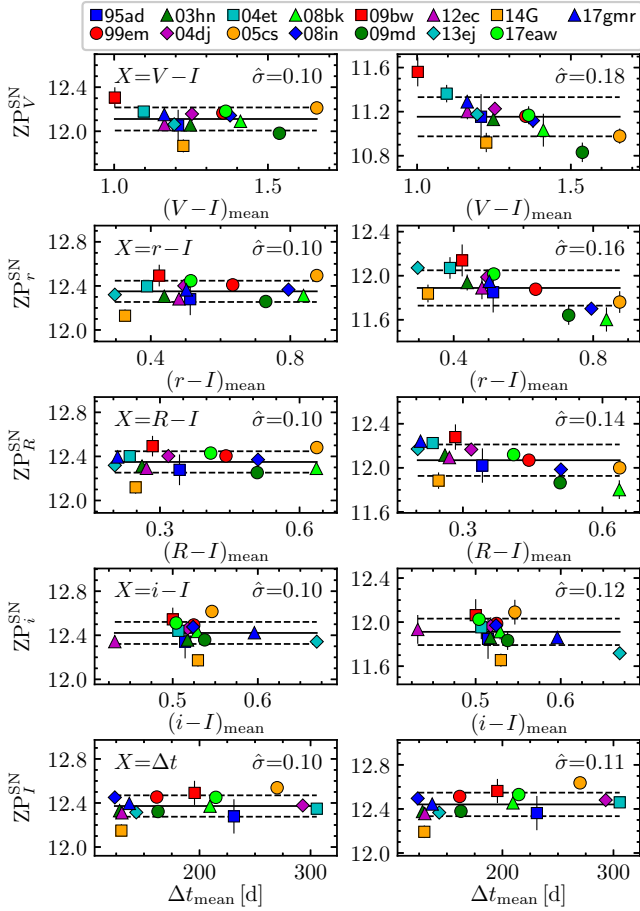


Figure 10. ZP_x^{SN} versus the mean X value. Left-hand panels: using the calibration with the lowest $\hat{\sigma}$ value. Right-hand panels: assuming a constant BC. Solid and dashed lines indicate mean values and $\pm 1 \hat{\sigma}$ limits around the mean, respectively.

able, then the i -, R -, r -, or V -band photometry along with the constant BC_x can be used to estimate luminosities. In the latter case, however, we caution that the derived luminosities of sub-luminous and moderately-luminous SNe II will be systematically under and overestimated, respectively, specially for the VrR bands.

4.3 ^{56}Ni mass distribution

4.3.1 $\log M_{56\text{Ni}}$ estimates

Armed with BCs for normal SNe II in the radioactive tail, we compute $\log M_{56\text{Ni}}$ using the recipe given in Appendix D.

For 25 SNe in our sample we find it is necessary to correct for the deposition function. As example, the left-hand side of Fig. 11 shows the $\log M_{56\text{Ni}}$ estimates of SN 2014G as a function of the time since explosion, assuming the complete γ -ray trapping scenario (i.e. $D_i = 0$ in equation 18). As visible in the figure, the $\log M_{56\text{Ni}}$ estimates are not concentrated around a constant but they decrease with time. This trend emerges because the ejecta becomes less able to thermalize γ -rays with time. In this case of γ -ray leakage, the inferred $\log M_{56\text{Ni}}$ corresponds to a lower limit. The right-hand side of the figure shows the $\log M_{56\text{Ni}}$ estimates corrected for f_{dep} . We can see that, using $T_0 = 127$ d, the

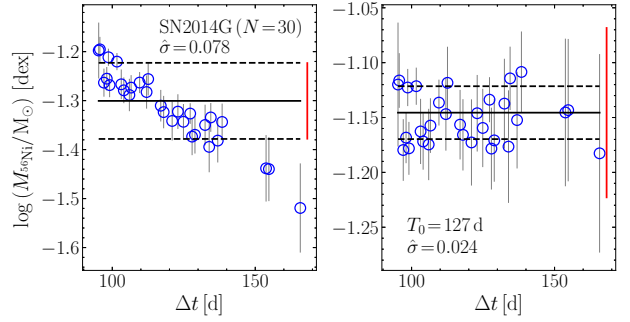


Figure 11. $\log M_{56\text{Ni}}$ estimates of SN 2014G versus the time since explosion, assuming the complete γ -ray trapping scenario (left-hand panel), and correcting for f_{dep} (right-hand panel). Solid horizontal lines correspond to the $\log M_{56\text{Ni}}$ values that maximize the likelihood, and dashed lines are the $\pm 1 \hat{\sigma}$ limits around them. Error bars are 1σ errors due to uncertainties on photometry, while red vertical bars depict the 1σ errors due to the uncertainty on μ , colour excesses, t_0 , and BC.

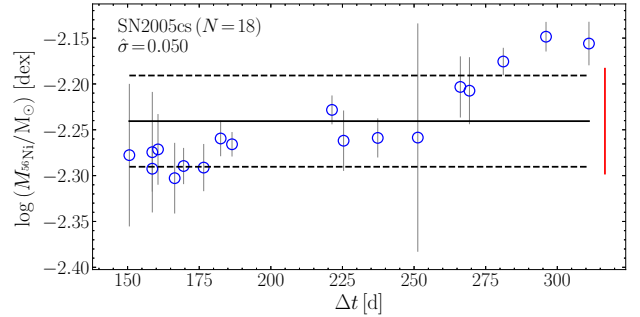


Figure 12. $\log M_{56\text{Ni}}$ estimates of SN 2005cs versus the time since explosion, assuming the complete γ -ray trapping scenario. Error bars and lines have the same meaning than in Fig. 11.

systematic with time disappears and the $\log M_{56\text{Ni}}$ estimates are consistent with a constant value.

In our SN set, SNe 2004dj, 2005cs, 2006my, 2013am, and 2013bu have $\log M_{56\text{Ni}}$ estimates that increase with time, which is shown in Fig. 12 for the case of SN 2005cs. This trend indicates that the observed luminosity increases with time relative to that expected from the radioactive decay. The latter suggests that (1) the SN ejecta during the early radioactive tail is not optically thin enough, so the energy deposited in the ejecta is not immediately emitted (i.e. $L < Q_{\text{dep}}$); and/or (2) there is an additional source of energy (i.e. $L > Q_{\text{dep}}$), whose relative contribution to the observed flux increases with time. For the latter scenarios, the higher and lower $\log M_{56\text{Ni}}$ estimates are closer to the real value, respectively. In this work, in order to be conservative about the origin of the observed tendency, for the aforementioned five SNe we adopt the $\log M_{56\text{Ni}}$ value obtained with $D_i = 0$.

In the case of SNe 1988A, 2003iq, 2005dx, PTF10gva, 2010aj, LS13dpa, 2015cz, and 2016ija we obtain $D_i = 0$ because the characteristics of their photometry (number of data, photometry errors, and time baseline) are not good enough to detect departures from a constant $\log M_{56\text{Ni}}$ value. In our sample 30 out of 102 SNe are consistent with $D_i \neq 0$. Therefore, we expect only two out of the aforementioned SNe to have $D_i \neq 0$, which should not impact our results.

Table 3. Error budget for the $\log M_{56\text{Ni}}$ estimates.

Error type	Error source	Typical error	Error in $\log M_{56\text{Ni}}$ (dex)	% of total error
Random	μ	0.18 mag	0.072	50.4
	E_{B-V}^h	0.08 mag	0.054	28.0
	t_0	3.8 d	0.013	1.6
	m_I	0.05 mag	0.012*	1.3
	E_{B-V}^G	0.01 mag	0.007	0.4
Systematic	All		0.092	81.7
	ZP_I^{BC}	0.10 mag	0.040	15.5
	α	3.9%	0.017	2.8
Total	All		0.102	100.0

*Considering three photometric points.

Table L5 lists the derived $\log M_{56\text{Ni}}$ and $M_{56\text{Ni}}$ values (Columns 6 and 7, respectively), along with the bands and numbers of photometric points used to compute $\log M_{56\text{Ni}}$ (Columns 2 and 4, respectively). The T_0 values of the 24 SNe corrected for the deposition function are listed in Column 5.

Table 3 shows the error budget for the $\log M_{56\text{Ni}}$ estimates computed with the I -band photometry (the preferred one), adopting the typical errors in our SN sample. The uncertainty on μ dominates the error budget, accounting for about 50 per cent of the total error. The ZP_I^{BC} error, on the other hand, is the main source of systematic uncertainty. Errors in photometry, t_0 , and E_{B-V}^G induce only ~ 3 per cent of the total $\log M_{56\text{Ni}}$ error. The typical error of the measured $\log M_{56\text{Ni}}$ is of 0.102 dex ($M_{56\text{Ni}}$ error of 24 per cent).

Similar to the I -band, the $\log M_{56\text{Ni}}$ error budgets for the $VrRi$ bands are dominated by uncertainties on μ and ZP_x^{BC} . Errors in photometry, t_0 , and E_{B-V}^G induce about 2–3 per cent of the total $\log M_{56\text{Ni}}$ error, while the typical $\log M_{56\text{Ni}}$ errors are of 0.143, 0.128, 0.121, and 0.109 dex for the $VrRi$ bands, respectively.

4.3.2 Outliers

Fig. 13 shows $\log M_{56\text{Ni}}$ versus the absolute V -band magnitude at 50 d since the explosion ($M_V^{50\text{d}}$, listed in Column 8 of Table L5). As reported by Hamuy (2003) and other authors (e.g. Spiro et al. 2014, Pejcha & Prieto 2015a,b, Valenti et al. 2016, Müller et al. 2017, Singh et al. 2019), we see a correlation between both quantities. As noted by Pejcha & Prieto (2015a), SN 2007od is an outlier in the $\log M_{56\text{Ni}}$ versus $M_V^{50\text{d}}$ distribution. The latter is a consequence of the increase in extinction due to the newly formed dust during the radioactive tail (Andrews et al. 2010; Inserra et al. 2011).

Using the model selection procedure (Appendix C), we find that the correlation between $\log M_{56\text{Ni}}$ and $M_V^{50\text{d}}$ can be represented by the straight line

$$\log M_{56\text{Ni}} = -7.708(\pm 0.445) - 0.3755(\pm 0.0271)M_V^{50\text{d}}, \quad (29)$$

where the parameter errors (in parentheses) are obtained performing 10^4 bootstrap resamplings.

To identify outliers other than SN 2007od in the $\log M_{56\text{Ni}}$ versus $M_V^{50\text{d}}$ distribution, we use the Chauvenet’s criterion. In Fig. 13 we see that SN 2010aj is located below the Chauvenet lower rejection limit but consistent with it within 2σ , which means that we cannot confirm that SN as

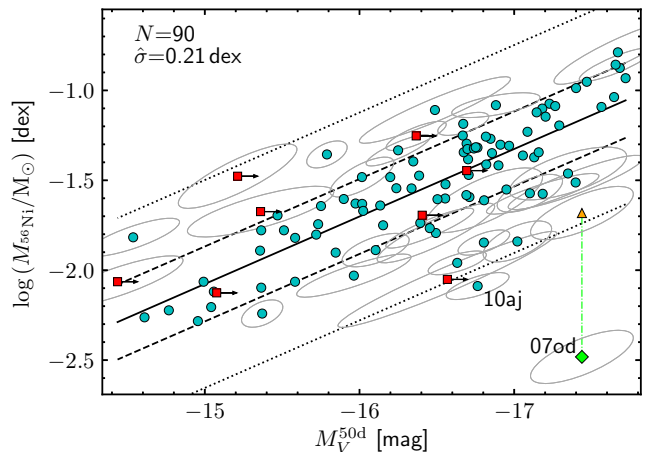


Figure 13. $\log M_{56\text{Ni}}$ against $M_V^{50\text{d}}$. The solid line is a straight-line fit to the data (cyan circles, 90 SNe), dashed lines indicate the $\pm 1\sigma$ limits around the fit, while dotted lines are the Chauvenet rejection limits. SNe with upper limits on $M_V^{50\text{d}}$ are indicated as red squares. The green diamond corresponds to SNe 2007od, while the orange triangle is SN 2010aj with a $\log M_{56\text{Ni}}$ correction of 0.8 dex. Ellipses indicate 1σ confidence regions, which for clarity are drawn only for SNe outside the $\pm 1\sigma$ limits.

an outlier. SN 2010aj was presented in Inserra et al. (2013), which suggested that it may be affected by newly formed dust. In that work, however, the lack of further evidence did not allow confirmation of the above scenario.

In the case of SNe 2007od we consider its $\log M_{56\text{Ni}}$ values as lower limits. Indeed, based on the $M_{56\text{Ni}}$ values reported by Inserra et al. (2011), the inclusion of the IR light excess to the luminosity of SN 2007od increases its $\log M_{56\text{Ni}}$ in ~ 0.8 dex. Applying this correction, SN 2007od moves in Fig. 13 from -6.3 to -2.5σ below the fit, becoming consistent with the $\log M_{56\text{Ni}}$ versus $M_V^{50\text{d}}$ distribution.

4.3.3 Sample completeness

The SNe in our set were selected from the literature by having at least three photometric points in the radioactive tail, so our sample is potentially affected by the selection bias. In order to correct for the latter bias and construct an SN sample as complete as possible, we use as reference the volume-limited SN sample of Shivvers et al. (2017). Most of the SNe II in that sample have completeness $\gtrsim 95$ per cent at the cut-off distance of 38 Mpc ($\mu = 32.9$ mag), while sub-luminous and highly reddened SNe have completeness $\gtrsim 70$ per cent (see Fig. 4 of Li et al. 2011). Therefore, we assume that the set of normal SNe II at $\mu < 32.9$ in the Shivvers et al. (2017) sample is roughly complete.

From the Shivvers et al. (2017) sample we select the 28 normal SNe II with $\mu < 32.9$ mag (hereafter the RC set), where we use μ values computed with the procedure described in Section 3.6.1 (reported in Column 8 of Table L2). We recalibrate their absolute R magnitudes (M_R) at maximum (M_R^{max} , listed in Li et al. 2011) using our μ values, and correcting for E_{B-V}^h (estimated with the procedure described in Section 3.6.2, and reported in Column 6 of Table L3). We also replace the Schlegel et al. (1998) E_{B-V}^G values used in Li et al. (2011) by the new ones provided by

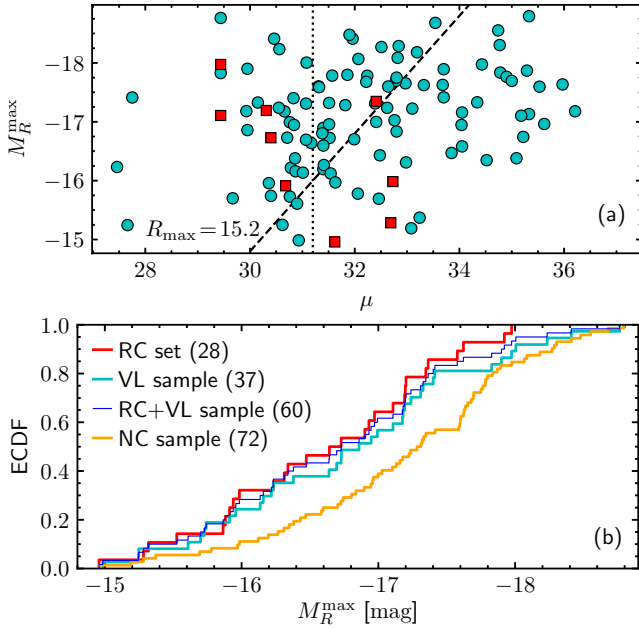


Figure 14. Panel (a): M_R^{\max} against μ for the SNe in our sample, where red squares are the SNe in common with the RC set. The dashed line corresponds to $R_{\max} = 15.2$ mag, while the dotted line ($\mu = 31.2$) is the limit for our VL sample. Panel (b): ECDF for the M_R^{\max} values in the RC (red line), VL (cyan line), and RC+VL (thin blue line) samples, and for the M_R^{\max} values of the SNe in our sample with $\mu > 31.2$ (orange line).

Schlafly & Finkbeiner (2011). Table L6 lists the M_R^{\max} estimates for the RC sample.

Among the 109 SNe in our sample, nine have M_R^{\max} estimates provided in the RC set, so we adopt those values for consistency. Out of the remaining 100 SNe:

1. Forty-seven SNe have R - or r -band light curves during the maximum light, where r magnitudes are converted into R ones using $r - R = 0.12$ (see Appendix H). We measure M_R^{\max} performing an ALR fit to the maximum photometry or adopting the brightest M_R value (M_R^{br}) as M_R^{\max} . The average of the rise time (t_R^{rise}) for the latter SNe is of 15 ± 6 d (1σ error), while the mean $V - R$ and $R - I$ colours at time t_R^{rise} are of 0.15 ± 0.08 and 0.04 ± 0.07 mag, respectively.

2. Thirty SNe have R/r light curves where the maximum light cannot be determined; six SNe have VI photometry, which we convert into R magnitudes using $V - R = 0.05 + 0.59(V - I)$ (see Appendix H); and eight SNe (one SN) only have V -band (I -band) photometry, which we convert into R magnitudes using $V - R = 0.15$ ($R - I = 0.04$). For each of these 45 SNe we fit a straight line to the light curve, compute M_R at t_R^{rise} ($M_R(t_R^{\text{rise}})$), and adopt the minimum between M_R^{br} and $M_R(t_R^{\text{rise}})$ as M_R^{\max} .

3. Eight SNe have photometry starting at $\Delta t > 80$ d. Two of them (SNe 1997D and 2004eg) are sub-luminous SNe II, which tend to have flat light curves during the photospheric phase (e.g. Spiro et al. 2014), so we adopt M_R^{br} as M_R^{\max} . For the remaining six SNe we estimate M_R^{\max} using their $\log M_{56\text{Ni}}$ values and $M_R^{\max} = -20.01 - 1.86 \log M_{56\text{Ni}}$, obtained from the 47 SNe with well-defined maximum light.

The M_R^{\max} values for the SNe in our sample are reported in Table L6 and plotted in Fig. 14(a) against μ . The mean

apparent R -band magnitude at maximum (R_{\max} , corrected for reddening) is of 15.2 mag, which is indicated as a dashed line. As we move to greater R_{\max} values (right-hand side of the dashed line) we see a decrement in the number of SNe, which is due to (1) bright SNe (in apparent magnitude) are more likely to be selected for photometric monitoring in the radioactive tail than faint ones; and (2) faint SNe have in general less photometric points in the radioactive tail than bright ones, so they are more likely not to meet our selection criterion of having at least three photometric points. In order to minimize the effect of the selection bias, we construct a volume-limited (VL) sample with the 37 SNe at $\mu \leq 31.2$ such that the selection bias could be relevant only in the small region between $R_{\max} > 15.2$ and $\mu \leq 31.2$.

Fig. 14(b) shows the empirical cumulative distribution function (ECDF) for the M_R^{\max} values in the VL (cyan line) and the RC (red line) samples. To test whether both M_R^{\max} samples are drawn from a common unspecified distribution (the null hypothesis), we use the two-sample Anderson-Darling (AD) test (e.g. Scholz & Stephens 1987). We obtain a standardized test statistic (T_{AD}) of -0.65 with a p -value of 0.74, meaning that the null hypothesis cannot be rejected at a significance level > 74 per cent. Since the M_R^{\max} values of the RC and the VL samples are likely drawn from the same M_R^{\max} distribution, we can assume that the completeness of both samples is quite similar, so we combine them into a single data set (RC+VL). The M_R^{\max} ECDF of the RC+VL sample (blue thin line) has a minimum, maximum, mean and σ of -18.8 , -15.0 , -16.7 , and 0.9 mag, respectively.

Fig. 14(b) also shows the ECDF for the M_R^{\max} values of the 72 SNe at $\mu > 31.2$ (orange line), which we refer as the non-complete (NC) sample. Using the two-sample AD test to test the null hypothesis for the M_R^{\max} values of the RC+VL and the NC samples, we obtain a T_{AD} of 5.66 and a p -value of 0.002. Thus, the null hypothesis can be rejected at a significance level of 0.2 per cent, which is expected since the NC sample is affected by the selection bias.

In order to roughly quantify the number and magnitudes of the SNe missing from the NC sample, and therefore from our full sample, we proceed as follows. First, we divide the M_R^{\max} distribution into four bins of width 1 mag (Column 1 of Table 4), and register the number of SNe within each bin for the NC and the RC+VL samples (Columns 2 and 3, respectively). Then, since bright SNe are less affected by the selection bias, we scale the number of SNe in the RC+VL sample by a factor of 15/8 (Column 4) in order to match the number of SNe with $M_R^{\max} < -17.8$ to that of the NC sample. In other words, the numbers in Column 4 are the SNe we would expect for a roughly complete sample with 15 SNe at $M_R^{\max} < -17.8$. The number of expected SNe minus the observed ones (i.e. the NC sample) is listed in Column 5. Thus, to correct our full SN sample for selection bias, we have to include 3, 23, and 15 SNe of magnitude $-17.8 \leq M_R^{\max} < -16.8$, $-16.8 \leq M_R^{\max} < -15.8$, and $M_R^{\max} \geq -15.8$, respectively. The latter SNe can be randomly selected from the VL or the RC+VL sample within the corresponding M_R^{\max} bins.

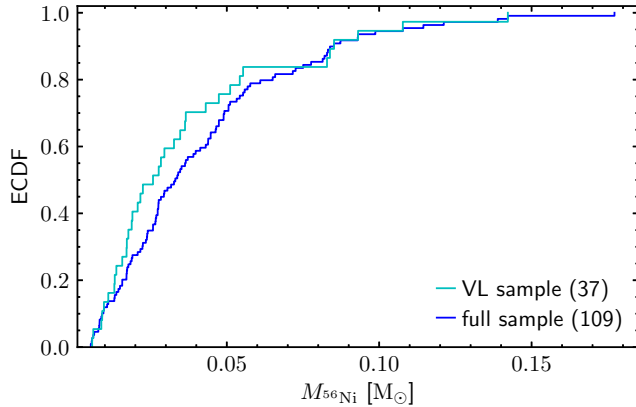
4.3.4 Mean ^{56}Ni mass

Fig. 15 shows the ECDFs for the $M_{56\text{Ni}}$ values in the VL (cyan line) and the full (blue line) samples. The ECDF

Table 4. Histogram for M_R^{\max} .

M_R^{\max} range	NC	RC+VL	Expected	Missing
-17.8, -18.8	15	8	15	0
-16.8, -17.8	36	21	39	3
-15.8, -16.8	15	20	38	23
-14.8, -15.8	6	11	21	15

Notes: Expected = 15/8(RC + VL). Missing = Expected - NC.

**Figure 15.** ECDF for the ^{56}Ni masses in the VL (cyan line) and the full sample (blue line).

of the VL sample has a $\langle M_{56\text{Ni}} \rangle$ and $\hat{\sigma}$ of 0.037 and $0.032 M_{\odot}$, respectively, while the random error (ran) on the mean ($\hat{\sigma}/\sqrt{N}$) is of $0.005 M_{\odot}$. On the other hand, the $M_{56\text{Ni}}$ distribution of the full sample has a minimum, maximum, mean, and $\hat{\sigma}$ of 0.005, 0.177, 0.042, and $0.033 M_{\odot}$, respectively, with $\hat{\sigma}/\sqrt{N} = 0.003 M_{\odot}$. The latter mean value corresponds to $\langle M_{56\text{Ni}} \rangle^{\text{unc}}$ uncorrected for selection bias ($\langle M_{56\text{Ni}} \rangle^{\text{unc}}$) which, as expected, is greater than the $\langle M_{56\text{Ni}} \rangle$ estimate for the VL sample. We note that for models based on the neutrino-heating mechanism (the generally accepted one for CC SNe, e.g. Burrows & Vartanyan 2021) the upper limit for the synthesized $M_{56\text{Ni}}$ is around 0.15 and $0.23 M_{\odot}$ (e.g. Ugliano et al. 2012; Suwa et al. 2019), which is consistent with the maximum $M_{56\text{Ni}}$ of our full SN sample.

The random error on $\langle M_{56\text{Ni}} \rangle^{\text{unc}}$ is made up of the sampling error along with the uncertainties induced by errors in μ and E_{B-V}^h . To estimate the random error in $\langle M_{56\text{Ni}} \rangle^{\text{unc}}$ induced by uncertainties in μ , we perform 10^5 simulations varying randomly μ according to its errors (assumed normal). For each realization, we rescale the log $M_{56\text{Ni}}$ values of the SNe in our full sample using the simulated μ values and calculate the mean ^{56}Ni mass. Using those 10^5 simulated mean values we compute a $\hat{\sigma}$ around $\langle M_{56\text{Ni}} \rangle^{\text{unc}}$ of $0.0009 M_{\odot}$, which we adopt as the error induced by uncertainties in μ . We repeat the same process for E_{B-V}^h , obtaining $0.0011 M_{\odot}$. The random error on $\langle M_{56\text{Ni}} \rangle^{\text{unc}}$ is $0.0028 M_{\odot}$ greater in quadrature than the error induced by μ and E_{B-V}^h . We adopt the latter value as the sampling error.

As mentioned in Section 4.3.3, to correct our full SN sample for selection bias we have to include 41 SNe. The mean ^{56}Ni mass of the selection-bias-corrected sample can be written as

$$\langle M_{56\text{Ni}} \rangle = \langle M_{56\text{Ni}} \rangle^{\text{unc}} - \text{sbc}. \quad (30)$$

Table 5. Error budget for the mean ^{56}Ni mass.

Error type	Error source	Typical error	Error in $\langle M_{56\text{Ni}} \rangle$ (M_{\odot})	% of total error
Random	Sampling	$0.0028 M_{\odot}$	0.0028	31.0
	sbc	$0.0014 M_{\odot}$	0.0014	7.7
	E_{B-V}^h	0.08 mag	0.0011	4.8
	μ	0.18 mag	0.0009	3.2
Systematic	All		0.00344	46.7
	ZP ^{BC}	0.10 mag	0.0034	45.6
	α	3.9 %	0.0014	7.7
All		0.00368	53.3	
Total			0.00504	100.0

Here,

$$\text{sbc} = \frac{41}{109 + 41} (\langle M_{56\text{Ni}} \rangle^{\text{unc}} - \langle M_{56\text{Ni}} \rangle_{41}^{\text{unc}}) \quad (31)$$

is the selection bias correction, where $\langle M_{56\text{Ni}} \rangle_{41}^{\text{unc}}$ is the mean ^{56}Ni mass computed with the 41 SNe that we have to add to our full SN sample. Performing 10^5 simulations, where the missing SNe (Column 5 of Table 4) are randomly selected from the VL sample within the corresponding M_R^{\max} bins, we obtain a sbc of $0.005 \pm 0.001 M_{\odot}$. Therefore, our best estimate of $\langle M_{56\text{Ni}} \rangle$ for normal SNe II is of 0.037 ± 0.003 (ran) M_{\odot} , with a systematic error due to the uncertainty on ZP^{BC} and α of $0.004 M_{\odot}$. This result compares to the $\langle M_{56\text{Ni}} \rangle$ value of 0.037 ± 0.005 (ran) M_{\odot} obtained with the VL sample.

Table 5 summarizes the error budget for $\langle M_{56\text{Ni}} \rangle$. The ZP^{BC} error, accounting for 46 per cent of the total uncertainty, dominates the error budget. The sampling error, which is the main source of random uncertainty, accounts for 31 per cent of the total error.

4.4 Mean iron yield

With our $\langle M_{56\text{Ni}} \rangle$ measurement along with equation (21) and $\eta = 1.07 \pm 0.04$ (see Section 3.5), we obtain a \bar{y}_{Fe} value of $0.040 \pm 0.005 M_{\odot}$ for normal SNe II.

In addition, we evaluate \bar{y}_{Fe} for CC SNe employing recent estimations of mean ^{56}Ni masses for other CC SN subtypes. The mean ^{56}Ni mass for CC SNe, using the SN rates provided in Shivvers et al. (2017), is given by

$$f_{\text{CC}}^{\text{Ni}} = 0.696 f_{\text{II}}^{\text{Ni}} + 0.304 f_{\text{SE}}^{\text{Ni}}. \quad (32)$$

Here,

$$f_{\text{II}}^{\text{Ni}} = 0.891 f_{\text{II-normal}}^{\text{Ni}} + 0.067 f_{\text{II-n}}^{\text{Ni}} + 0.042 f_{\text{long-rising}}^{\text{Ni}} \quad (33)$$

and

$$f_{\text{SE}}^{\text{Ni}} = 0.360 f_{\text{Ib}}^{\text{Ni}} + 0.356 f_{\text{Ic}}^{\text{Ni}} + 0.247 f_{\text{Ic}}^{\text{Ni}} + 0.037 f_{\text{Ic-BL}}^{\text{Ni}}, \quad (34)$$

where f^{Ni} denotes the mean ^{56}Ni mass for the subscripted CC SN types and subtypes.

In equation (33) we adopt $f_{\text{long-rising}}^{\text{Ni}} = 0.086 M_{\odot}$ (Anderson 2019) and for SNe II_n we assume $f_{\text{II-n}}^{\text{Ni}} = f_{\text{II-normal}}^{\text{Ni}}$, thus obtaining $f_{\text{II}}^{\text{Ni}} = 0.039 M_{\odot}$.

For SNe II_b, II_c, II_c, and II_c-BL we adopt the mean $M_{56\text{Ni}}$ values from the compilation of Anderson (2019): 0.124, 0.199, 0.198, and $0.507 M_{\odot}$, respectively. The ^{56}Ni masses of the SE SNe compiled by Anderson (2019) were

mainly computed with the Arnett (1982) rule, which overestimates the ^{56}Ni mass of SE SNe by ~ 50 per cent (Dessart et al. 2015, 2016). Including this correction to the mean $M_{56\text{Ni}}$ values of SE SNe, with equation (34) we get $f_{\text{SE}}^{\text{Ni}} = 0.122 M_{\odot}$. Recently, by using the radioactive tail luminosity, Afsariardchi et al. (2020) estimated mean $M_{56\text{Ni}}$ values of 0.06, 0.11, 0.20, and $0.15 M_{\odot}$ for SNe I Ib, Ic, and Ic-BL, respectively⁹. Inserting these values in equation (33) we get $f_{\text{SE}}^{\text{Ni}} = 0.116 M_{\odot}$, which is similar to the previous finding. Since the SN samples of Anderson (2019) and Afsariardchi et al. (2020) are not corrected for selection bias, we adopt $f_{\text{SE}}^{\text{Ni}} < 0.12 M_{\odot}$.

Replacing the $f_{\text{SE}}^{\text{Ni}}$ and $f_{\text{II}}^{\text{Ni}}$ values in equation (32), we get $f_{\text{CC}}^{\text{Ni}} < 0.064 M_{\odot}$, where the contribution of normal SNe II to $f_{\text{CC}}^{\text{Ni}}$ is > 36 per cent. Finally, if we assume $\eta = 1.07$ for all CC SN subtypes, then from equation (21) we obtain $\bar{y}_{\text{Fe}} < 0.068 M_{\odot}$ for CC SNe.

4.5 Steepness as ^{56}Ni mass indicator

From the analysis of nine normal SNe II and the long-rising SN 1987A, Elmhamdi et al. (2003b) reported a linear correlation between $\log M_{56\text{Ni}}$ and the maximum value of dV/dt during the transition phase, called V -band steepness S_V . This correlation was also rebuilt by Singh et al. (2018), which included another 30 SNe to the sample of Elmhamdi et al. (2003b). The observed correlation is proposed to be a consequence of the ^{56}Ni heating during the transition phase (e.g. Pumo & Zampieri 2011, 2013). The latter produces slower transitions of the luminosity from the end of the plateau phase to the beginning of the radioactive tail as $M_{56\text{Ni}}$ increases. Since the correlation between $\log M_{56\text{Ni}}$ and steepness has not been studied for bands other than V , in this work we will include the $gVrRiI$ bands in the analysis.

In order to measure the x -band steepness, S_x , we represent the light-curve transition phase by the function

$$m_x(t) = m_{0,x} - \frac{a_{0,x}}{1 + e^{(t-t_{\text{PT},x})/w_{0,x}}} + p_{0,x} \frac{t - t_{\text{PT},x}}{100 \text{ d}} \quad (35)$$

(e.g. Olivares E. et al. 2010; Valenti et al. 2016). The parameters $m_{0,x}$, $a_{0,x}$, $t_{\text{PT},x}$ (the middle of the transition phase), $w_{0,x}$, and $p_{0,x}$ are obtained maximizing the model log-likelihood (equation C1). Fig. 16 shows this analytical fit applied to the V -band photometry of SN 2014G. Using the aforementioned parametric function, the x -band steepness (in mag d^{-1}) in the SN rest frame is given by

$$S_x = \left(\frac{a_{0,x}}{4w_{0,x}} + \frac{p_{0,x}}{100 \text{ d}} \right) / (1 + z_{\text{helio}}^{\text{SN}}). \quad (36)$$

Columns 2–7 of Table L7 list the $gVrRiI$ -band S_x values and their bootstrap errors. As visible in the table, the S_x estimates are in general not available for each of the $gVrRiI$ bands. In those cases we estimate S_x indirectly from the steepnesses in bands other than x (see Appendix J). These indirect S_x values (S_x^*) for the $gVrRiI$ bands and their errors are in Columns 8–13 of Table L7. Table 6 lists the mean and $\hat{\sigma}$ values of the $S_x^* - S_x$ estimates for the $gVrRiI$ bands.

⁹ Mean values were computed with ≤ 8 SNe per subtype, so we caution that those values are not statistically significant.

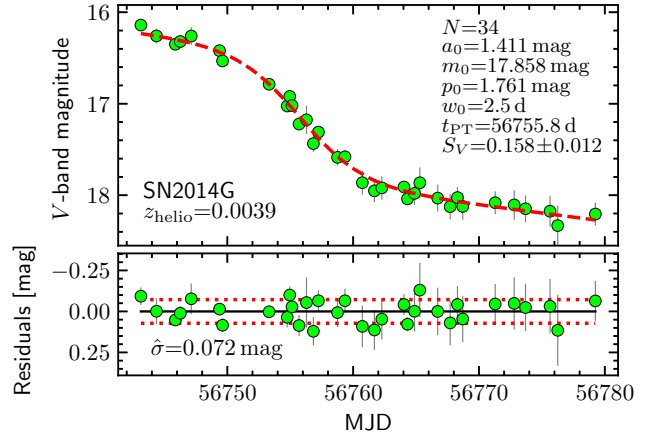


Figure 16. Top panel: V -band light curve of SN 2014G in the transition phase, where the dashed line corresponds to the best fit. Bottom panel: best fit residuals, where dotted lines indicate the $\pm 1 \hat{\sigma}$ limits. Error bars are 1σ errors.

Table 6. Mean $S_x^* - S_x$ values.

x	$\langle S_x^* - S_x \rangle$	$\hat{\sigma}$	N	x	$\langle S_x^* - S_x \rangle$	$\hat{\sigma}$	N
g	-0.002	0.016	16	V	-0.003	0.024	41
r	0.003	0.029	20	R	-0.002	0.017	32
i	-0.004	0.036	22	I	0.002	0.018	31

Note. Mean and $\hat{\sigma}$ values are in mag d^{-1} units.

Table 7. $\log M_{56\text{Ni}}$ versus S_x calibrations.

x	$c_{0,x}$ (dex)	$c_{1,x}$ (dex)	$\hat{\sigma}$ (dex)	N	r_x
g	-1.219 ± 0.049	-1.844 ± 0.256	0.217	72	-0.67
V	-1.201 ± 0.043	-1.789 ± 0.183	0.210	72	-0.69
r	-1.238 ± 0.047	-2.130 ± 0.292	0.219	72	-0.66
R	-1.217 ± 0.042	-2.053 ± 0.217	0.210	72	-0.69
i	-1.237 ± 0.044	-1.901 ± 0.231	0.221	72	-0.65
I	-1.223 ± 0.045	-2.106 ± 0.253	0.219	72	-0.66

Notes. $\log M_{56\text{Ni}} = c_{0,x} + c_{1,x} S_x$. $M_{56\text{Ni}}$ and S_x are in M_{\odot} and mag d^{-1} units, respectively.

The mean values are statistically consistent with zero within $1 \hat{\sigma} / \sqrt{N}$. Therefore, for SNe without an specific S_x value, we can use their respective S_x^* as a proxy.

Fig. 17 shows $\log M_{56\text{Ni}}$ versus S_x for the $gVrRiI$ bands. Through the model selection procedure (Appendix C), we find that the correlation between $\log M_{56\text{Ni}}$ and S_x is well represented by the straight line

$$\log M_{56\text{Ni}} = c_{0,x} + c_{1,x} S_x \quad (37)$$

which, for the V -band, corresponds to the best fit proposed by Elmhamdi et al. (2003b). The parameters $c_{0,x}$ and $c_{1,x}$ (and their bootstrap errors) for the $gVrRiI$ bands are reported in Table 7. To evaluate the linear correlation between $\log M_{56\text{Ni}}$ and S_x , we calculate the Pearson correlation coefficient r_x , listed in Column 6 of Table 7. The probability of obtaining $|r_x| \geq 0.65$ from a random population with $N = 72$ is < 0.001 per cent.

The observed $\hat{\sigma}$ of 0.21–0.22 dex for the $gVrRiI$ bands indicates that there is no preferred band for the $\log M_{56\text{Ni}}$ versus S_x correlation. Since the $\hat{\sigma}$ values are ~ 0.17 dex greater in quadrature than the typical random error

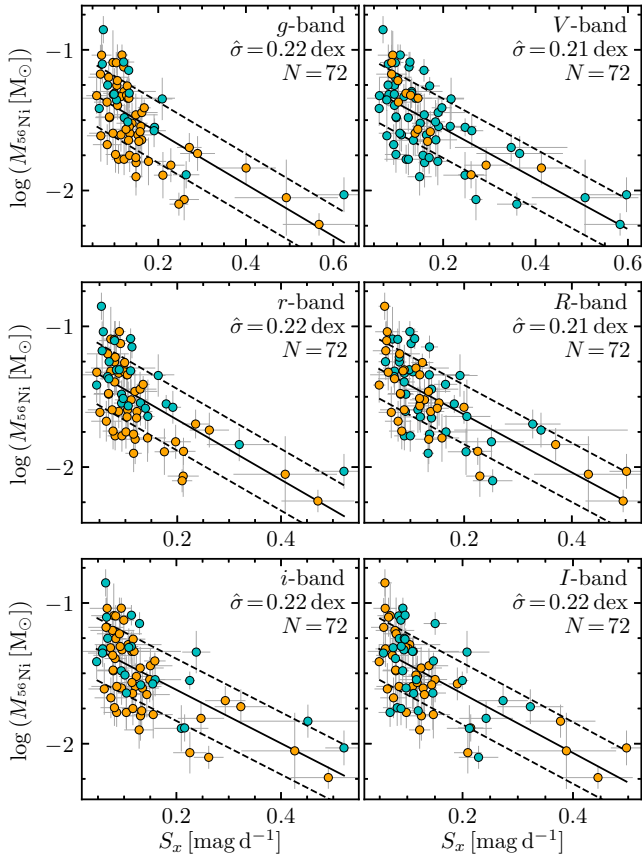


Figure 17. $\log M_{56\text{Ni}}$ against S_x for $gVrRiI$ bands. Cyan circles are SNe with S_x measured from their x -band light curves, while orange circles are SNe with S_x estimated from the steepnesses in other bands. Solid lines are straight-line fits to the data, dashed lines are $\pm 1 \hat{\sigma}$ limits around the fits, and error bars are 1σ errors.

(0.13 dex), the observed dispersion is mainly intrinsic. The latter was also pointed out by Pumo & Zampieri (2013). Indeed, the shape of light curves in the transition phase not only depends on $M_{56\text{Ni}}$ but also, among others, on the H mass retained before the explosion and the ^{56}Ni mixing (e.g. Young 2004; Bersten et al. 2011; Kozyreva et al. 2019).

Fig. 18 shows the residuals of the $\log M_{56\text{Ni}}$ versus S_V correlation (i.e. upper-right panel of Fig. 17) plotted against $M_V^{50\text{d}}$, where we detect a linear dependence of the residuals on $M_V^{50\text{d}}$. Therefore the Elmhamdi et al. (2003b) relation over and underestimates the $\log M_{56\text{Ni}}$ of sub-luminous and moderately-luminous SNe II, respectively, by up to ~ 0.3 dex. This fact, along with the low statistical precision of the Elmhamdi et al. (2003b) relation to measure $M_{56\text{Ni}}$ (around 50 per cent), makes the latter method poorly suited for ^{56}Ni mass measurements.

4.6 Nickel-magnitude-steepness relation

Our previous finding suggests a correlation of $\log M_{56\text{Ni}}$ as a function not only of S_x but also of the x -band absolute magnitude at $\Delta t = 50$ d ($M_x^{50\text{d}}$). The $M_x^{50\text{d}}$ values for $grRiI$ are listed in Table L9. If $M_x^{50\text{d}}$ is not available for a given band, then we estimate it using photometry in other bands and magnitude transformation formulae (see Appendix H).

Using the model selection procedure (Appendix C), we

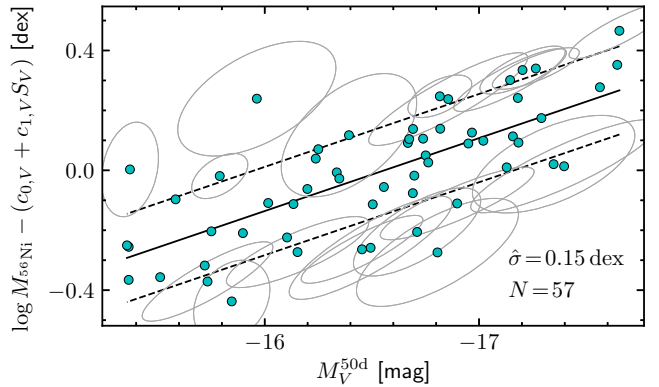


Figure 18. Residuals of the $\log M_{56\text{Ni}}$ versus S_V correlation, as a function of $M_V^{50\text{d}}$. The solid and dashed lines have the same meaning than in Fig 17. Ellipses are 1σ confidence regions, which for clarity are drawn only for SNe outside the dashed lines.

find that the correlation of $\log M_{56\text{Ni}}$ as a function of S_x and $M_x^{50\text{d}}$ can be represented by

$$\log M_{56\text{Ni}} = a_x + b_x M_x^{50\text{d}} + c_x \log S_x, \quad (38)$$

where $\log S_x$ is given by equation (E3). Fig. 19 shows the nickel-magnitude-steepness (NMS) relation for the $gVrRiI$ bands, while Table 8 lists the parameters (and their bootstrap errors) of equation (38) along with the ranges of $M_x^{50\text{d}}$ and $\log S_x$ where the relation is valid. To evaluate the linear correlation of $\log M_{56\text{Ni}}$ on $M_x^{50\text{d}}$ and $\log S_x$, we calculate the multiple correlation coefficient (R_x^{mc} , reported in Column 10 of Table 8). The probability of obtaining $R_x^{\text{mc}} \geq 0.89$ from a random population is < 0.001 per cent.

The NMS relation allows to measure $\log M_{56\text{Ni}}$ with a statistical precision of 0.12–0.14 dex ($M_{56\text{Ni}}$ error of ~ 30 per cent). The observed random error is about 0.08 dex, so the intrinsic random error on the NMS relation ($\sigma_{0,x}$, listed in Column 6 of Table 8) is around 0.10 dex. Since ~ 80 per cent of the SNe used to calibrate equation (38) have $\log M_{56\text{Ni}}$ computed with I - or i -band photometry, we adopt a systematic uncertainty due to the ZP^{BC} errors of 0.044 dex (the average between the errors on ZP_I^{BC} and ZP_i^{BC} in dex scale). The total systematic error (σ_{sys}), including the uncertainty due to α , is of 0.047 dex, while the total error on $\log M_{56\text{Ni}}$ provided by the NMS relation is given by

$$\sigma_{\log M_{56\text{Ni}}} = \sqrt{(b_x \sigma_{M_x^{50\text{d}}})^2 + (c_x \sigma_{\log S_x})^2 + \sigma_{0,x}^2 + \sigma_{\text{sys}}^2}. \quad (39)$$

Since $|b_x| < 0.4$, the $\log M_{56\text{Ni}}$ values estimated with the NMS relation are less dependent on E_{B-V}^h and μ than those computed with the radioactive tail photometry and the BC technique (Appendix D).

As a first application of the NMS relation, we compute $\log M_{56\text{Ni}}$ estimates ($\log M_{56\text{Ni}}^{\text{NMS}}$) for a sample of normal SNe II observed by the Zwicky Transient Facility (ZTF; Bellm et al. 2019; Graham et al. 2019). Specifically, we employ SNe from the ZTF bright transient survey¹⁰ (BTS; Fremling et al. 2020; Perley et al. 2020), which consists on SNe brighter than 19 mag. From this magnitude-limited survey, we select SNe spectroscopically classified as SNe II, discarding those (1) classified as Type IIb or IIc, (2) with long-

¹⁰ <https://sites.astro.caltech.edu/ztf/bts/explorer.php>

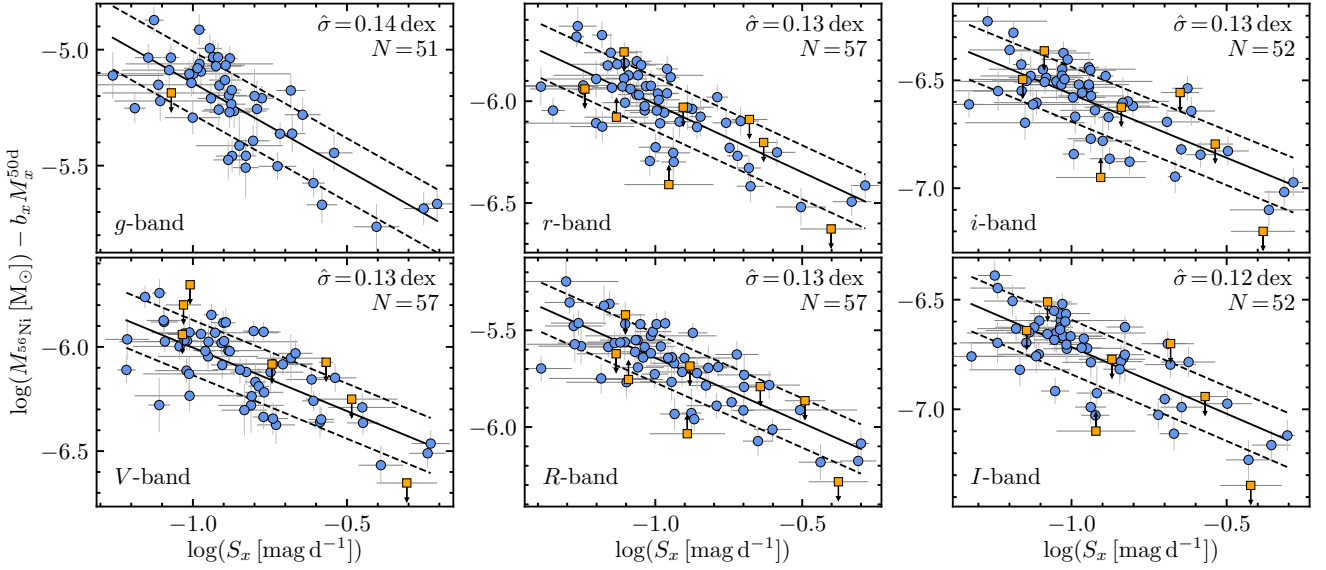


Figure 19. NMS relations for the *gVrRiI* bands. Solid lines are the best fits to the data (circles), while dashed lines indicate the $\pm 1\sigma$ limits around the fits. Orange squares correspond to SNe with lower/upper limits on M_x^{50d} . Error bars are 1σ errors.

Table 8. NMS relation parameters.

x	a_x (dex)	b_x (dex mag $^{-1}$)	c_x	$\hat{\sigma}$ (dex)	$\sigma_{0,x}$ (dex)	N	M_x^{50d} range (mag)	$\log S_x$ range (dex)	R_x^{mc}
<i>g</i>	-5.894 ± 0.461	-0.2311 ± 0.0306	-0.750 ± 0.097	0.136	0.112	51	-14.9, -17.4	-1.26, -0.21	0.89
<i>V</i>	-6.612 ± 0.409	-0.2778 ± 0.0266	-0.608 ± 0.083	0.132	0.106	57	-15.4, -17.7	-1.22, -0.23	0.89
<i>r</i>	-6.683 ± 0.459	-0.2710 ± 0.0294	-0.669 ± 0.087	0.132	0.107	57	-15.6, -18.1	-1.39, -0.29	0.90
<i>R</i>	-6.315 ± 0.449	-0.2487 ± 0.0287	-0.673 ± 0.082	0.128	0.094	57	-15.7, -18.2	-1.39, -0.30	0.90
<i>i</i>	-7.154 ± 0.442	-0.3066 ± 0.0281	-0.590 ± 0.079	0.127	0.098	52	-15.4, -17.7	-1.33, -0.28	0.90
<i>I</i>	-7.324 ± 0.430	-0.3083 ± 0.0267	-0.608 ± 0.080	0.124	0.098	52	-15.7, -18.1	-1.32, -0.30	0.91

Notes. $\log M_{56\text{Ni}} = a_x + b_x M_x^{50d} + c_x \log S_x$. $M_{56\text{Ni}}$, M_x^{50d} , and S_x are in units of M_\odot , mag, and mag d^{-1} , respectively.

rising light curves, (3) with less than three r_{ZTF} photometric points in the radioactive tail, (4) with t_0 errors greater than 10 d, and (5) with absolute magnitudes and steepnesses outside the range where the NMS relation is valid. The selected ZTF BTS (SZB) sample of 28 normal SNe II and their main properties are summarized in Table L10, while Fig. 20 shows their r_{ZTF} light curves¹¹. Out of the SNe in the SZB set, 24 have $M_R^{\text{max}} < -17$ mag, so the sample consists mainly of moderately-luminous SNe II.

Given that $r_{\text{ZTF}} - R = 0.14$ mag from the photospheric to the radioactive tail phase (see Appendix H), for the r_{ZTF} band we adopt the *R*-band NMS relation, but with $a_{r_{\text{ZTF}}} = a_R - 0.14b_R$ equal to -6.281 dex. Since we cannot measure E_{B-V}^h for the SZB sample with the available data, we assume $E_{B-V}^h = 0.16 \pm 0.15$ mag (the average of the E_{B-V}^h distribution shown in Fig. 6). Column 9 of Table L10 lists the inferred $\log M_{56\text{Ni}}^{\text{NMS}}$ values. For comparison, we also compute $\log M_{56\text{Ni}}$ with the radioactive tail luminosity ($\log M_{56\text{Ni}}^{\text{tail}}$, Column 10 of Table L10), using a constant $\text{BC}_{r_{\text{ZTF}}} = \text{BC}_R - 0.14$ equivalent to 11.93 ± 0.14 mag.

The mean offset between the $\log M_{56\text{Ni}}^{\text{tail}}$ and $\log M_{56\text{Ni}}^{\text{NMS}}$ values is of 0.038 dex with a $\hat{\sigma}$ of 0.110 dex. The $\hat{\sigma}$ value is similar to that expected for the NMS relation (0.13 dex),

while the offset is consistent with zero within $1.9\hat{\sigma}/\sqrt{N}$. As stated in Section 4.2.2, the use of the constant BC_R reported in Table 2 ($\text{BC}_R = 12.07$) overestimates the radioactive tail luminosities (and therefore the $\log M_{56\text{Ni}}^{\text{tail}}$ values) of moderately-luminous SNe II. To roughly estimate a more appropriate constant BC_R for the SZB sample, we use the ZP_R^{SN} values of the nine SNe in the BC calibration set with $M_R^{\text{max}} < -17$ mag, obtaining a BC_R of 12.13 mag. Increasing $\text{BC}_{r_{\text{ZTF}}}$ by 0.06 mag decreases the offset from 0.046 to 0.014 dex, being consistent with zero within $0.7\hat{\sigma}/\sqrt{N}$. In addition, the offset decreases from $1.9\hat{\sigma}/\sqrt{N}$ to zero if we adopt $E_{B-V}^h = 0.05$ mag. Therefore, part of the offset could be due to an overestimation of the adopted E_{B-V}^h . The results we obtain with the SZB sample provides further evidence supporting the usefulness of the NMS relation for $\log M_{56\text{Ni}}$ measurements.

5 DISCUSSION

5.1 Comparison with other works

Table 2 summarizes the BC values for SNe II in the radioactive tail reported by Hamuy (2001), Bersten & Hamuy (2009), Maguire et al. (2010), and Pejcha & Prieto (2015a). From each value we subtract the zero-point used to define the apparent bolometric magnitude scale

¹¹ Photometry obtained from the ALERCE (Förster et al. 2021) website (<https://alerce.online/>).

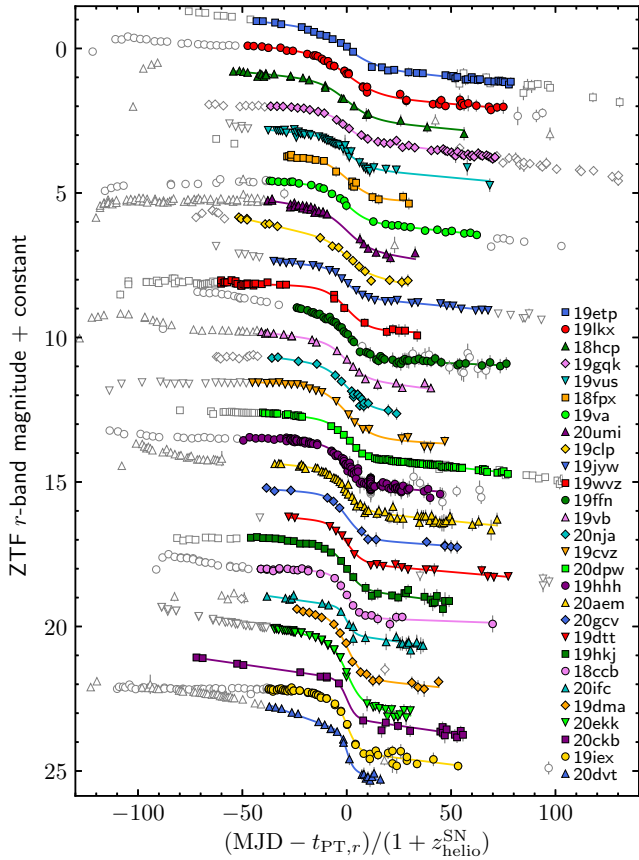


Figure 20. r_{ZTF} light curves of the 28 normal SNe II in the SZB sample. Data used to measure the steepness are shown with colour-filled symbols, while solid lines are analytical fits.

(-10.89 mag for Hamuy 2001 and Maguire et al. 2010, -11.64 mag for Bersten & Hamuy 2009, and -11.48 mag for Pejcha & Prieto 2015a). Since previous works reported constant BC values, for the comparison we use our estimates assuming a constant BC, which are also listed in the table. The BC values reported in the literature are consistent with our estimations within $\pm 1.1\sigma$. Except for Pejcha & Prieto (2015a), which did not report BC errors, the uncertainties provided in previous works are lower than those reported here. The latter is due to the few SNe used in previous studies to compute BCs. Indeed, they used only SN 1999em and the long-rising SN 1987A to compute BCs. It is interesting to note the good agreement between our constant BC values for $rRiI$ bands and those of Pejcha & Prieto (2015a) within ± 0.04 mag.

Table 10 collects the mean and $\hat{\sigma}$ values of the normal SN II $M_{56\text{Ni}}$ distributions presented in Blanc & Greggio (2008) and Müller et al. (2017). Despite the Blanc & Greggio (2008) sample includes the long-rising SN 1987A, we find that removing that SN only marginally modifies the reported mean and $\hat{\sigma}$ value. In addition, we include the mean ^{56}Ni mass computed with the 107 normal SNe II in the sample of Anderson (2019)¹². Since pre-

¹² $M_{56\text{Ni}}$ values are reported in Meza & Anderson (2020), from which we remove SN 2007od, the long-rising SNe 1987A, 1998A, 2000cb, 2006V, 2006au, and 2009E, and the LLEV SN 2008bm.

Table 9. Constant BC values for the radioactive tail.

BC _x (mag)	x	N	Reference
11.15 ± 0.06	V	2 ^a	Hamuy (2001)
10.94 ± 0.05	V	1 ^a	Bersten & Hamuy (2009)
11.22 ± 0.06	V	2 ^a	Maguire et al. (2010)
11.27	V	26 ^b	Pejcha & Prieto (2015a)
11.15 ± 0.18	V	15	This work
11.90	r	26 ^b	Pejcha & Prieto (2015a)
11.89 ± 0.16	r	15	This work
12.07	R	26 ^b	Pejcha & Prieto (2015a)
12.07 ± 0.14	R	15	This work
11.95	i	26 ^b	Pejcha & Prieto (2015a)
11.91 ± 0.12	i	15	This work
12.41	I	26 ^b	Pejcha & Prieto (2015a)
12.44 ± 0.11	I	15	This work

^aIt includes the long-rising SN 1987A.

^bOnly six SNe with optical and near-IR photometry in the radioactive tail.

Table 10. Mean ^{56}Ni mass values for normal SNe II.

$\langle M_{56\text{Ni}} \rangle^{\text{unc}\dagger}$ (M_{\odot})	$\hat{\sigma}$ (M_{\odot})	N	$\hat{\sigma}/\sqrt{N}$ (M_{\odot})	N_c^*	Reference [‡]
0.066	0.082	28	0.015	17	B08
0.046	0.048	38	0.008	33	M17
0.042	0.044	107	0.004	75	A19
0.042	0.033	109	0.003	–	This work

[†] $\langle M_{56\text{Ni}} \rangle^{\text{unc}}$ uncorrected for selection bias.

*Number of SNe in common with our full sample (109 SNe).

[‡]B08: Blanc & Greggio (2008); M17: Müller et al. (2017); A19: Anderson (2019), selecting only normal SNe II.

vious estimates are not corrected for selection bias, for the comparison we use our $\langle M_{56\text{Ni}} \rangle^{\text{unc}}$ value. The latter value and those from the aforementioned samples are consistent within $1.6\hat{\sigma}/\sqrt{N}$. It is worth mentioning that the collected $\langle M_{56\text{Ni}} \rangle^{\text{unc}}$ values are not independent since they were computed with SN samples having objects in common. The number of SNe in common between a given set and our full sample is indicated in Column 5. In particular, the similarity between our result and that obtained from the Anderson (2019) sample is because both analyses have 70 per cent of SNe in common.

We also compare the $\log M_{56\text{Ni}}$ values of the SNe in common between our SN set and the samples analysed in Müller et al. (2017), Valenti et al. (2016), and Sharon & Kushnir (2020). Müller et al. (2017) employed the methodology of Pejcha & Prieto (2015a), which computes $\log M_{56\text{Ni}}$ using the luminosity at $\Delta t = 200$ d and equation (3) of Hamuy (2003). Valenti et al. (2016) used

$$M_{56\text{Ni}}/M_{\odot} = 0.075 L_{\text{SN}}^{\text{opt}}(\Delta t) / L_{87\text{A}}^{\text{opt}}(\Delta t), \quad (40)$$

being $L_{\text{SN}}^{\text{opt}}(\Delta t)$ and $L_{87\text{A}}^{\text{opt}}(\Delta t)$ the optical quasi-bolometric luminosity in the radioactive tail of a specific SN and of the long-rising SN 1987A, respectively. Sharon & Kushnir (2020) used the radioactive tail luminosity and the set of equations presented in Wygoda et al. (2019) to derive $\log M_{56\text{Ni}}$. For each sample we compute the differences between its $\log M_{56\text{Ni}}$ measurements, and calculate the mean offset (Δ) and its $\hat{\sigma}$. Then, to track the main source of the observed dispersion, we repeat the previous process, but recomputing our $\log M_{56\text{Ni}}$ values without correcting for the γ -ray leakage (except for Sharon & Kushnir 2020, which in-

Table 11. Mean $\log M_{56\text{Ni}}$ differences between different works.

$\log M_{56\text{Ni}}$ differences [†]	N	Δ (dex)	$\hat{\sigma}$ (dex)
M17–here	33	−0.01	0.29
M17–here(a)	33	0.01	0.28
M17–here(a,b)	33	0.07	0.13
M17–here(a,b,c)	33	0.05	0.08
V16–here	33	−0.15	0.30
V16–here(a,b,c)	33	−0.05	0.14
S20–here	7	−0.09	0.15
S20–here(b,c)	7	0.02	0.05

[†]M17: Müller et al. (2017); S20: Sharon & Kushnir (2020); V16: Valenti et al. (2016); here: this work, uncorrected for γ -ray leakage (a), and using the distance moduli (b) and colour excesses (c) of the comparison work.

cluded this correction) and using the μ and E_{B-V}^h values of the comparison work. The Δ and $\hat{\sigma}$ values are listed in Table 11.

From the comparison with the Müller et al. (2017) sample we obtain $\hat{\sigma} = 0.29$ dex. This value decreases to 0.28 dex when we do not correct for γ -ray leakage, to 0.13 dex when we use the distance moduli of Müller et al. (2017), and to 0.08 dex if we also use their colour excesses. This indicates that differences between our $\log M_{56\text{Ni}}$ estimates and those of Müller et al. (2017) are mainly due to differences in the adopted distance moduli and colour excesses. Therefore, the $\hat{\sigma}$ value of 0.08 dex represents the typical $\log M_{56\text{Ni}}$ error for single SNe due to differences in the methodology used to compute $\log M_{56\text{Ni}}$. For the other two comparison samples we arrive at similar results.

The Δ value from the comparison with the sample of Müller et al. (2017) is equivalent to $3.5\hat{\sigma}/\sqrt{N}$, which indicates the presence of a systematic offset. We note that, of the 0.05 dex offset, 0.03 dex is due to the numerical coefficients of the equation used in Pejcha & Prieto (2015a) to compute $\log M_{56\text{Ni}}$ ¹³. The remaining 0.02 dex is statistically consistent with zero within $1.4\hat{\sigma}/\sqrt{N}$. The Δ values from the comparison with the samples of Valenti et al. (2016) and Sharon & Kushnir (2020) are statistically consistent with zero within 2.0 and $1.0\hat{\sigma}/\sqrt{N}$, respectively.

5.2 Systematics

The models we use in this work (SN II spectra and nucleosynthesis yields) were generated by adopting many approximations and assumptions that help to characterize the underlying complex physical processes of SN explosions. Therefore, our ZP_x^{BC} , $\log M_{56\text{Ni}}$, $\langle M_{56\text{Ni}} \rangle$, and \bar{y}_{Fe} values are potentially affected by systematics on the spectral models, while \bar{y}_{Fe} is also affected by systematics on nucleosynthesis yield models. An analysis and quantification of those systematics is beyond the scope of this study.

5.2.1 Local Hubble-Lemaître constant

The distance moduli of 92 SNe in our sample were estimated as the weighted average of μ_{TF} , μ_{HLL} , and μ_{SVF} (see Sec-

¹³ Equation (3) of Hamuy (2003) is not accurate. To estimate $\log M_{56\text{Ni}}$ we recommend the set of equations presented in Wygoda et al. (2019).

tion 3.6.1). The latter are anchored to Cepheid-calibrated H_0 values of around $75 \text{ km s}^{-1} \text{ Mpc}^{-1}$. If we adopt a TRGB-calibrated H_0 value between 69.6 and $72.4 \text{ km s}^{-1} \text{ Mpc}^{-1}$ (e.g. Freedman et al. 2020; Yuan et al. 2019), then the μ values of our SN sample increase by about 0.08–0.16 mag. In this case, we obtain $\langle M_{56\text{Ni}} \rangle$ values around 0.040–0.044 M_{\odot} . If we assume that the true local H_0 value lies between 71 and $75 \text{ km s}^{-1} \text{ Mpc}^{-1}$ with a uniform probability, then the systematic offset in $\langle M_{56\text{Ni}} \rangle$ induced by the H_0 uncertainty ranges between 0.0 and 0.005 M_{\odot} , with a mean of $0.002 \pm 0.001 M_{\odot}$. This systematic error is lower than that induced by the ZP^{BC} error (0.003 M_{\odot}). Therefore the H_0 uncertainty is not so relevant for our current analysis.

5.2.2 Early dust formation

To compute $\log M_{56\text{Ni}}$ we assumed that the extinction along the SN line of sight is constant for $\Delta t \leq 320$ d. However, normal SNe II are dust factories¹⁴, where the onset of the dust formation is different for each SN. In some cases, the dust formation begins as early as $\Delta t \sim 100$ –200 d (e.g. SN 2007od, Andrews et al. 2010, Inserra et al. 2011; SN 2011ja, Andrews et al. 2016; SN 2017eaw, Rho et al. 2018, Tinyanont et al. 2019). The latter indicates that some normal SNe II may experience a non-negligible increase of the extinction at $\Delta t \leq 320$ d, with a consequent decrease in their ^{56}Ni masses inferred from optical light.

In the case of SN 2007od, the newly formed dust decreases the $\log M_{56\text{Ni}}$ inferred from optical light in ~ 0.8 dex (see Section 4.3.2). On the other hand, for SN 2017eaw (which shows evidence of dust formation at $\Delta t \sim 120$ d, Rho et al. 2018) we measure a $\log M_{56\text{Ni}}$ of -1.087 dex ($M_{56\text{Ni}} = 0.083 M_{\odot}$). This value is about 0.1–0.2 dex greater than the predicted from the NMS relation. Moreover, our $M_{56\text{Ni}}$ estimate is consistent with the ^{56}Ni mass of 0.084 M_{\odot} used in the models found by Rho et al. (2018) to be consistent with the near-IR spectra of SN 2017eaw. Therefore, the early dust formation does not necessarily translate into a non-negligible increase of the extinction.

In the case of strong extinction due to newly formed dust, if it only affects to SNe 2007od, and possibly to SN 2010aj in our set, then the fraction of these events is around 1–2 per cent. Therefore, they should not be a severe contaminant in the mean ^{56}Ni mass of normal SNe II.

5.3 Future improvements

Future works on improving the precision of $\langle M_{56\text{Ni}} \rangle$ should focus on reducing the random and ZP^{BC} errors.

The ZP_x^{BC} values we present in Section 4.2 are based on only 15 SNe, so their errors could be misestimated due to the small sample size. Indeed, the real error on ZP_x^{BC} for the I -band (the preferred one to measure $\log M_{56\text{Ni}}$) can be as low as 0.07 mag or as large as 0.19 mag at a confidence level of 99 per cent¹⁵. Moreover, the small sample size of our

¹⁴ The amount of newly formed dust, however, is still unclear (e.g. Priestley et al. 2020).

¹⁵ Assuming that ZP_I^{BC} has a normal parent distribution with standard deviation σ , for which the quantity $(\hat{\sigma}/\sigma)^2\nu$ has a chi-square distribution with ν degrees of freedom (e.g. Lu 1960).

BC calibration set does not allow us to robustly detect outliers. For example, using the Chauvenet’s criterion, we find that SN 2014G is a possible outlier in the ZP_I^{BC} distribution (Fig. 10). On the other hand, using the Chauvenet’s criterion over 10^4 bootstrap resampling, we find that SN 2014G is consistent with the ZP_I^{BC} distribution in 65 per cent of the realizations. Increasing the number of SNe used to calibrate BCs (i.e. observed at optical and near-IR filters in the radioactive tail) is, therefore, a necessary step to improve the ZP^{BC} error estimation.

One of the current surveys providing optical photometry is the ZTF, which observe about 2300 normal SNe II brighter than 20 mag per year (Feindt et al. 2019). Based on our SN sample, the R -band magnitude of normal SNe II during the first 50 d of the radioactive tail is between 1.5–3.8 mag dimmer than at the maximum light, with an average of 2.5 mag. This means that roughly 3 per cent of all normal SNe II observed by the ZTF have r_{ZTF} photometry useful to estimate $\log M_{56Ni}$ with the radioactive tail photometry. Therefore, it is possible to construct an SN set of similar size to that we used here with two years of ZTF data. Within a few years, the Rubin Observatory Legacy Survey of Space and Time (LSST) will be the main source of photometric data, which will observe $\sim 10^5$ SNe II per year (Lien & Fields 2009). With one year of LSST data (~ 2500 normal SNe II with radioactive tail photometry), it will be feasible to reduce the random error in $\langle M_{56Ni} \rangle$ from 9 per cent (estimated in this work) to around 2 per cent.

The NMS relation provides a method to measure $\log M_{56Ni}$ virtually independent on the radioactive tail photometry. Therefore, the $\log M_{56Ni}$ estimates computed with the radioactive tail luminosity and the NMS relation could be combined to further reduce the random error. Since the transition phase lasts $\lesssim 30$ d, $\log M_{56Ni}$ measurements with the NMS relation require light curves sampled with a cadence of ~ 5 d. As we see in Figure 20, the cadence of the ZTF (around 3 d) is more than enough to estimate the steepness parameter. In the case of the LSST, in order to have light curves sampled with a cadence of ~ 5 d, it will be necessary to combine light curves in different bands into a single one.

Finally, based on the empirical correlation between absolute magnitude and expansion velocity at $\Delta t = 50$ d (v_{50d}) (e.g. Hamuy & Pinto 2002; Hamuy 2003), we expect a relation between $\log M_{56Ni}$, v_{50d} , and S_x . If confirmed, the latter relation will provide a method to measure $\log M_{56Ni}$ independent of the distance and colour excess.

6 SUMMARY AND CONCLUSIONS

In this work we computed the ^{56}Ni masses of 110 normal SNe II from their luminosities in the radioactive tail. To estimate those luminosities we employed the BC technique. We used 15 SNe with $BV(r)R(i)JHK$ photometry and three theoretical spectral models to calibrate the BC values. In order to convert ^{56}Ni masses to iron masses, we used iron isotope ratios of CC nucleosynthesis models. We also analysed the correlation of the ^{56}Ni mass on the steepness parameter and on the absolute magnitude at $\Delta t = 50$ d.

Our main conclusion are the following:

(1) The I - and i -band are best suited to estimate radioac-

tive tail luminosities through the BC technique. In particular, the BC_V value is not constant as reported in previous studies but it is correlated with the $V-I$ colour.

(2) We obtained $\langle M_{56Ni} \rangle = 0.037 \pm 0.005 M_\odot$ for normal SNe II, which translates into a \bar{y}_{Fe} of $0.040 \pm 0.005 M_\odot$. Combining this result with recent mean ^{56}Ni mass measurements for other CC SN subtypes, we estimated a mean CC SN iron yield $< 0.068 M_\odot$. The contribution of normal SNe II to this yield is > 36 per cent.

(3) The relation between $\log M_{56Ni}$ and S_V suggested by Elmhamdi et al. (2003b) is poorly suited to estimate M_{56Ni} . Instead we proposed the NMS method, based on the correlation of $\log M_{56Ni}$ on M_x^{50d} and $\log S_x$, which allows to measure $\log M_{56Ni}$ with a precision of 0.13 dex. Using the r_{ZTF} photometry of 28 normal SNe II from the ZTF BTS, we obtained further evidence supporting the usefulness of the NMS relation to measure $\log M_{56Ni}$.

Future works with ZTF and LSST data during the first years of operation will allow to verify our $\langle M_{56Ni} \rangle$ measurement. In particular, it will be feasible to reduce its random error by a factor of four with one year of LSST data. On the other hand, to reduce the error due to the BC ZP uncertainty, it will be necessary to carry out an observational campaign to increase the number of normal SNe II observed with optical and near-IR filters during the radioactive tail.

ACKNOWLEDGEMENTS

This paper is part of a project that has received funding from the European Research Council (ERC) under the European Union’s Seventh Framework Programme, Grant agreement No. 833031 (PI Dan Maoz). MR thanks the support of the National Agency for Research and Development, ANID-PFCHA/Doctorado-Nacional/2020-21202606. This research has made use of the NASA/IPAC Extragalactic Database (NED) which is operated by the Jet Propulsion Laboratory, California Institute of Technology, under contract with the National Aeronautics and Space Administration. This work has made use of the Weizmann Interactive Supernova Data Repository (<https://www.wiserep.org>).

DATA AVAILABILITY

The data underlying this article will be shared on reasonable request to the corresponding author.

REFERENCES

- Afsariardchi N., et al., 2019, *ApJ*, **881**, 22
Afsariardchi N., Drout M. R., Khatami D., Matzner C. D., Moon D.-S., Ni Y. Q., 2020, arXiv e-prints, p. [arXiv:2009.06683](https://arxiv.org/abs/2009.06683)
Anand G. S., Rizzi L., Tully R. B., 2018, *AJ*, **156**, 105
Anderson J. P., 2019, *A&A*, **628**, A7
Anderson J. P., et al., 2014, *ApJ*, **786**, 67
Andrews J. E., et al., 2010, *ApJ*, **715**, 541
Andrews J. E., et al., 2011, *ApJ*, **731**, 47
Andrews J. E., et al., 2016, *MNRAS*, **457**, 3241
Andrews J. E., et al., 2019, *ApJ*, **885**, 43
Angus J. E., 1994, *Journal of the Royal Statistical Society. Series D (The Statistician)*, **43**, 395

- Arcavi I., et al., 2012, *ApJ*, **756**, L30
- Arcavi I., et al., 2017, *Nature*, **551**, 210
- Arnett W. D., 1982, *ApJ*, **253**, 785
- Barbarino C., et al., 2015, *MNRAS*, **448**, 2312
- Barbon R., Ciatti F., Rosino L., 1982, *A&A*, **116**, 35
- Bayless A. J., et al., 2013, *ApJ*, **764**, L13
- Bellm E. C., et al., 2019, *PASP*, **131**, 018002
- Benetti S., Cappellaro E., Turatto M., 1991, *A&A*, **247**, 410
- Benetti S., Cappellaro E., Turatto M., della Valle M., Mazzali P. A., Gouiffes C., 1994, *A&A*, **285**, 147
- Benetti S., et al., 2001, *MNRAS*, **322**, 361
- Bersten M. C., Hamuy M., 2009, *ApJ*, **701**, 200
- Bersten M. C., Benvenuto O., Hamuy M., 2011, *ApJ*, **729**, 61
- Bessell M., Murphy S., 2012, *PASP*, **124**, 140
- Blanc G., Greggio L., 2008, *New Astron.*, **13**, 606
- Blanton E. L., Schmidt B. P., Kirshner R. P., Ford C. H., Chromey F. R., Herbst W., 1995, *AJ*, **110**, 2868
- Bohlin R. C., Gilliland R. L., 2004, *AJ*, **127**, 3508
- Bose S., et al., 2013, *MNRAS*, **433**, 1871
- Bose S., et al., 2015a, *MNRAS*, **450**, 2373
- Bose S., et al., 2015b, *ApJ*, **806**, 160
- Bose S., Kumar B., Misra K., Matsumoto K., Kumar B., Singh M., Fukushima D., Kawabata M., 2016, *MNRAS*, **455**, 2712
- Bose S., et al., 2018, *ApJ*, **862**, 107
- Bose S., et al., 2019, *ApJ*, **873**, L3
- Bostroem K. A., et al., 2019, *MNRAS*, **485**, 5120
- Bostroem K. A., et al., 2020, *ApJ*, **895**, 31
- Brown P. J., et al., 2009, *AJ*, **137**, 4517
- Bullivant C., et al., 2018, *MNRAS*, **476**, 1497
- Burnham K. P., Anderson D. R., 2002, *Model Selection and Multimodal Inference*, 2nd edn. Springer-Verlag, New York
- Burrows A., Vartanyan D., 2021, *Nature*, **589**, 29
- Buta R. J., 1982, *PASP*, **94**, 578
- Buta R. J., Keel W. C., 2019, *MNRAS*, **487**, 832
- Cappellaro E., Danziger I. J., della Valle M., Gouiffes C., Turatto M., 1995, *A&A*, **293**, 723
- Carlin J. L., et al., 2016, *ApJ*, **828**, L5
- Chauvenet W., 1863, *A manual of spherical and practical astronomy*
- Childress M. J., et al., 2016, *Publ. Astron. Soc. Australia*, **33**, e055
- Cleveland W. S., Grosse E., Shyu W. M., 1992, in Chambers J. M., Hastie T. J., eds., *Statistical models in S*. Chapman and Hall, London, Chapt. 8, pp 309–376
- Clocchiatti A., et al., 1996, *AJ*, **111**, 1286
- Cohen M., Walker R. G., Carter B., Hammersley P., Kidger M., Noguchi K., 1999, *AJ*, **117**, 1864
- Cohen M., Wheaton W. A., Megeath S. T., 2003, *AJ*, **126**, 1090
- Curtis S., Ebinger K., Fröhlich C., Hempel M., Perego A., Liebigdorfer M., Thielemann F.-K., 2019, *ApJ*, **870**, 2
- Dall’Ora M., et al., 2014, *ApJ*, **787**, 139
- Dastidar R., et al., 2018, *MNRAS*, **479**, 2421
- Dastidar R., et al., 2019, *MNRAS*, **490**, 1605
- Dastidar R., et al., 2021, *MNRAS*,
- Dessart L., Hillier D. J., 2011, *MNRAS*, **410**, 1739
- Dessart L., et al., 2008, *ApJ*, **675**, 644
- Dessart L., Hillier D. J., Waldman R., Livne E., 2013, *MNRAS*, **433**, 1745
- Dessart L., Hillier D. J., Woosley S., Livne E., Waldman R., Yoon S.-C., Langer N., 2015, *MNRAS*, **453**, 2189
- Dessart L., Hillier D. J., Woosley S., Livne E., Waldman R., Yoon S.-C., Langer N., 2016, *MNRAS*, **458**, 1618
- Dhungana G., et al., 2016, *ApJ*, **822**, 6
- Dimai A., 2016, *Transient Name Server Discovery Report*, **2016-673**, 1
- Dong Y., et al., 2020, *ApJ*, **906**, 56
- Elias-Rosa N., et al., 2011, *ApJ*, **742**, 6
- Elmhamdi A., et al., 2003a, *MNRAS*, **338**, 939
- Elmhamdi A., Chugai N. N., Danziger I. J., 2003b, *A&A*, **404**, 1077
- Faran T., et al., 2014a, *MNRAS*, **442**, 844
- Faran T., et al., 2014b, *MNRAS*, **445**, 554
- Feindt U., Nordin J., Rigault M., Brinnel V., Dhawan S., Goobar A., Kowalski M., 2019, *J. Cosmology Astropart. Phys.*, **2019**, 005
- Fitzpatrick E. L., 1999, *PASP*, **111**, 63
- Förster F., et al., 2018, *Nature Astronomy*, **2**, 808
- Förster F., et al., 2021, *AJ*, **161**, 242
- Foster C., et al., 2014, *MNRAS*, **442**, 3544
- Fraser M., et al., 2011, *MNRAS*, **417**, 1417
- Freedman W. L., et al., 2019, *ApJ*, **882**, 34
- Freedman W. L., et al., 2020, *ApJ*, **891**, 57
- Fremling C., et al., 2020, *ApJ*, **895**, 32
- Fukugita M., Ichikawa T., Gunn J. E., Doi M., Shimasaku K., Schneider D. P., 1996, *AJ*, **111**, 1748
- Gal-Yam A., 2017, *Observational and Physical Classification of Supernovae*. p. 195, doi:10.1007/978-3-319-21846-5-35
- Galbany L., et al., 2016, *AJ*, **151**, 33
- Graham M. J., et al., 2019, *PASP*, **131**, 078001
- Graziani R., Courtois H. M., Lavaux G., Hoffman Y., Tully R. B., Copin Y., Pomarède D., 2019, *MNRAS*, **488**, 5438
- Gurugubelli U. K., Sahu D. K., Anupama G. C., Chakradhari N. K., 2008, *Bulletin of the Astronomical Society of India*, **36**, 79
- Gutiérrez C. P., et al., 2017a, *ApJ*, **850**, 89
- Gutiérrez C. P., et al., 2017b, *ApJ*, **850**, 90
- Gutiérrez C. P., et al., 2020, *MNRAS*, **496**, 95
- Hamuy M. A., 2001, PhD thesis, The University of Arizona
- Hamuy M., 2003, *ApJ*, **582**, 905
- Hamuy M., Pinto P. A., 2002, *ApJ*, **566**, L63
- Hamuy M., Suntzeff N. B., Gonzalez R., Martin G., 1988, *AJ*, **95**, 63
- Harutyunyan A. H., et al., 2008, *A&A*, **488**, 383
- Hayes D. S., Latham D. W., 1975, *ApJ*, **197**, 593
- Hendry M. A., et al., 2005, *MNRAS*, **359**, 906
- Hendry M. A., et al., 2006, *MNRAS*, **369**, 1303
- Hicken M., et al., 2017, *ApJS*, **233**, 6
- Hoeflich P., 2017, *Explosion Physics of Thermonuclear Supernovae and Their Signatures*. p. 1151, doi:10.1007/978-3-319-21846-5-56
- Hosseinizadeh G., et al., 2018, *ApJ*, **861**, 63
- Huang F., et al., 2015, *ApJ*, **807**, 59
- Huang F., et al., 2016, *ApJ*, **832**, 139
- Huang F., et al., 2018, *MNRAS*, **475**, 3959
- Inserra C., et al., 2011, *MNRAS*, **417**, 261
- Inserra C., et al., 2012, *MNRAS*, **422**, 1122
- Inserra C., et al., 2013, *A&A*, **555**, A142
- Itagaki K., 2016, *Transient Name Server Discovery Report*, **2016-234**, 1
- Iwamoto K., Brachwitz F., Nomoto K., Kishimoto N., Umeda H., Hix W. R., Thielemann F.-K., 1999, *ApJS*, **125**, 439
- Jang I. S., Lee M. G., 2017, *ApJ*, **836**, 74
- Jeffery D. J., 1999, arXiv e-prints, pp astro-ph/9907015
- Jerkstrand A., Fransson C., Kozma C., 2011, *A&A*, **530**, A45
- Jerkstrand A., Smartt S. J., Fraser M., Fransson C., Sollerman J., Taddia F., Kotak R., 2014, *MNRAS*, **439**, 3694
- Kobayashi C., Umeda H., Nomoto K., Tominaga N., Ohkubo T., 2006, *ApJ*, **653**, 1145
- Kourkchi E., Courtois H. M., Graziani R., Hoffman Y., Pomarède D., Shaya E. J., Tully R. B., 2020, *AJ*, **159**, 67
- Kozyreva A., Nakar E., Waldman R., 2019, *MNRAS*, **483**, 1211
- Krisciunas K., et al., 2009, *AJ*, **137**, 34
- Leonard D. C., et al., 2002, *AJ*, **124**, 2490
- Li W., Wang X., Van Dyk S. D., Cuilland re J.-C., Foley R. J., Filippenko A. V., 2007, *ApJ*, **661**, 1013
- Li W., et al., 2011, *MNRAS*, **412**, 1441

- Liao J., Sun G., Gao X., 2019, Transient Name Server Discovery Report, [2019-1124](#), 1
- Liddle A. R., 2007, *MNRAS*, **377**, L74
- Lien A., Fields B. D., 2009, *J. Cosmology Astropart. Phys.*, **2009**, 047
- Lisakov S. M., Dessart L., Hillier D. J., Waldman R., Livne E., 2017, *MNRAS*, **466**, 34
- Lu J. Y., 1960, *Journal of Farm Economics*, **42**, 910
- Lusk J. A., Baron E., 2017, *PASP*, **129**, 044202
- Maguire K., et al., 2010, *MNRAS*, **404**, 981
- Maoz D., Graur O., 2017, *ApJ*, **848**, 25
- McQuinn K. B. W., Skillman E. D., Dolphin A. E., Berg D., Kennicutt R., 2017, *AJ*, **154**, 51
- Meikle W. P. S., et al., 2011, *ApJ*, **732**, 109
- Meza N., Anderson J. P., 2020, *A&A*, **641**, A177
- Minkowski R., 1941, *PASP*, **53**, 224
- Misra K., Pooley D., Chandra P., Bhattacharya D., Ray A. K., Sagar R., Lewin W. H. G., 2007, *MNRAS*, **381**, 280
- Monachesi A., Bell E. F., Radburn-Smith D. J., Bailin J., de Jong R. S., Holwerda B., Streich D., Silverstein G., 2016, *MNRAS*, **457**, 1419
- Morozova V., Piro A. L., Valenti S., 2018, *ApJ*, **858**, 15
- Müller-Bravo T. E., et al., 2020, *MNRAS*, **497**, 361
- Müller T., Prieto J. L., Pejcha O., Clocchiatti A., 2017, *ApJ*, **841**, 127
- Munari U., Henden A., Belligoli R., Castellani F., Cherini G., Righetti G. L., Vagnozzi A., 2013, *New Astron.*, **20**, 30
- Nakaoka T., et al., 2018, *ApJ*, **859**, 78
- Nomoto K., Hashimoto M., Tsujimoto T., Thielemann F. K., Kishimoto N., Kubo Y., Nakasato N., 1997, *Nuclear Phys. A*, **616**, 79
- Olivares E. F., et al., 2010, *ApJ*, **715**, 833
- Pastorello A., et al., 2004, *MNRAS*, **347**, 74
- Pastorello A., et al., 2006, *MNRAS*, **370**, 1752
- Pastorello A., et al., 2007, *MNRAS*, **376**, 1301
- Pastorello A., et al., 2009a, *MNRAS*, **394**, 2266
- Pastorello A., et al., 2009b, *A&A*, **500**, 1013
- Pejcha O., Prieto J. L., 2015a, *ApJ*, **799**, 215
- Pejcha O., Prieto J. L., 2015b, *ApJ*, **806**, 225
- Pennypacker C. R., et al., 1989, *AJ*, **97**, 186
- Perley D. A., et al., 2020, *ApJ*, **904**, 35
- Phillips M. M., et al., 2013, *ApJ*, **779**, 38
- Pignata G., 2013, in *Massive Stars: From alpha to Omega*. p. 176
- Poznanski D., Prochaska J. X., Bloom J. S., 2012, *MNRAS*, **426**, 1465
- Pozzo M., et al., 2006, *MNRAS*, **368**, 1169
- Priestley F. D., Bevan A., Barlow M. J., De Looze I., 2020, *MNRAS*, **497**, 2227
- Pumo M. L., Zampieri L., 2011, *ApJ*, **741**, 41
- Pumo M. L., Zampieri L., 2013, *MNRAS*, **434**, 3445
- Quimby R. M., Wheeler J. C., Höflich P., Akerlof C. W., Brown P. J., Rykoff E. S., 2007, *ApJ*, **666**, 1093
- Reguitti A., et al., 2021, *MNRAS*, **501**, 1059
- Rho J., Geballe T. R., Banerjee D. P. K., Dessart L., Evans A., Joshi V., 2018, *ApJ*, **864**, L20
- Richmond M. W., 2014, *Journal of the American Association of Variable Star Observers (JAAVSO)*, **42**, 333
- Riess A. G., et al., 2016, *ApJ*, **826**, 56
- Riess A. G., Casertano S., Yuan W., Macri L. M., Scolnic D., 2019, *ApJ*, **876**, 85
- Rizzi L., Tully R. B., Makarov D., Makarova L., Dolphin A. E., Sakai S., Shaya E. J., 2007, *ApJ*, **661**, 815
- Rodríguez Ó., Clocchiatti A., Hamuy M., 2014, *AJ*, **148**, 107
- Rodríguez Ó., et al., 2019, *MNRAS*, **483**, 5459
- Rodríguez Ó., et al., 2020, *MNRAS*, **494**, 5882
- Roy R., et al., 2011a, *MNRAS*, **414**, 167
- Roy R., et al., 2011b, *ApJ*, **736**, 76
- Rubenstein E. P., 1999, *IAU Circ.*, **7319**, 2
- Rubin A., et al., 2016, *ApJ*, **820**, 33
- Ruiz-Lapuente P., Kidger M., Lopez R., Canal R., 1990, *AJ*, **100**, 782
- Saha A., Thim F., Tammann G. A., Reindl B., Sand age A., 2006, *ApJS*, **165**, 108
- Sahu D. K., Anupama G. C., Srividya S., Muneer S., 2006, *MNRAS*, **372**, 1315
- Sanders N. E., et al., 2015, *ApJ*, **799**, 208
- Schlafly E. F., Finkbeiner D. P., 2011, *ApJ*, **737**, 103
- Schlegel E. M., 1990, *MNRAS*, **244**, 269
- Schlegel D. J., Finkbeiner D. P., Davis M., 1998, *ApJ*, **500**, 525
- Schmidt B. P., et al., 1993, *AJ*, **105**, 2236
- Scholz F. W., Stephens M. A., 1987, *Journal of the American Statistical Association*, **82**, 918
- Schwarz G., 1978, *Annals of Statistics*, **6**, 461
- Sharon A., Kushnir D., 2020, *MNRAS*, **496**, 4517
- Shaya E. J., Tully R. B., Hoffman Y., Pomarède D., 2017, *ApJ*, **850**, 207
- Shivvers I., et al., 2017, *PASP*, **129**, 054201
- Silverman J. M., et al., 2017, *MNRAS*, **467**, 369
- Singh A., Srivastav S., Kumar B., Anupama G. C., Sahu D. K., 2018, *MNRAS*, **480**, 2475
- Singh A., Kumar B., Moriya T. J., Anupama G. C., Sahu D. K., Brown P. J., Andrews J. E., Smith N., 2019, *ApJ*, **882**, 68
- Smartt S. J., 2009, *ARA&A*, **47**, 63
- Smartt S. J., 2015, *Publ. Astron. Soc. Australia*, **32**, e016
- Spiro S., et al., 2014, *MNRAS*, **439**, 2873
- Stritzinger M., Suntzeff N. B., Hamuy M., Challis P., Demarco R., Germany L., Soderberg A. M., 2005, *PASP*, **117**, 810
- Sukhbold T., Ertl T., Woosley S. E., Brown J. M., Janka H. T., 2016, *ApJ*, **821**, 38
- Suwa Y., Tominaga N., Maeda K., 2019, *MNRAS*, **483**, 3607
- Szalai T., et al., 2019, *ApJ*, **876**, 19
- Taddia F., et al., 2016, *A&A*, **588**, A5
- Takáts K., et al., 2014, *MNRAS*, **438**, 368
- Takáts K., et al., 2015, *MNRAS*, **450**, 3137
- Tartaglia L., et al., 2018, *ApJ*, **853**, 62
- Tartaglia L., et al., 2021, *ApJ*, **907**, 52
- Terreran G., et al., 2016, *MNRAS*, **462**, 137
- Terreran G., et al., 2017, *Nature Astronomy*, **1**, 713
- Thompson L. A., 1982, *ApJ*, **257**, L63
- Tikhonov N. A., Galazutdinova O. A., 2020, *Astrophysical Bulletin*, **75**, 384
- Tinyanont S., et al., 2019, *ApJ*, **873**, 127
- Tomasella L., et al., 2013, *MNRAS*, **434**, 1636
- Tomasella L., et al., 2018, *MNRAS*, **475**, 1937
- Tsvetkov D. Y., 1983, *Peremennye Zvezdy*, **22**, 39
- Tsvetkov D. Y., 2014, *Peremennye Zvezdy*, **34**, 2
- Tsvetkov D. Y., Volnova A. A., Shulga A. P., Korotkiy S. A., Elmhamdi A., Danziger I. J., Ereshko M. V., 2006, *A&A*, **460**, 769
- Tsvetkov D. Y., Muminov M., Burkhanov O., Kahharov B., 2007, *Peremennye Zvezdy*, **27**, 5
- Tsvetkov D. Y., et al., 2018, *Astronomy Letters*, **44**, 315
- Tsvetkov D. Y., et al., 2019, *MNRAS*, **487**, 3001
- Tully R. B., Rizzi L., Shaya E. J., Courtois H. M., Makarov D. I., Jacobs B. A., 2009, *AJ*, **138**, 323
- Turatto M., Cappellaro E., Benetti S., Danziger I. J., 1993, *MNRAS*, **265**, 471
- Turatto M., et al., 1998, *ApJ*, **498**, L129
- Uglikano M., Janka H.-T., Marek A., Arcones A., 2012, *ApJ*, **757**, 69
- Valenti S., et al., 2015, *MNRAS*, **448**, 2608
- Valenti S., et al., 2016, *MNRAS*, **459**, 3939
- Van Dyk S. D., 2013, *AJ*, **146**, 24
- Van Dyk S. D., et al., 2012, *AJ*, **143**, 19
- Van Dyk S. D., et al., 2019, *ApJ*, **875**, 136
- Vinkó J., et al., 2006, *MNRAS*, **369**, 1780

- Vinkó J., et al., 2009, *ApJ*, **695**, 619
- Weaver T. A., Woosley S. E., 1980, in Ninth Texas Symposium on Relativistic Astrophysics. pp 335–357, doi:10.1111/j.1749-6632.1980.tb15942.x
- Wiggins P., 2017, Transient Name Server Discovery Report, 2017-548, 1
- Woosley S. E., Weaver T. A., 1995, *ApJS*, **101**, 181
- Wygoda N., Elbaz Y., Katz B., 2019, *MNRAS*, **484**, 3941
- Wyrzykowski L., et al., 2014, *Acta Astron.*, **64**, 197
- Yaron O., et al., 2017, *Nature Physics*, **13**, 510
- Young T. R., 2004, *ApJ*, **617**, 1233
- Yuan F., et al., 2016, *MNRAS*, **461**, 2003
- Yuan W., Riess A. G., Macri L. M., Casertano S., Scolnic D. M., 2019, *ApJ*, **886**, 61
- Zgirski B., et al., 2017, *ApJ*, **847**, 88
- Zhang T., Wang X., Li W., Zhou X., Ma J., Jiang Z., Chen J., 2006, *AJ*, **131**, 2245
- Zhang J., et al., 2014, *ApJ*, **797**, 5
- de Jaeger T., et al., 2019, *MNRAS*, **490**, 2799
- de Jaeger T., Stahl B. E., Zheng W., Filippenko A. V., Riess A. G., Galbany L., 2020, *MNRAS*, **496**, 3402

APPENDIX A: SYNTHETIC MAGNITUDES

Given a SED f_λ (in $\text{erg s}^{-1} \text{cm}^{-2} \text{\AA}^{-1}$), we can compute the synthetic magnitude in the x -band using

$$m_x = -2.5 \log \int d\lambda S_{x,\lambda} \frac{\lambda f_\lambda}{hc} + ZP_x^{\text{mag}} \quad (\text{A1})$$

(e.g. Hamuy 2001). Here λ is the observed wavelength (in \AA), $S_{x,\lambda}$ is the peak-normalized x -band transmission function (considering a photon-counting detector), $hc = 1.986 \times 10^{-8} \text{ erg \AA}$, and ZP_x^{mag} is the zero-point for the magnitude system. To compute ZP_x^{mag} values in the Vega system, we use equation (A1) along with the Vega SED published by Bohlin & Gilliland (2004)¹⁶ and the Vega magnitudes published by Fukugita et al. (1996): $B = 0.03$, $V = 0.03$, and $I = 0.024 \text{ mag}$, and by Cohen et al. (1999): $J = -0.001$, $H = 0.000$, and $K = -0.001 \text{ mag}$. For Johnson-Kron-Cousins *BVRI* bands we adopt the transmission functions given in Stritzinger et al. (2005), while for 2MASS *JHK* bands we adopt the transmission of Cohen et al. (2003)¹⁷. To compute ZP_x^{mag} values in the AB system, we use equation (A1), $f_\lambda = 1/\lambda^2$, and $m_x = -2.408$. For the Sloan *gri* bands we use the transmission functions of the SDSS Data Release 7¹⁸. To compute the r_{ZTF} transmission function, we use equation (1) of Pastorello et al. (2007), adopting the corresponding ZTF filter transmission¹⁷ and CCD quantum efficiency¹⁹, the atmospheric extinction at Palomar Observatory of Hayes & Latham (1975) (assuming an airmass of 1.2) combined with atmospheric telluric lines, a standard aluminium reflectivity curve, and a constant lens throughput. Column 3 of Table A1 lists the ZP_x^{mag} values.

¹⁶ https://ssb.stsci.edu/cdbs/current_calspec/alpha_lyr_stis_010.fits

¹⁷ Since they consider an energy-counting detector, we have to divide the transmissions by λ before to use them in equation (A1).

¹⁸ <http://classic.sdss.org/dr7/instruments/imager/index.html>

¹⁹ https://github.com/ZwickyTransientFacility/ztf_information

Table A1. Properties of the filters used in this work.

x	System	ZP_x^{mag} (mag)	ZP_x^{flux} (mag)	$\bar{\lambda}_x$ (\AA)	$R_{\bar{\lambda}_x}$	R_x^{pt}
B	Vega	15.300	-20.462	4610	3.86	3.99
g	AB	15.329	-20.770	4860	3.62	3.68
V	Vega	14.865	-21.074	5600	2.96	3.04
r	AB	14.986	-21.361	6330	2.49	2.55
r_{ZTF}	AB	15.212	-21.436	6490	2.40	2.45
R	Vega	15.053	-21.629	6610	2.33	2.40
i	AB	14.710	-21.780	7450	1.93	1.91
I	Vega	14.538	-22.354	8090	1.68	1.71
J	Vega	13.729	-23.787	12470	0.80	0.80
H	Vega	13.412	-24.886	16520	0.51	0.51
K	Vega	12.691	-25.948	21630	0.35	0.35

APPENDIX B: PHOTOMETRIC SED

To compute pSEDs, we need to convert x -band magnitudes to monochromatic fluxes \bar{f}_x (in $\text{erg s}^{-1} \text{cm}^{-2} \text{\AA}^{-1}$). For this, we use $f_\lambda = \bar{f}_x$ in equation (A1), thus obtaining

$$\bar{f}_x = 10^{-0.4(m_x - ZP_x^{\text{flux}})}, \quad (\text{B1})$$

where

$$ZP_x^{\text{flux}} = 2.5 \log \int d\lambda S_{x,\lambda} \frac{\lambda}{hc} + ZP_x^{\text{mag}}. \quad (\text{B2})$$

Values of ZP_x^{flux} are reported in Column 4 of Table A1.

The effective wavelength of the x -band as a function of the SED is given by

$$\lambda_x = \frac{\int d\lambda S_{x,\lambda} \lambda^2 f_\lambda}{\int d\lambda S_{x,\lambda} \lambda f_\lambda} \quad (\text{B3})$$

(e.g. Bessell & Murphy 2012). To estimate this value for the *BVRIJHK* bands, we use the theoretical spectral models of D13, J14, and L17 during the radioactive tail, adopting the median as the representative effective wavelength $\bar{\lambda}_x$. These values are summarized in Column 5 of Table A1. In Column 6 we report the total-to-selective extinction ratio for $\bar{\lambda}_x$ ($R_{\bar{\lambda}_x}$), assuming the extinction curve of Fitzpatrick (1999) with $R_V = 3.1$. We also compute the $R_{\bar{\lambda}_x}$ values for the photospheric and transition phase (R_x^{pt}). Those values are listed in Column 7 of Table A1.

To obtain monochromatic fluxes corrected for reddening (\bar{f}_x^{corr}) we use

$$\bar{f}_x^{\text{corr}} = \bar{f}_x \cdot 10^{0.4(E_{B-V}^G + E_{B-V}^h)R_{\bar{\lambda}_x}}. \quad (\text{B4})$$

Using the set of ($\bar{\lambda}_x$, \bar{f}_x^{corr}) values, we construct the pSED, from which the quasi-bolometric flux is computed with the trapezoidal rule, i.e.,

$$F^{BVRIJHK} = \frac{1}{2} \sum_{i=1}^6 (\bar{\lambda}_{x_{i+1}} - \bar{\lambda}_{x_i}) (\bar{f}_{x_{i+1}}^{\text{corr}} + \bar{f}_{x_i}^{\text{corr}}), \quad (\text{B5})$$

where $x_j = B, V, R, I, J, H, K$ for $j = 1, \dots, 7$. The error on $F^{BVRIJHK}$ due to error in photometry, σ_{m_x} , is given by

$$\sigma_{F^{BVRIJHK}} = \frac{\ln(10)}{5} \left([(\bar{\lambda}_{x_1} - \bar{\lambda}_{x_2}) \bar{f}_{x_1}^{\text{corr}} \sigma_{m_{x_1}}]^2 + \sum_{i=2}^6 [(\bar{\lambda}_{x_{i+1}} - \bar{\lambda}_{x_{i-1}}) \bar{f}_{x_i}^{\text{corr}} \sigma_{m_{x_i}}]^2 + [(\bar{\lambda}_{x_7} - \bar{\lambda}_{x_6}) \bar{f}_{x_7}^{\text{corr}} \sigma_{m_{x_7}}]^2 \right)^{1/2}. \quad (\text{B6})$$

To estimate the error on F^{BVRJHK} due to uncertainties on E_{B-V}^G and E_{B-V}^h , we define the pSED total-to-selective extinction ratio as

$$R_p = -\frac{2.5}{E_{B-V}^G + E_{B-V}^h} \log \left(\frac{F_{\text{unc}}^{BVRJHK}}{F^{BVRJHK}} \right). \quad (\text{B7})$$

Here F_{unc}^{BVRJHK} is the quasi-bolometric flux uncorrected for E_{B-V}^G and E_{B-V}^h , i.e., replacing \bar{f}_x^{corr} in equation (B5) by \bar{f}_x . With this, the error on F^{BVRJHK} due to the uncertainties on E_{B-V}^G and E_{B-V}^h , in magnitude scale, is

$$\sigma(2.5 \log(F^{BVRJHK})) = R_p \sqrt{\sigma_{E_{B-V}^G}^2 + \sigma_{E_{B-V}^h}^2}. \quad (\text{B8})$$

APPENDIX C: MODEL SELECTION

Let a set of N data $X_i = \{x_i, y_i, \sigma_{y_i}\}$ ($i = 1, \dots, N$) and a set of M models $\{f_{j,\theta}\}$ ($j = 1, \dots, M$) with parameters θ . To select the model that best represents the data, we use the Bayesian information criterion (BIC, Schwarz 1978), performing the following procedure. First, we compute the parameters θ of each model, maximizing its log-likelihood

$$\ln \mathcal{L}(f_{j,\theta}|X_i) = -\frac{1}{2} \sum_i^N \left[\ln(\sigma_i^2) + \frac{(y_i - f_{j,\theta}(x_i))^2}{\sigma_i^2} \right], \quad (\text{C1})$$

where $\sigma_i^2 = \sigma_{y_i}^2 + \sigma_0^2$, being σ_0 the error not accounted for the errors in y_i . Next, for each model we compute

$$\text{BIC}_j = -2 \ln \mathcal{L}_j^{\text{max}} + k \ln N \quad (\text{C2})$$

(Schwarz 1978), where $\ln \mathcal{L}_j^{\text{max}}$ is the maximum log-likelihood and k is the number of free parameters. Then, we evaluate the Bayesian weights

$$p_j = e^{-0.5(\text{BIC}_j - \text{BIC}_l)} \left(\sum_{m=1}^M e^{-0.5(\text{BIC}_m - \text{BIC}_l)} \right)^{-1} \quad (\text{C3})$$

(Burnham & Anderson 2002), where l is the index of the model with the lowest BIC value. As reference, if $p_l/p_j > 13.0$ (e.g. Liddle 2007), then there is a strong evidence in favour of the l th model over the j th one. Finally, among all models with $p_l/p_j \leq 13.0$, by the principle of parsimony, we select the one with less parameters.

In the case of least-square regressions (e.g. when σ_{y_i} values are not available), we replace equation (C2) by

$$\text{BIC}_j = \ln(s_j^2) + k/N \cdot \ln N \quad (\text{C4})$$

(e.g. Rodríguez et al. 2019), where s_j^2 is the average of the squared residuals around the j th model.

APPENDIX D: ^{56}Ni MASS EQUATION

Let a normal SN II with a set of N measurements of $\{m_{x,i}\}$ magnitudes (K -corrected, see Appendix I) at times t_i , and a set of parameters $\{t_0, \mu, E_{B-V}^G, E_{B-V}^h, z_{\text{helio}}^{\text{SN}}\}$. The ^{56}Ni mass (in M_{\odot}) can be computed using equations (17) and (18), which can be written as

$$\log M_{56\text{Ni}} = \langle A_i - D_i \rangle + B. \quad (\text{D1})$$

Here the angle brackets denote the value that maximizes the log-likelihood of a constant-only model (equation C1) where, using $\text{BC}_x = \text{ZP}_x^{\text{BC}} + \beta_x \Delta t / 100 \text{ d}$,

$$A_i = -\frac{m_{x,i}}{2.5} + \frac{(0.39 - \beta_x / 2.5) t_i}{(1 + z_{\text{helio}}^{\text{SN}}) 100 \text{ d}}, \quad (\text{D2})$$

$$B = \frac{\mu - \text{ZP}_x^{\text{BC}} + A_x^{\text{tot}}}{2.5} - \frac{(0.39 - \beta_x / 2.5) t_0}{(1 + z_{\text{helio}}^{\text{SN}}) 100 \text{ d}} - 3.076, \quad (\text{D3})$$

where $A_x^{\text{tot}} = (E_{B-V}^G + E_{B-V}^h) R_{\lambda_x}$. To evaluate whether it is necessary to include the D_i correction in equation (D1), we have to check the constancy of the $\log M_{56\text{Ni}}$ estimates with respect to t_i . For this, we use the model selection procedure given in Appendix C using the $\{t_i, A_i, \sigma_{A_i}\}$ data along with a zero-order and a linear polynomial. If data can be represented by a zero-order polynomial, then $D_i = 0$ in equation (D1). In this case, the $\log M_{56\text{Ni}}$ error is given by

$$\sigma_{\log M_{56\text{Ni}}} = \sqrt{\sigma_{\langle A_i \rangle}^2 + \sigma_B^2}. \quad (\text{D4})$$

Here

$$\sigma_B^2 = \frac{\sigma_{\mu}^2 + \sigma_{\text{ZP}_x^{\text{BC}}}^2 + \sigma_{A_x^{\text{tot}}}^2}{6.25} + \left[\frac{(0.39 - \beta_x / 2.5) \sigma_{t_0}}{(1 + z_{\text{helio}}^{\text{SN}}) 100 \text{ d}} \right]^2, \quad (\text{D5})$$

where σ denotes the error in the subscripted quantity, and $\sigma_{\langle A_i \rangle} = \hat{\sigma}_{A,k} / \sqrt{N}$, being

$$\hat{\sigma}_{A,k} = \left[\frac{1}{N-k} \sum_i^N (X_i - \langle X_i \rangle)^2 \right]^{1/2} \quad (\text{D6})$$

the sample standard deviation, and k the number of free parameters.

If data are not well represented by a zero-order polynomial, then there is a dependence of the $\log M_{56\text{Ni}}$ estimates on t_i , so we have to include the D_i term. If the time derivative of A is negative as in the case of SN 2014G (left-hand side of Fig. 11), then we use the $D_i(T_0)$ term given by equations (19) and (20). The value of T_0 is computed through a log-likelihood maximization (equation C1). Once the value of T_0 is determined, we compute $\log M_{56\text{Ni}}$ using equation (D1) and $D_i = D_i(T_0)$. The error in $\log M_{56\text{Ni}}$ is given by equation (D4) replacing $\sigma_{\langle A_i \rangle}$ by $\hat{\sigma}_{A-D,k} / \sqrt{N}$ if the $\log M_{56\text{Ni}}$ estimates are independent on t_i (using the procedure given in Appendix C), otherwise we replace $\sigma_{\langle A_i \rangle}$ by $\hat{\sigma}_{A-D,k}$. If the time derivative of A is positive as in the case of SN 2005cs (Fig. 12), then we assume the result obtained with $D_i = 0$, and $\sigma_{\langle A_i \rangle} = \hat{\sigma}_{A,k}$ in equation (D4).

APPENDIX E: LOG-NORMAL MEAN

Let the quantity x (e.g. $M_{56\text{Ni}}$, D , S_x) and its log-transformation $y = \log x$. If y has a normal PDF with mean \bar{y} and standard deviation σ_y , then x has a log-normal distribution. The mean of the latter PDF (\bar{x}) is not $10^{\bar{y}}$ (which indeed is the median) but

$$\bar{x} = 10^{\bar{y} + 0.5 \ln(10) \sigma_y^2} \quad (\text{E1})$$

(e.g. Angus 1994). The standard deviation of the x PDF is

$$\sigma_x = |\bar{x}| \sqrt{10^{\ln(10) \sigma_y^2} - 1}. \quad (\text{E2})$$

On the other hand, if x has a normal PDF then \bar{y} is not $\log \bar{x}$ but

$$\bar{y} = \log \bar{x} - 0.5 \log(1 + (\sigma_x/\bar{x})^2), \quad (\text{E3})$$

while the standard deviation of the y PDF is

$$\sigma_y = \sqrt{\ln(1 + (\sigma_x/\bar{x})^2) / \ln(10)}. \quad (\text{E4})$$

APPENDIX F: C3 METHOD

The C3 method (Rodríguez et al. 2014, 2019) relies on the assumption that, during the plateau phase, all normal SNe II have similar linear $V-I$ versus $B-V$ C3s. For an SN with a measurement of $V-I$ and $B-V$ (corrected for E_{B-V}^G and K -correction, e.g. Rodríguez et al. 2019) at time t_i (during the plateau phase), the host galaxy color excess is given by

$$E_{B-V,i}^h = A_i + ZP_{C3}. \quad (\text{F1})$$

Here ZP_{C3} is the zero-point for the C3 method, and

$$A_i = [(V-I)_i - m_{C3} \cdot (B-V)_i] / (R_V - R_I - m_{C3}) \quad (\text{F2})$$

(e.g. Rodríguez et al. 2019), where $R_V = 3.1$, $R_I = 1.72$, and $m_{C3} = 0.45 \pm 0.07$ is the $V-I$ versus $B-V$ C3 slope (Rodríguez et al. 2019). For an SN with a set of N measurements of $\{(B-V)_i, (V-I)_i\}$, the E_{B-V}^h value is given by

$$E_{B-V}^h = \langle A_i \rangle + ZP_{C3}, \quad (\text{F3})$$

where the angle brackets denote the value that maximizes the log-likelihood of a constant-only model (equation C1).

The ZP_{C3} value can be computed from a set of reddening-free SNe. For each of those SNe, following equation (F3), we have $ZP_{C3}^{\text{SN}} = -\langle A_i \rangle^{\text{SN}}$. Using this set of ZP_{C3}^{SN} values, we calculate the mean and the $\hat{\sigma}$ value, which we adopt as ZP_{C3} and its error, respectively. To determine ZP_{C3} we use SNe 2005ay, 2008gz, 2013ej, and 2014cx, which are found to have low reddening by other methods (see Table L3), and SN 2003bn (Galbany et al. 2016), which is also affected by low reddening (e.g. Olivares E. et al. 2010). Using those SNe, we obtain $ZP_{C3} = -0.116 \pm 0.024$ mag. This value is equivalent to the ZP_{C3} inferred by Rodríguez et al. (2019) from SNe 2003bn and 2013ej, but with a lower error as we use more SNe to determine the ZP_{C3} value.

The expression for the E_{B-V}^h error is

$$\sigma_{E_{B-V}^h} = \sqrt{\hat{\sigma}_{A,k}^2 + \sigma_{ZP_{C3}}^2 + \sigma_m^2}, \quad (\text{F4})$$

where $\hat{\sigma}_{A,k}$ is given by equation (D6), and

$$\sigma_m = \left| \frac{E_{B-V}^h - \langle (B-V)_i \rangle + \langle (B-V)_i^{\text{ZP}} \rangle}{R_V - R_I - m_{C3}} \right| \sigma_{m_{C3}} \quad (\text{F5})$$

is the error induced by the m_{C3} uncertainty. In the latter expression, $\langle (B-V)_i^{\text{ZP}} \rangle = 1.065$ is the mean $\langle (B-V)_i^{\text{ZP}} \rangle$ value of the five SNe we use to calibrate the C3 method.

For example, Fig. F1 shows the $E_{B-V,i}^h$ estimates for SN 2009N obtained with the C3 method. For that SN we compute $E_{B-V}^h = 0.277 \pm 0.082$ mag.

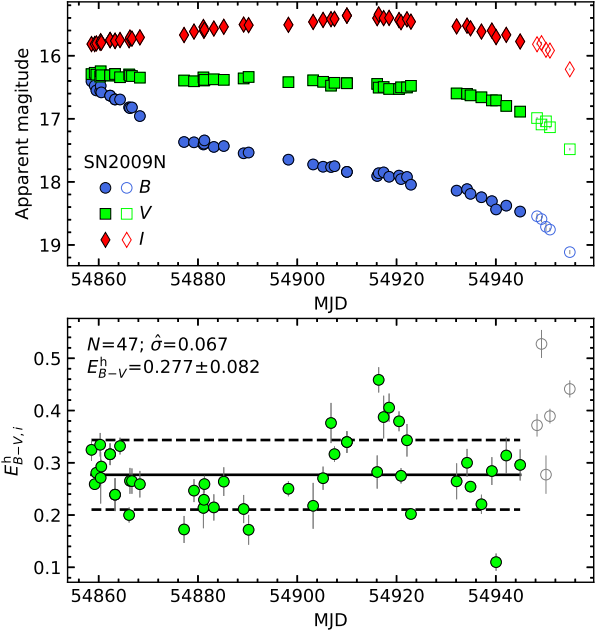


Figure F1. Top panel: BVI light curves of SN 2009N during the plateau phase. Bottom panel: $E_{B-V,i}^h$ estimates obtained with the C3 method. Filled symbols are the data used to compute E_{B-V}^h . The solid line corresponds to the E_{B-V}^h value that maximizes the likelihood, and dashed lines are the $\pm 1\hat{\sigma}$ limits around E_{B-V}^h . Error bars are 1σ errors due to uncertainties on photometry.

APPENDIX G: SPECTROSCOPIC REDDENING

Let a set of N SN spectra $\{f_i\}$ corrected for E_{B-V}^G and $z_{\text{helio}}^{\text{SN}}$, where each spectrum has a dispersion Δ_i (in $\text{\AA}/\text{pixel}$) and n_i flux measurements at wavelengths $\lambda_{i,k}$ ($k = 1, \dots, n_i$), and a set of M reddening-free spectra $\{F_j\}$. For each $\{f_i, F_j\}$ combination, the E_{B-V}^h value can be inferred minimizing

$$\hat{\sigma}_{i,j}^2 = \frac{\Delta_i^{-1}}{n_i - 2} \sum_k \left[\log \left[\frac{f_i(\lambda_{i,k})}{F_j(\lambda_{i,k})} \right] - A + \frac{E_{B-V}^h R_{\lambda_{i,k}}}{2.5} \right]^2. \quad (\text{G1})$$

Here A is a constant accounting for differences in SN distances and photosphere radius sizes, and R_λ is the extinction curve for the host-galaxy dust along the line of sight. The best estimation for E_{B-V}^h is that provided by the $\{f_i, F_j\}$ combination with the lowest $\hat{\sigma}_{i,j}$ value.

In this work we use the D13 and L17 spectral models as $\{F_j\}$, and adopt the extinction curve of Fitzpatrick (1999) with $R_V = 3.1$. For an input SN we select spectra: (1) earlier than 40 d since the explosion, (2) with a minimum wavelength coverage of 360–700 nm, and (3) with differences between synthetic and observed colours lower than 0.1 mag. These criteria are such that the selected spectra are suitable to measure E_{B-V}^h with an error of 0.05 mag (e.g. Olivares E. et al. 2010). To be conservative, we adopt an error of 0.1 mag. For example, Fig. G1 shows the $\{f_i, F_j\}$ combination for SN 2009N that minimizes equation (G1). For that SN we compute $E_{B-V}^h = 0.202$ mag.

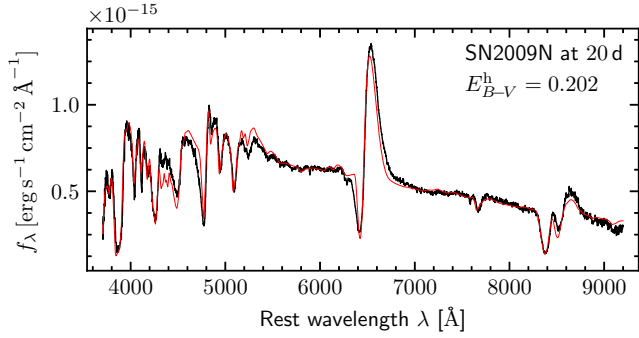


Figure G1. Spectrum of SN 2009N (corrected for E_{B-V}^G and $z_{\text{helio}}^{\text{SN}}$, black line) and model (reddened for $E_{B-V}^h = 0.202$ mag, red line) that minimizes equation (G1).

APPENDIX H: MAGNITUDE TRANSFORMATIONS

We present magnitude transformations between Sloan and Johnson–Kron–Cousins filters, and between r_{ZTF} and R . All magnitudes are corrected for E_{B-V}^G , E_{B-V}^h , and K -correction, while reported uncertainties are 1σ errors.

Using 12 SNe in our set having VRI and ri photometry in the radioactive tail (see Table L1), we find that $r-R$ and $i-I$ have a small linear dependence on $V-I$, i.e.,

$$c_y = a + b(V-I), \quad (\text{H1})$$

where $c_y = r-R, i-I$. Fig. H1 shows the mean $r-R$ ($\langle r-R \rangle$) and $i-I$ ($\langle i-I \rangle$) values of each SN as a function of the mean $V-I$ ($\langle V-I \rangle$). The average of equation (H1) is $\langle c_y \rangle = a + b\langle V-I \rangle$, so we can compute a and b fitting a straight line to the data plotted in the figure. We obtain

$$r-R = 0.17(V-I) - 0.03 \pm 0.08 \quad (\text{H2})$$

and

$$i-I = 0.12(V-I) + 0.38 \pm 0.10. \quad (\text{H3})$$

Using the same technique for $V-R$ versus $V-I$ during the photospheric phase (69 SNe, Fig. H1), we obtain

$$V-R = 0.59(V-I) + 0.05 \pm 0.05. \quad (\text{H4})$$

To convert r to R magnitudes near the maximum light, we use 18 SNe with rR photometry at $\Delta t < 20$ d (see Table L1). We find that $r-R$ is consistent with a constant value of $r-R = 0.12 \pm 0.08$ mag (see Fig. H2(a)).

To compute conversions between magnitudes at $\Delta t = 50$ d we use 18, 25, and 24 SNe for g/V , r/R , and i/I transformations, respectively. We find $(g-V)_{50\text{d}} = -0.20 + 0.61(B-V)_{50\text{d}} \pm 0.06$ (see Fig H2(b)), while the $(r-R)_{50\text{d}}$ and $(i-I)_{50\text{d}}$ values are consistent with constant values of 0.13 ± 0.05 and 0.39 ± 0.06 , respectively (see Fig H2(c)-(d)).

The public ZTF photometry is not in the SDSS photometric system but in the native ZTF one, so we cannot just adopt $r_{\text{ZTF}} = r$. To assess how similar the r_{ZTF} photometry is to the r - and R -band photometry, we compute synthetic magnitudes (Appendix A) using SN spectra. From the spectra of the SNe in our set, we select those having differences between synthetic and observed $V-r$, $V-R$, $V-i$, and/or $V-I$ colours lower than 0.1 mag.

The left-hand panels of Fig. H3 show the $r_{\text{ZTF}}-r$ (top panel) and $r_{\text{ZTF}}-R$ (bottom panel) values, computed with

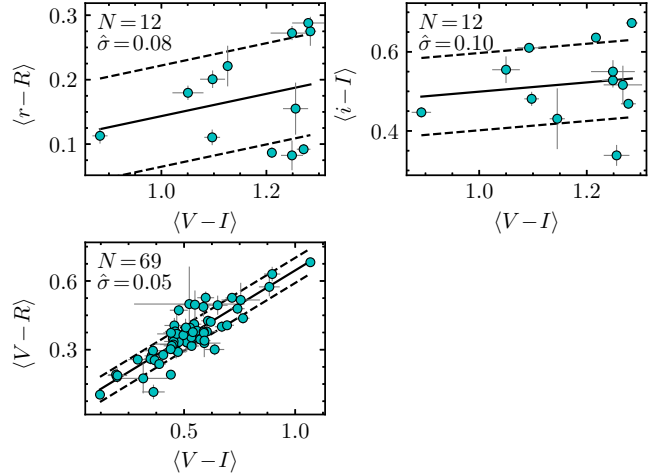


Figure H1. Upper-left (upper-right) panel: mean $r-R$ ($i-I$) against mean $V-I$ for 12 normal SNe II during the radioactive tail. Bottom panel: mean $V-R$ versus mean $V-I$ for 69 normal SNe II during the photospheric phase. Solid and dashed lines are straight line fits and $\pm 1\sigma$ limits, respectively. Error bars are 1σ errors.

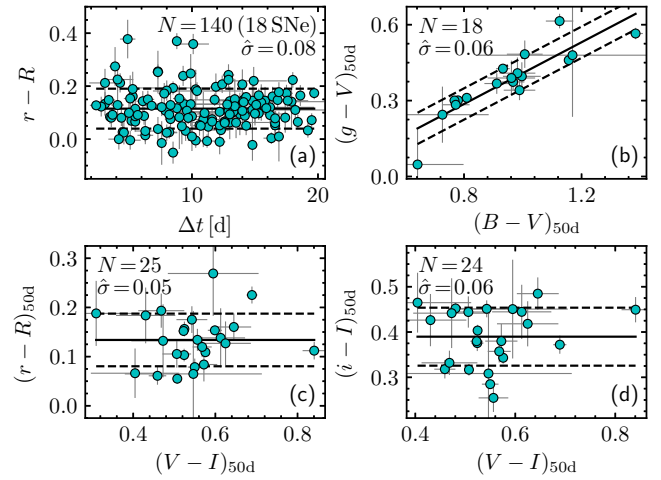


Figure H2. Panel (a): $r-R$ versus time since explosion for $\Delta t < 20$ d. Panel (b): $g-V$ against $B-V$ at $\Delta t = 50$ d. Panels (c) and (d): $r-R$ and $i-I$ versus $V-I$ at $\Delta t = 50$ d, respectively. Solid and dashed lines are the best fits and the $\pm 1\sigma$ limits, respectively. Error bars are 1σ errors.

308 spectra of 36 SNe during the photospheric and transition phase, against the time since explosion. We see that the $r_{\text{ZTF}}-R$ values have a lower dependence on time and a lower scatter than the $r_{\text{ZTF}}-r$ estimates (the y -axis scale is the same in the two panels). Therefore, the r_{ZTF} light curves during the photospheric and transition phase are more similar to the R -band light curves than the r -band ones. Given the low $\hat{\sigma}$ value (0.008 mag) around the mean $r_{\text{ZTF}}-R$ (0.138 mag), we consider the time dependence to be negligible and adopt $r_{\text{ZTF}}-R = 0.138 \pm 0.008$ mag to transform r_{ZTF} into R magnitudes. We find similar results for the radioactive tail (right-hand panels, using 56 spectra of 13 SNe), for which we adopt $r_{\text{ZTF}}-R = 0.142 \pm 0.024$ mag.

In the literature we find only one normal SN II having r_{ZTF} and R photometry (SN 2018aoq; Tsvetkov et al. 2019).

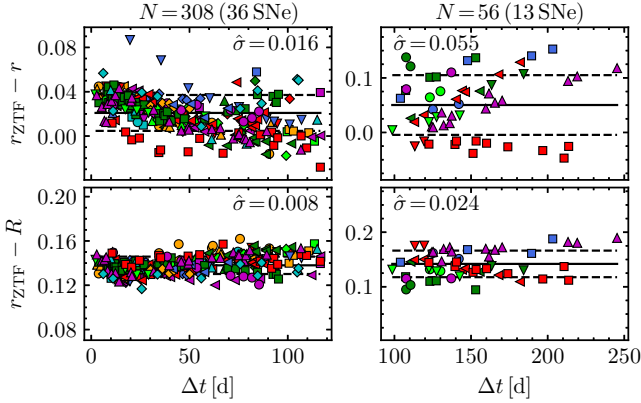


Figure H3. $r_{\text{ZTF}} - r$ (top panels) and $r_{\text{ZTF}} - R$ (bottom panels) values computed from spectra of normal SNe II in the photospheric and transition phase (left-hand panels) and in the radioactive tail phase (right-hand panels), against the time since explosion. Solid and dashed lines are mean values and $\pm 1\sigma$ limits, respectively.

For that SN we measure a mean $r_{\text{ZTF}} - R$ of 0.17 ± 0.04 mag (16 points in the photospheric phase), which is consistent within its error with our result from synthetic magnitudes.

APPENDIX I: K-CORRECTIONS

We express the x -band K -correction ($K_{x,j}$) such that the apparent magnitude ($m_{x,j}$) corrected for K -correction is $m_{x,j}^K = m_{x,j} - K_{x,j}$, where

$$K_{x,j} = -2.5 \log(1 + z_{\text{helio}}^{\text{SN}}) + k_{x,j}^s, \quad (11)$$

being

$$k_{x,j}^s = 2.5 \log \left(\frac{d\lambda S_{x,\lambda} \lambda f_{j,\lambda}}{d\lambda' S_{x,\lambda'} \lambda' f_{j,\lambda'}} \right) \quad (12)$$

and $\lambda' = \lambda / (1 + z_{\text{helio}}^{\text{SN}})$. To compute $k_{x,j}^s$ we use the spectral models of D13, J14, and L17, and $z_{\text{helio}}^{\text{SN}}$ values uniformly distributed between 0.001 and 0.043. Expressing k_x^s as polynomials on Δt , we obtain

$$k_{x,j}^s = \left(\sum_{i=0} k_i \cdot \left[\frac{\Delta t_j}{100 \text{ d}} \right]^i \pm \hat{\sigma} \right) z_{\text{helio}}^{\text{SN}}. \quad (13)$$

Table II lists the parameters for the photospheric and radioactive tail phase. At $\Delta t = 200$ d (the midpoint of the time range we use to estimate $M_{56\text{Ni}}$) K_x values are < 0.03 mag for $z_{\text{helio}}^{\text{SN}} = 0.009$ (the median redshift in our set), while for $z_{\text{helio}}^{\text{SN}} > 0.02$ (15 out of 110 SNe in our sample) K_x values start to be comparable to the typical photometry errors.

APPENDIX J: INDIRECT STEEPNESS VALUE

In order to calculate S_x indirectly from steepnesses in bands other than x , we compute steepness transformations.

Fig. J1 shows S_V against the steepness for $grRiI$ bands. Using the model selection procedure (Appendix C), we find that the five correlations plotted in the figure are well represented by straight lines. In general, for the 30 possible combinations with the $gVrRiI$ bands, we find that correlations between the x - and b -band steepness are given by

$$S_x = c_{x,b} + d_{x,b} S_b. \quad (J1)$$

Table II. K -correction parameters.

x	k_0^*	k_1^*	k_2^*	$\hat{\sigma}^*$	k_0^\dagger	k_1^\dagger	$\hat{\sigma}^\dagger$
B	-1.50	19.8	-10.8	1.32	–	–	–
g	-1.23	16.1	-10.2	0.90	–	–	–
V	-1.46	8.85	-5.27	0.66	8.10	-1.69	2.97
r	-0.05	6.56	-4.12	0.72	4.12	0.88	2.21
r_{ZTF}	-0.70	4.21	-2.54	0.24	0.60	0.77	1.22
R	-0.42	3.56	-2.09	0.21	1.48	0.57	0.92
i	-1.05	2.33	-0.87	0.37	1.05	0.26	1.00
I	-1.00	3.60	-1.50	0.24	6.31	-1.69	1.07

Note. Parameters for the photospheric (*) and radioactive tail (†) phase.

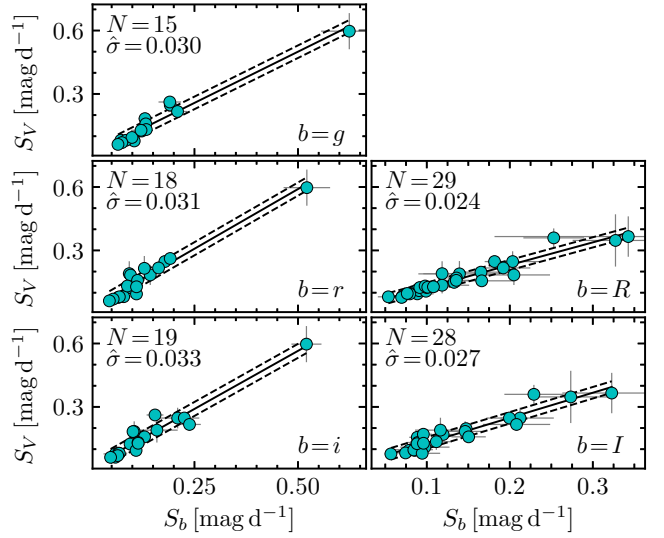


Figure J1. V -band steepness against the steepness for the $grRiI$ bands. Solid lines are straight-line fits to the data, while dashed ones are $\pm 1\sigma$ limits around the fits. Error bars are 1σ errors.

Table L8 reports the $c_{x,b}$ and $d_{x,b}$ parameters, their bootstrap errors, and the $\hat{\sigma}_{x,b}$ values.

For an SN with a set of n steepness estimates, $\{S_b\}_{b \neq x}$, we can compute a set of n S_x values, $\{S_x\}$, using equation (J1). Our best indirect measurement of S_x will be the weighted mean of the $\{S_x\}$ values, S_x^* , given by

$$S_x^* = \frac{1}{\sum_{b \neq x} w_{x,b}} \sum_{b \neq x} (c_{x,b} + d_{x,b} S_b) w_{x,b}, \quad (J2)$$

where $w_{x,b} = [d_{x,b}^2 \sigma_{S_b}^2 + \hat{\sigma}_{x,b}^2]^{-1}$. The error on S_x^* is simply

$$\sigma_{S_x^*} = \sqrt{\frac{1}{\sum_{b \neq x} w_{x,b}}}. \quad (J3)$$

APPENDIX K: REFERENCE LIST FOR THE DATA

Here the references for Tables L1, L2, L3, and L4.

- (1) Barbon et al. (1982); (2) Buta (1982); (3) Tsvetkov (1983); (4) Pennypacker et al. (1989); (5) Ruiz-Lapuente et al. (1990); (6) Benetti et al. (1991); (7) Turatto et al. (1993); (8) Schmidt et al. (1993); (9) Benetti et al. (1994); (10) Cappellaro et al. (1995); (11) Blanton et al. (1995); (12) Galbany et al. (2016); (13) Clocchiatti et al. (1996); (14) Pastorello et al. (2004); (15) Inserra et al. (2013); (16) Benetti et al. (2001); (17)

Elmhamdi et al. (2003a); (18) Krisciunas et al. (2009); (19) Faran et al. (2014a); (20) Rubenstein (1999); (21) Pastorello et al. (2009b); (22) Leonard et al. (2002); (23) Pozzo et al. (2006); (24) Tsvetkov et al. (2007); (25) Spiro et al. (2014); (26) Hendry et al. (2005); (27) Faran et al. (2014b); (28) Gurugubelli et al. (2008); (29) Zhang et al. (2006); (30) Vinkó et al. (2006); (31) Vinkó et al. (2009); (32) Meikle et al. (2011); (33) Anderson et al. (2014); (34) Sahu et al. (2006); (35) Misra et al. (2007); (36) Maguire et al. (2010); (37) Arcavi et al. (2012); (38) Tsvetkov et al. (2006); (39) Dessart et al. (2008); (40) Pastorello et al. (2009a); (41) Hicken et al. (2017); (42) Brown et al. (2009); (43) Andrews et al. (2011); (44) Andrews et al. (2010); (45) Inserra et al. (2011); (46) de Jaeger et al. (2019); (47) Van Dyk et al. (2012); (48) Van Dyk (2013); (49) Pignata (2013); (50) Roy et al. (2011a); (51) Roy et al. (2011b); (52) Takáts et al. (2014); (53) Tsvetkov (2014); (54) Inserra et al. (2012); (55) Elias-Rosa et al. (2011); (56) Takáts et al. (2015); (57) Fraser et al. (2011); (58) Rubin et al. (2016); (59) Tomasella et al. (2013); (60) Bayless et al. (2013); (61) Bose et al. (2013); (62) Munari et al. (2013); (63) Dall’Ora et al. (2014); (64) Barbarino et al. (2015); (65) Tomasella et al. (2018); (66) Bose et al. (2015a); (67) Zhang et al. (2014); (68) Valenti et al. (2016); (69) Valenti et al. (2015); (70) Richmond (2014); (71) Bose et al. (2015b); (72) Huang et al. (2015); (73) Dhungana et al. (2016); (74) Yuan et al. (2016); (75) Bullivant et al. (2018); (76) Bose et al. (2016); (77) Terreran et al. (2016); (78) Huang et al. (2016); (79) Dastidar et al. (2021); (80) Singh et al. (2018); (81) Wyrzykowski et al. (2014); (82) Dastidar et al. (2019); (83) Dastidar et al. (2018); (84) Bostroem et al. (2019); (85) Huang et al. (2018); (86) Bose et al. (2019); (87) Müller-Bravo et al. (2020); (88) Nakaoka et al. (2018); (89) Hosseinzadeh et al. (2018); (90) Singh et al. (2019); (91) Tartaglia et al. (2018); (92) Afsariardchi et al. (2019); (93) Tartaglia et al. (2021); (94) Rho et al. (2018); (95) Tsvetkov et al. (2018); (96) Tinyanont et al. (2019); (97) Van Dyk et al. (2019); (98) Szalai et al. (2019); (99) Buta & Keel (2019); (100) Andrews et al. (2019); (101) Dong et al. (2020); (102) Reguitti et al. (2021); (103) Anand et al. (2018); (104) de Jaeger et al. (2020); (105) Riess et al. (2016); (106) McQuinn et al. (2017); (107) Freedman et al. (2019); (108) Saha et al. (2006); (109) Carlin et al. (2016); (110) Monachesi et al. (2016); (111) Zgirski et al. (2017); (112) Jang & Lee (2017); (113) Rizzi et al. (2007); (114) Tikhonov & Galazutdinova (2020); (115) Hamuy (2001); (116) Rodríguez et al. (2014); (117) Olivares E. et al. (2010); (118) Turatto et al. (1998); (119) Pastorello et al. (2006); (120) Quimby et al. (2007); (121) Li et al. (2007); (122) Yaron et al. (2017); (123) Childress et al. (2016); (124) Thompson (1982); (125) Gutiérrez et al. (2017a); (126) Harutyunyan et al. (2008); (127) Hendry et al. (2006); (128) Shivvers et al. (2017); (129) Liao et al. (2019); (130) Itagaki (2016); (131) Dimai (2016); (132) Wiggins (2017).

APPENDIX L: TABLES

This paper has been typeset from a $\text{\TeX}/\text{\LaTeX}$ file prepared by the author.

Table L1. SN sample.

SN	Host galaxy	E_{B-V}^G (mag)	$cz_{\text{helio}}^{\text{SN}}$ (km s^{-1})	μ (mag)	E_{B-V}^H (mag)	t_0 (MJD)	References
1980K	NGC 6946	0.291	40	29.44 ± 0.09	-0.106 ± 0.084	44528.2 ± 5.9	1, 2, 3
1986I	M99	0.034	2407	30.71 ± 0.40	0.212 ± 0.142	46556.4 ± 1.9	4
1988A	M58	0.035	1517	31.17 ± 0.35	0.090 ± 0.111	47176.2 ± 0.3	5, 6, 7
1990E	NGC 1035	0.022	1362	30.83 ± 0.26	0.598 ± 0.072	47934.4 ± 1.4	8, 9
1990K	NGC 150	0.012	1584	31.57 ± 0.24	0.227 ± 0.034	48013.8 ± 4.2	10
1991G	NGC 4088	0.017	757	30.76 ± 0.17	0.025 ± 0.071	48281.5 ± 5.3	11
1991al	LEDA 140858	0.044	4572	32.80 ± 0.12	0.067 ± 0.026	48446.7 ± 3.7	12
1992H	NGC 5377	0.015	1793	32.07 ± 0.17	0.167 ± 0.123	48656.4 ± 4.5	13
1992ba	NGC 2082	0.050	1135	30.78 ± 0.29	0.096 ± 0.029	48886.1 ± 2.8	12
1994N	UGC 5695	0.032	2940	33.24 ± 0.20	0.045 ± 0.036	49453.9 ± 4.5	14
1995ad [†]	NGC 2139	0.029	1837	32.24 ± 0.18	0.090 ± 0.111	49972.0 ± 4.2	15
1996W	NGC 4027	0.036	1617	31.86 ± 0.19	0.260 ± 0.054	50180.2 ± 2.5	15
1997D	NGC 1536	0.017	1217	30.93 ± 0.25	0.090 ± 0.111	50361.0 ± 15.0	16
1999ca	NGC 3120	0.094	2791	32.82 ± 0.11	0.076 ± 0.033	51273.4 ± 2.9	12
1999em [†]	NGC 1637	0.035	800	30.31 ± 0.09	0.082 ± 0.034	51474.5 ± 2.0	12, 17, 18, 19
1999ga	NGC 2442	0.173	1466	31.51 ± 0.05	0.511 ± 0.084	51419.5 ± 20.0	20, 21
1999gi	NGC 3184	0.014	503	30.40 ± 0.18	0.250 ± 0.033	51518.6 ± 1.8	19, 22
2001X	NGC 5921	0.034	1480	31.52 ± 0.21	0.063 ± 0.031	51963.6 ± 2.6	19
2001dc	NGC 5777	0.009	2145	32.69 ± 0.16	0.694 ± 0.076	52046.0 ± 5.0	14
2002gw	NGC 922	0.016	3143	32.98 ± 0.22	0.138 ± 0.036	52554.8 ± 3.0	12
2002hh	NGC 6946	1.065	110	29.44 ± 0.09	1.545 ± 0.182	52575.6 ± 2.5	23, 24
2002hx	PGC 23727	0.045	9299	35.53 ± 0.08	0.140 ± 0.043	52580.3 ± 3.7	12
2003B	NGC 1097	0.023	1141	30.62 ± 0.25	0.023 ± 0.033	52622.2 ± 4.2	12
2003T	UGC 4864	0.027	8368	35.33 ± 0.10	0.154 ± 0.040	52652.6 ± 4.6	12
2003Z	NGC 2742	0.033	1289	31.62 ± 0.23	0.109 ± 0.050	52665.1 ± 2.4	19, 25
2003fb	UGC 11522	0.155	5081	34.05 ± 0.13	0.371 ± 0.046	52779.0 ± 4.4	12
2003gd	M74	0.060	657	29.95 ± 0.08	0.144 ± 0.040	52716.5 ± 21.0	12, 19, 26
2003hd	ESO 543-G17	0.011	12031	35.97 ± 0.08	0.124 ± 0.042	52857.2 ± 2.8	12
2003hk	NGC 1085	0.032	6880	34.77 ± 0.12	0.142 ± 0.054	52868.3 ± 2.7	12, 27
2003hn [†]	NGC 1448	0.012	1305	31.31 ± 0.04	0.169 ± 0.040	52865.6 ± 4.0	12, 18
2003ho	ESO 235-G58	0.033	4091	33.70 ± 0.18	0.640 ± 0.050	52848.5 ± 3.3	12
2003iq	NGC 772	0.062	2331	32.41 ± 0.16	0.122 ± 0.038	52919.4 ± 0.9	12, 19
2004A	NGC 6207	0.013	852	30.87 ± 0.26	0.177 ± 0.043	53012.5 ± 1.7	28
2004dj [†]	NGC 2403	0.034	221	27.46 ± 0.11	0.094 ± 0.035	53180.6 ± 15.6	29, 30, 31, 32
2004eg	UGC 3053	0.390	2414	32.46 ± 0.24	0.160 ± 0.150	53169.5 ± 30.0	25
2004ej	NGC 3095	0.060	2723	32.76 ± 0.13	0.145 ± 0.116	53231.5 ± 4.2	33
2004et [†]	NGC 6946	0.293	40	29.44 ± 0.09	0.073 ± 0.043	53270.5 ± 0.3	19, 34, 35, 36
2004fx	MCG -02-14-3	0.088	2673	32.73 ± 0.19	0.090 ± 0.115	53305.1 ± 1.4	33
2005af	NGC 4945	0.159	563	27.75 ± 0.12	0.090 ± 0.117	53320.8 ± 17.0	33
2005au	NGC 5056	0.010	5592	34.43 ± 0.12	0.117 ± 0.073	53441.4 ± 6.1	37
2005ay	NGC 3938	0.018	850	30.68 ± 0.21	0.035 ± 0.037	53450.7 ± 1.8	19, 38
2005cs ^{†*}	M51a	0.032	463	29.67 ± 0.07	0.124 ± 0.037	53548.4 ± 0.3	19, 38, 39, 40
2005dx	ESO 550-G2	0.021	8012	35.09 ± 0.09	0.090 ± 0.142	53615.7 ± 4.6	33
2006my	NGC 4651	0.012	788	31.40 ± 0.10	-0.062 ± 0.152	53942.5 ± 20.0	36
2006ov [†]	M61	0.019	1566	31.40 ± 0.63	0.275 ± 0.105	53973.5 ± 6.0	25, 41
2007aa	NGC 4030	0.023	1574	31.99 ± 0.27	0.046 ± 0.100	54131.9 ± 4.1	33, 41, 42
2007hv	UGC 2858	0.418	5054	34.05 ± 0.16	0.000 ± 0.100	54346.6 ± 2.8	41
2007it	NGC 5530	0.099	1193	30.56 ± 0.24	0.109 ± 0.111	54348.0 ± 0.6	33, 43
2007od	UGC 12846	0.031	1734	31.63 ± 0.25	0.134 ± 0.070	54388.2 ± 4.1	41, 44, 45, 46
2008K	ESO 504-G4	0.033	7964	35.29 ± 0.10	0.090 ± 0.111	54466.8 ± 4.8	33
2008M	ESO 121-G26	0.039	2192	32.62 ± 0.20	0.090 ± 0.112	54475.3 ± 3.3	33
2008aw	NGC 4939	0.035	3110	33.19 ± 0.17	0.226 ± 0.043	54519.3 ± 3.9	33
2008bk [†]	NGC 7793	0.017	230	27.66 ± 0.08	0.090 ± 0.111	54547.1 ± 2.6	47, 48, 49
2008gz	NGC 3672	0.036	1862	32.22 ± 0.15	-0.031 ± 0.040	54693.5 ± 5.0	50
2008in ^{††*}	M61	0.019	1566	31.40 ± 0.63	0.037 ± 0.044	54824.2 ± 0.1	41, 46, 51
2009N ^{†*}	NGC 4487	0.018	905	30.90 ± 0.38	0.265 ± 0.045	54850.1 ± 3.4	41, 46, 52
2009at	NGC 5301	0.015	1503	31.82 ± 0.22	0.551 ± 0.079	54899.1 ± 2.0	46
2009ay	NGC 6479	0.034	6650	34.74 ± 0.13	0.252 ± 0.087	54898.3 ± 4.4	41, 46, 53
2009bw [†]	UGC 2890	0.197	1155	31.07 ± 0.26	0.160 ± 0.049	54916.5 ± 3.0	54
2009dd	NGC 4088	0.017	757	30.76 ± 0.17	0.285 ± 0.057	54916.0 ± 4.2	15, 41
2009hd	M66	0.029	727	30.15 ± 0.07	1.206 ± 0.056	55001.6 ± 3.9	55
2009ib*	NGC 1559	0.026	1304	31.41 ± 0.05	0.147 ± 0.038	55040.3 ± 4.0	56
2009md [†]	NGC 3389	0.023	1308	32.06 ± 0.12	0.165 ± 0.048	55161.9 ± 7.9	57
2010aj	MCG -01-32-35	0.029	6497	34.78 ± 0.12	0.082 ± 0.048	55261.8 ± 3.5	15, 41
PTF10gva	NSA 49030	0.026	8253	35.33 ± 0.10	0.111 ± 0.111	55320.3 ± 0.9	58
2011fd	NGC 2273B	0.063	2101	32.41 ± 0.22	0.090 ± 0.111	55777.9 ± 4.5	46
PTF11go	MCG +09-19-105	0.010	8037	35.22 ± 0.10	0.160 ± 0.150	55570.9 ± 1.4	58
PTF11htj	SDSS J211603.12+123124.4	0.060	5096	34.04 ± 0.15	0.160 ± 0.150	55751.9 ± 1.5	58
PTF11lzt	anonymous	0.047	5996	34.52 ± 0.11	0.160 ± 0.150	55766.8 ± 1.3	58
2012A*	NGC 3239	0.027	753	30.66 ± 0.24	0.040 ± 0.049	55929.3 ± 2.6	46, 59
2012aw*	M95	0.024	778	29.93 ± 0.05	0.115 ± 0.041	56002.0 ± 0.5	46, 60, 61, 62, 63
2012br	SDSS J122417.04+185529.4	0.031	6805	34.90 ± 0.12	0.199 ± 0.260	56000.9 ± 0.2	58
2012cd	CGCG 271-34	0.025	3525	33.54 ± 0.19	0.123 ± 0.134	56019.4 ± 1.9	58
2012ec ^{††*}	NGC 1084	0.023	1407	31.07 ± 0.25	0.102 ± 0.048	56144.5 ± 3.4	46, 64
PTF12grj	WISEA J012039.07+044621.5	0.024	10193	35.62 ± 0.09	0.160 ± 0.150	56123.4 ± 0.6	58
PTF12hsx	SDSS J005503.33+421954.0	0.079	5696	34.34 ± 0.14	0.167 ± 0.221	56113.0 ± 0.5	58
2013K	ESO 9-G10	0.122	2418	32.48 ± 0.21	0.512 ± 0.066	56294.5 ± 4.2	65
2013ab ^{†*}	NGC 5669	0.023	1368	31.38 ± 0.20	0.028 ± 0.040	56339.6 ± 0.6	46, 66
2013am*	M65	0.021	1114	30.36 ± 0.29	0.536 ± 0.069	56371.8 ± 0.4	46, 65, 67
2013bu	NGC 7331	0.078	440	30.84 ± 0.10	0.523 ± 0.062	56396.6 ± 2.0	46, 68

Table L1 – *continued*

SN	Host galaxy	E_{B-V}^G (mag)	$cz_{\text{helio}}^{\text{SN}}$ (km s^{-1})	μ (mag)	E_{B-V}^h (mag)	t_0 (MJD)	References
2013by	ESO 138-G10	0.188	1144	30.46 ± 0.29	0.196 ± 0.100	56401.6 ± 3.6	69
2013ej ^{†‡*}	M74	0.060	657	29.95 ± 0.08	0.044 ± 0.040	56496.8 ± 0.2	46, 70, 71, 72, 73, 74
2013fs*	NGC 7610	0.035	3554	33.32 ± 0.18	0.027 ± 0.037	56570.8 ± 0.5	68, 75
2013hj	MCG -02-24-3	0.045	2072	32.51 ± 0.13	0.047 ± 0.039	56636.8 ± 0.9	76
iPTF13dkz	SDSS J013611.64+333703.6	0.039	4797	33.85 ± 0.17	0.144 ± 0.180	56547.9 ± 0.3	58
LSQ13dpa	LCSB S1492O	0.032	7045	35.00 ± 0.11	0.160 ± 0.150	56642.2 ± 2.0	68
2014G ^{†‡*}	NGC 3448	0.010	1160	31.96 ± 0.14	0.268 ± 0.046	56669.3 ± 0.8	46, 76, 77
2014cx ^{†*}	NGC 337	0.096	1646	31.51 ± 0.22	-0.021 ± 0.045	56901.9 ± 0.3	78
2014cy*	NGC 7742	0.048	1663	31.54 ± 0.23	0.090 ± 0.045	56899.6 ± 0.7	46, 68, 79
2014dw	NGC 3568	0.092	2444	32.39 ± 0.13	0.182 ± 0.127	56957.5 ± 10.0	68
ASASSN-14dq [†]	UGC 11860	0.060	3125	32.97 ± 0.21	0.108 ± 0.038	56841.0 ± 5.5	80
ASASSN-14ha	NGC 1566	0.008	1504	30.86 ± 0.15	0.090 ± 0.111	56909.5 ± 0.6	68
OGLE14-18	ESO 87-G3	0.049	8082	35.18 ± 0.10	0.144 ± 0.137	56701.7 ± 0.9	81
2015V	UGC 11000	0.031	1369	31.63 ± 0.22	0.031 ± 0.060	57112.3 ± 4.3	46
2015W	UGC 3617	0.118	3984	33.70 ± 0.19	0.157 ± 0.063	57015.0 ± 6.5	46, 68
2015an	IC 2367	0.009	2448	32.79 ± 0.13	0.114 ± 0.111	57268.0 ± 1.6	82
2015ba	IC 1029	0.015	2383	32.80 ± 0.16	0.416 ± 0.047	57347.5 ± 4.9	83
2015cz	NGC 582	0.045	4352	33.68 ± 0.16	0.472 ± 0.065	57290.4 ± 7.5	79
ASASSN-15oz	LEDA 4614833	0.078	2078	31.90 ± 0.26	0.230 ± 0.056	57259.1 ± 1.9	84
2016X ^{†*}	UGC 8041	0.019	1321	31.32 ± 0.34	0.079 ± 0.049	57405.9 ± 0.3	46, 85, 86
2016aqf	NGC 2101	0.047	1204	31.01 ± 0.25	0.180 ± 0.100	57442.6 ± 0.3	87
2016bkv*	NGC 3184	0.014	592	30.40 ± 0.18	0.036 ± 0.078	57467.5 ± 1.2	88, 89
2016gfy	NGC 2276	0.086	2416	32.64 ± 0.22	0.163 ± 0.045	57641.3 ± 2.6	90
2016ija	NGC 1532	0.013	1040	30.55 ± 0.17	1.950 ± 0.150	57712.1 ± 1.0	91
2017it	anonymous	0.029	12891	36.21 ± 0.07	-0.087 ± 0.042	57746.2 ± 0.7	92
2017ahn	NGC 3318	0.067	2775	32.84 ± 0.10	0.233 ± 0.148	57791.8 ± 0.5	93
2017eaw ^{†‡*}	NGC 6946	0.293	40	29.44 ± 0.09	0.059 ± 0.037	57886.2 ± 0.6	94, 95, 96, 97, 98, 99
2017gmr ^{†‡*}	NGC 988	0.023	1510	31.08 ± 0.19	0.332 ± 0.045	57999.2 ± 0.6	100
2018cuf	IC 5092	0.028	3248	33.10 ± 0.19	0.221 ± 0.100	58291.8 ± 0.3	101
2018hwm	IC 2327	0.022	2684	33.08 ± 0.19	0.150 ± 0.069	58424.8 ± 0.9	102

Notes. Column 1: SN names. Column 2: SN host galaxy names. Column 3: Galactic colour excesses with random errors of 16 per cent. Column 4: heliocentric SN redshifts. Column 5 and 6: host galaxy distance moduli and colour excesses, respectively. Column 7: explosion epochs. Column 8: references for the photometry (codes are in Appendix K).

[†]Selected to compute BCs.

[‡]With *VRI* and *ri* photometry in the radioactive tail.

*Used to compute $r-R$ for $\Delta t < 20$ d.

Table L2. Host galaxy distance moduli. The full table is available online as supplementary data.

Host galaxy	SN	μ_{CPL}	μ_{TRGB}	μ_{TF}	μ_{HLL}	μ_{SVF}	μ
NGC 6946	1980K	–	29.44 ± 0.09^{103}	–	–	–	29.44 ± 0.09
	2002hh	–	–	–	–	–	29.44 ± 0.09
	2004et	–	–	–	–	–	29.44 ± 0.09

Notes. Column 1: SN host galaxy names. Column 2: SN names, Columns 3 and 4: Cepheids and TRGB distances from the literature, respectively. Column 5: Tully-Fisher distances from EDD. Column 6: distances compute with the Hubble-Lemaître law. Column 6: distances inferred from smoothed velocity fields (Kourkchi et al. 2020). Column 8: adopted distance moduli. References for the data (superscript numbers) are in Appendix K.

Table L3. Host galaxy colour excesses. The full table is available online as supplementary data.

SN	$E_{B-V}^{\text{h,C3}}$	$E_{B-V}^{\text{h,V-I}}$	$E_{B-V}^{\text{h,spec}}$	$E_{B-V}^{\text{h,NaID}}$	E_{B-V}^{h}
1980K	-0.106 ± 0.084	–	–	–	0.106 ± 0.084
1986I	–	–	–	0.122 ± 0.090^4	0.212 ± 0.142
1988A	–	–	–	0.000 ± 0.014^{115}	0.090 ± 0.111

Notes. Column 1: SN names. Column 2: $E_{B-V}^{\text{h,C3}}$ values computed with the C3 method. Column 3: $E_{B-V}^{\text{h,V-I}}$ values measured with the *V-I* colour method. Column 4: $E_{B-V}^{\text{h,spec}}$ computed with the spectrum-fitting technique. Column 5: $E_{B-V}^{\text{h,NaID}}$ values estimated from the pEW of the host galaxy NaID line. Column 6: adopted host galaxy colour excesses. References for the data (superscript numbers) are in Appendix K.

Table L4. SN explosion epochs. The full table is available online as supplementary data.

SN	t_{ln} (MJD)	t_{fd} (MJD)	t_0 (MJD)	Phase source	Spectral source
1980K	44494.0	44540.0	44528.2 ± 5.9	124, IAUC 3532	WISeREP
1986I	–	46558.0	46556.4 ± 1.9	IAUC 4219	4
1988A	47175.7	47176.8	47176.2 ± 0.3	IAUC 4533, IAUC 4540	125

Notes. Column 1: SN names. Column 2 and 3: SN last non-detection and first detection epochs, respectively. Column 4: explosion epochs estimated with the SNII_ETOS code ($\pm 1 \sigma$ error), unless otherwise noted. Column 5: references for t_{ln} and t_{fd} . Column 6: data source of spectroscopy used to compute t_0 with the SNII_ETOS code. Reference codes are in Appendix K.

Table L5. ^{56}Ni masses and light-curve parameters.

SN	x	Range (d)	N	T_0 (d)	$\log(M_{56\text{Ni}}[\text{M}_\odot])$ (dex)	$M_{56\text{Ni}}$ (M_\odot)	$M_V^{50\text{d}}$ (mag)	ρ
1980K	V	100–285	9	–	-1.462 ± 0.147	0.03655 ± 0.01273	-17.348 ± 0.379	-0.655
1986I	I	171–213	4	–	-1.302 ± 0.198	0.05535 ± 0.02661	-16.911 ± 0.590	-0.900
1988A	R	185–189	3	–	-1.109 ± 0.185	0.08519 ± 0.03800	-16.488 ± 0.488	-0.930
1990E	I	141–300	7	–	-1.383 ± 0.123	0.04309 ± 0.01245	-16.702 ± 0.341	-0.899
1990K	R	100–223	7	222	-1.470 ± 0.118	0.03516 ± 0.00973	-16.705 ± 0.275	-0.810
1991G	I	135–303	7	–	-1.778 ± 0.099	0.01711 ± 0.00395	-15.365 ± 0.277	-0.798
1991al	I	101–129	4	–	-1.629 ± 0.068	0.02379 ± 0.00375	-15.974 ± 0.159	-0.670
1992H	V	140–292	7	–	-0.788 ± 0.178	0.17721 ± 0.07579	-17.670 ± 0.413	-0.899
1992ba	I	150–197	3	–	-1.744 ± 0.126	0.01881 ± 0.00557	-15.733 ± 0.305	-0.925
1994N	R	260–290	3	–	-2.283 ± 0.106	0.00537 ± 0.00133	-14.955 ± 0.233	-0.801
1995ad	I	104–229	7	258	-1.230 ± 0.115	0.06099 ± 0.01644	-17.086 ± 0.387	-0.858
1996W	I	250–309	3	–	-0.952 ± 0.097	0.11451 ± 0.02590	-17.469 ± 0.256	-0.823
1997D	I	125–176	6	–	-2.064 ± 0.144	0.00912 ± 0.00311	$< -14.436 \pm 0.423$	-0.824
1999ca	I	203–223	7	–	-1.846 ± 0.070	0.01444 ± 0.00234	-16.804 ± 0.167	-0.644
1999em	I	132–311	11	–	-1.296 ± 0.062	0.05110 ± 0.00733	-16.692 ± 0.138	-0.661
1999ga	I	121–196	3	–	-1.446 ± 0.120	0.03720 ± 0.01048	$< -16.693 \pm 0.285$	-0.497
1999gi	I	133–177	7	186	-1.333 ± 0.087	0.04739 ± 0.00959	-16.250 ± 0.207	-0.845
2001X	I	123–144	4	–	-1.395 ± 0.097	0.04129 ± 0.00934	-16.348 ± 0.231	-0.877
2001dc	I	119–153	7	–	-2.119 ± 0.110	0.00785 ± 0.00202	-15.059 ± 0.283	-0.709
2002gw	I	137–153	3	–	-1.631 ± 0.103	0.02406 ± 0.00579	-16.017 ± 0.246	-0.869
2002hh	I	167–286	14	–	-1.082 ± 0.069	0.08385 ± 0.01341	-16.882 ± 0.285	-0.611
2002hx	I	96–160	7	–	-1.186 ± 0.064	0.06587 ± 0.00976	-16.671 ± 0.165	-0.612
2003B	I	223–282	3	–	-2.223 ± 0.115	0.00620 ± 0.00167	-14.768 ± 0.271	-0.876
2003T	V	121–137	3	–	-1.344 ± 0.101	0.04653 ± 0.01097	-16.674 ± 0.164	-0.595
2003Z	I	151–208	3	–	-2.262 ± 0.116	0.00567 ± 0.00154	-14.610 ± 0.277	-0.821
2003fb	V	116–147	5	–	-1.482 ± 0.111	0.03406 ± 0.00885	-16.016 ± 0.206	-0.725
2003gd	I	128–301	17	303	-1.694 ± 0.099	0.02076 ± 0.00480	$< -16.405 \pm 0.149$	-0.407
2003hd	I	104–138	4	–	-1.362 ± 0.063	0.04391 ± 0.00640	-17.056 ± 0.156	-0.629
2003hk	R	117–145	3	–	-1.572 ± 0.105	0.02759 ± 0.00677	-17.101 ± 0.211	-0.635
2003hn	I	121–151	8	187	-1.412 ± 0.056	0.03905 ± 0.00506	-16.819 ± 0.136	-0.514
2003ho	R	102–118	3	–	-1.601 ± 0.105	0.02580 ± 0.00633	-16.554 ± 0.267	-0.717
2003iq	I	120–126	3	–	-1.318 ± 0.082	0.04895 ± 0.00933	-16.763 ± 0.200	-0.817
2004A	I	122–241	21	–	-1.604 ± 0.116	0.02579 ± 0.00701	-15.898 ± 0.291	-0.913
2004dj	I	131–284	17	–	-1.902 ± 0.130	0.01311 ± 0.00401	-15.846 ± 0.178	-0.320
2004eg	I	150–203	4	–	-2.126 ± 0.188	0.00822 ± 0.00373	$< -15.077 \pm 0.551$	-0.744
2004ej	V	120–194	14	–	-1.793 ± 0.166	0.01733 ± 0.00687	-16.494 ± 0.380	-0.881
2004et	I	135–319	23	372	-1.037 ± 0.071	0.09307 ± 0.01532	-17.645 ± 0.213	-0.759
2004fx	V	109–161	24	–	-1.802 ± 0.173	0.01708 ± 0.00708	-15.720 ± 0.400	-0.906
2005af	V	123–162	20	234	-1.477 ± 0.179	0.03630 ± 0.01562	$< -15.212 \pm 0.383$	-0.836
2005au	I	102–137	5	–	-1.195 ± 0.085	0.06506 ± 0.01286	-17.291 ± 0.273	-0.718
2005ay	R	117–236	5	–	-1.778 ± 0.109	0.01721 ± 0.00439	-15.512 ± 0.239	-0.828
2005cs	I	150–311	18	–	-2.241 ± 0.076	0.00583 ± 0.00103	-15.371 ± 0.133	-0.474
2005dx	V	103–120	3	–	-2.064 ± 0.194	0.00954 ± 0.00448	-15.583 ± 0.445	-0.878
2006my	I	177–261	8	–	-1.674 ± 0.141	0.02233 ± 0.00745	$< -15.361 \pm 0.473$	-0.768
2006ov	I	145–231	9	–	-2.051 ± 0.267	0.01074 ± 0.00728	$< -16.568 \pm 0.707$	-0.961
2007aa	i	106–121	7	–	-1.522 ± 0.143	0.03174 ± 0.01074	-16.556 ± 0.407	-0.907
2007hv	i	113–131	6	–	-1.326 ± 0.125	0.04920 ± 0.01446	-16.698 ± 0.400	-0.887
2007it	I	137–312	7	–	-0.987 ± 0.130	0.10776 ± 0.03299	-17.400 ± 0.417	-0.899
2007od	I	239–316	3	–	$> -2.482 \pm 0.148$	$> 0.00349 \pm 0.00123$	-17.438 ± 0.332	-0.713
2008K	V	122–182	4	–	-1.611 ± 0.180	0.02669 ± 0.01155	-16.806 ± 0.378	-0.713
2008M	V	96–120	5	–	-1.605 ± 0.172	0.02686 ± 0.01107	-16.504 ± 0.396	-0.900
2008aw	V	103–133	5	117	-1.074 ± 0.114	0.08729 ± 0.02331	-17.228 ± 0.230	-0.700
2008bk	I	175–292	5	–	-2.064 ± 0.094	0.00883 ± 0.00193	-14.992 ± 0.366	-0.806
2008gz	I	127–273	26	–	-1.253 ± 0.081	0.05683 ± 0.01069	$< -16.366 \pm 0.194$	-0.784
2008in	I	113–152	9	–	-1.640 ± 0.258	0.02733 ± 0.01778	-16.134 ± 0.644	-0.979
2009N	I	109–191	23	–	-1.891 ± 0.161	0.01377 ± 0.00528	-15.357 ± 0.404	-0.951
2009at	I	115–142	3	–	-1.750 ± 0.115	0.01842 ± 0.00496	-16.153 ± 0.332	-0.841
2009ay	R	100–178	8	–	-0.932 ± 0.116	0.12120 ± 0.03296	-17.720 ± 0.309	-0.790
2009bw	I	138–235	10	236	-1.737 ± 0.120	0.01904 ± 0.00536	-16.393 ± 0.316	-0.897
2009dd	R	139–298	6	–	-1.474 ± 0.112	0.03471 ± 0.00910	-16.385 ± 0.259	-0.716
2009hd	I	158–271	5	220	-1.959 ± 0.066	0.01112 ± 0.00170	-16.632 ± 0.188	-0.677
2009ib	R	149–262	4	–	-1.356 ± 0.075	0.04472 ± 0.00778	-15.790 ± 0.131	-0.524
2009md	I	123–180	4	–	-2.097 ± 0.078	0.00813 ± 0.00147	-15.365 ± 0.195	-0.689
2010aj	I	95–107	4	–	-2.088 ± 0.075	0.00829 ± 0.00144	-16.764 ± 0.203	-0.690
PTF10gva	r	175–213	3	–	-1.111 ± 0.138	0.08146 ± 0.02655	–	–
2011fd	I	126–260	12	292	-1.498 ± 0.125	0.03311 ± 0.00973	–	–
PTF11go	R	97–160	15	–	-1.593 ± 0.160	0.02732 ± 0.01042	–	–
PTF11htj	r	133–173	6	–	-1.309 ± 0.175	0.05324 ± 0.02236	–	–
PTF11lizt	R	111–182	49	–	-1.651 ± 0.159	0.02388 ± 0.00905	–	–
2012A	I	125–310	9	–	-1.766 ± 0.111	0.01771 ± 0.00460	-16.454 ± 0.284	-0.888
2012aw	I	221–309	22	537	-1.269 ± 0.055	0.05426 ± 0.00690	-16.847 ± 0.135	-0.602
2012br	R	99–263	37	–	-1.219 ± 0.254	0.07166 ± 0.04576	–	–
2012cd	r	108–216	6	228	-1.038 ± 0.168	0.09874 ± 0.03967	–	–
2012ec	I	111–163	8	–	-1.545 ± 0.115	0.02953 ± 0.00796	-16.336 ± 0.290	-0.891
PTF12grj	r	107–139	6	–	-1.565 ± 0.169	0.02937 ± 0.01187	–	–
PTF12hsx	R	135–223	575	–	-1.090 ± 0.225	0.09296 ± 0.05158	–	–
2013K	R	211–303	5	–	-1.593 ± 0.123	0.02657 ± 0.00768	-16.711 ± 0.297	-0.851
2013ab	I	107–218	19	312	-1.482 ± 0.095	0.03376 ± 0.00747	-16.199 ± 0.234	-0.867
2013am	I	230–314	5	–	-1.695 ± 0.163	0.02166 ± 0.00842	-15.470 ± 0.358	-0.743
2013bu	I	130–281	9	–	-1.888 ± 0.093	0.01324 ± 0.00287	-16.104 ± 0.217	-0.604

Table L5 – *continued*

SN	x	Range (d)	N	T_0 (d)	$\log(M_{56\text{Ni}}[M_\odot])$ (dex)	$M_{56\text{Ni}}$ (M_\odot)	$M_V^{50\text{d}}$ (mag)	ρ
2013by	<i>i</i>	104–153	10	176	-1.512 ± 0.151	0.03268 ± 0.01171	-17.397 ± 0.436	-0.902
2013ej	<i>I</i>	107–226	107	172	-1.551 ± 0.060	0.02839 ± 0.00394	-16.950 ± 0.149	-0.675
2013fs	<i>r</i>	102–107	4	–	-1.323 ± 0.106	0.04897 ± 0.01213	-16.739 ± 0.213	-0.762
2013hj	<i>I</i>	117–168	19	–	-1.092 ± 0.073	0.08206 ± 0.01389	-17.564 ± 0.178	-0.767
iPTF13dkz	<i>r</i>	152–174	5	–	-1.173 ± 0.205	0.07506 ± 0.03750	–	–
LSQ13dpa	<i>i</i>	144–152	3	–	-1.101 ± 0.135	0.08317 ± 0.02649	-17.181 ± 0.470	-0.913
2014G	<i>I</i>	95–165	30	127	-1.146 ± 0.077	0.07258 ± 0.01297	-17.203 ± 0.199	-0.793
2014cx	<i>I</i>	120–150	10	–	-1.251 ± 0.103	0.05771 ± 0.01388	-16.668 ± 0.263	-0.884
2014cy	<i>R</i>	128–164	4	113	-1.820 ± 0.117	0.01569 ± 0.00431	-15.584 ± 0.269	-0.861
2014dw	<i>r</i>	97–143	18	85	-1.544 ± 0.158	0.03053 ± 0.01149	-16.238 ± 0.487	-0.734
ASASSN-14dq	<i>I</i>	108–204	10	266	-1.308 ± 0.101	0.05055 ± 0.01192	-16.967 ± 0.249	-0.826
ASASSN-14ha	<i>i</i>	140–181	18	–	-2.030 ± 0.120	0.00970 ± 0.00273	-15.963 ± 0.369	-0.859
OGLE14-18	<i>I</i>	182–235	6	–	-1.367 ± 0.123	0.04471 ± 0.01292	–	–
2015V	<i>I</i>	124–217	33	–	-1.643 ± 0.107	0.02345 ± 0.00587	-15.751 ± 0.287	-0.871
2015W	<i>i</i>	253–289	4	–	-1.372 ± 0.110	0.04385 ± 0.01129	-17.129 ± 0.314	-0.714
2015an	<i>i</i>	148–218	13	–	-1.575 ± 0.113	0.02752 ± 0.00728	-17.184 ± 0.363	-0.873
2015ba	<i>i</i>	166–259	3	–	-1.840 ± 0.114	0.01496 ± 0.00400	-17.020 ± 0.221	-0.613
2015cz	<i>I</i>	125–143	4	–	-1.344 ± 0.093	0.04634 ± 0.01004	-17.158 ± 0.272	-0.750
ASASSN-15oz	<i>i</i>	185–261	18	126	-0.875 ± 0.124	0.13890 ± 0.04048	-17.682 ± 0.316	-0.887
2016X	<i>I</i>	98–196	37	205	-1.349 ± 0.147	0.04741 ± 0.01652	-16.856 ± 0.371	-0.937
2016aqf	<i>i</i>	154–307	11	332	-1.670 ± 0.137	0.02247 ± 0.00727	-16.024 ± 0.394	-0.902
2016bkv	<i>I</i>	202–307	29	–	-1.817 ± 0.106	0.01570 ± 0.00389	-14.537 ± 0.300	-0.800
2016gfy	<i>I</i>	122–238	11	307	-1.122 ± 0.103	0.07766 ± 0.01868	-17.145 ± 0.263	-0.883
2016ija	<i>i</i>	96–105	6	–	-1.582 ± 0.144	0.02766 ± 0.00943	-16.691 ± 0.490	-0.916
2017it	<i>I</i>	118–135	18	–	-1.257 ± 0.060	0.05587 ± 0.00776	-16.817 ± 0.149	-0.626
2017ahn	<i>i</i>	101–142	5	98	-1.316 ± 0.132	0.05059 ± 0.01574	-16.751 ± 0.464	-0.914
2017eaw	<i>I</i>	128–313	136	–	-1.087 ± 0.069	0.08289 ± 0.01325	-17.265 ± 0.203	-0.752
2017gmr	<i>I</i>	103–146	6	–	-0.857 ± 0.093	0.14222 ± 0.03081	-17.655 ± 0.235	-0.852
2018cuf	<i>i</i>	123–273	18	–	-1.417 ± 0.121	0.03980 ± 0.01131	-16.898 ± 0.359	-0.877
2018hwm	<i>r</i>	171–191	3	–	-2.205 ± 0.124	0.00650 ± 0.00189	-15.041 ± 0.284	-0.822

Notes. Column 1: SN names. Column 2, 3, and 4: bands, phase ranges, and number of points used to compute $\log M_{56\text{Ni}}$, respectively. Column 5: γ -ray escape times. Column 6 and 7: derived $\log M_{56\text{Ni}}$ and $M_{56\text{Ni}}$ values. Column 8: Absolute V-band magnitudes at 50 d since explosion. Column 9: correlation coefficients between $\log M_{56\text{Ni}}$ and $M_V^{50\text{d}}$.

Table L6. M_R^{max} value for the LOSS set and our SN sample.

SN [†]	M_R^{max} (mag)	SN [‡]	M_R^{max} (mag)	SN [‡]	M_R^{max} (mag)	SN [‡]	M_R^{max} (mag)	SN [‡]	M_R^{max} (mag)
1999an	-16.931	1980K	-18.764	2003hk	-18.303	2009ay	-18.552	LSQ13dpa	-17.694
1999bg	-16.473	1986I	-16.730	2003hn	-17.602	2009bw	-17.309	2014G	-18.411
1999br	-15.526	1988A	-16.639	2003ho	-17.415	2009dd	-16.993	2014cx	-16.957
1999em	-17.192	1990E	-17.401	2003iq	-17.347	2009hd	-17.327	2014cy	-16.122
1999gi	-16.728	1990K	-17.784	2004A	-16.159	2009ib	-16.266	2014dw	-17.312
2000dc	-17.921	1991G	-15.729	2004dj	-16.232	2009md	-15.779	ASASSN-14dq	-17.653
2000el	-16.312	1991al	-16.836	2004eg	-15.693	2010aj	-17.836	ASASSN-14ha	-16.379
2001bq	-17.577	1992H	-18.067	2004ej	-17.026	PTF10gva	-18.794	OGLE14-18	-17.103
2001dc	-15.283	1992ba	-16.218	2004et	-17.974	2011fd	-16.998	2015V	-15.970
2001fz	-15.865	1994N	-15.371	2004fx	-15.984	PTF11go	-16.743	2015W	-17.893
2002bx	-16.901	1995ad	-17.782	2005af	-17.413	PTF11htj	-16.946	2015an	-17.697
2002ce	-15.319	1996W	-17.798	2005au	-17.974	PTF11izt	-16.348	2015ba	-17.750
2002dq	-16.232	1997D	-14.986	2005ay	-15.912	2012A	-17.176	2015cz	-17.627
2002ds	-17.197	1999ca	-18.086	2005cs	-15.700	2012aw	-17.181	ASASSN-15oz	-18.478
2002gd	-15.939	1999em	-17.192	2005dx	-16.381	2012br	-17.764	2016X	-17.588
2002hh	-17.107	1999ga	-17.320	2006my	-16.896	2012cd	-18.680	2016aqf	-16.136
2003Z	-14.958	1999gi	-16.728	2006ov	-16.195	2012ec	-16.695	2016bkv	-15.741
2003ao	-16.339	2001X	-16.726	2007aa	-16.703	PTF12grj	-16.963	2016gfy	-17.599
2003hl	-17.364	2001dc	-15.283	2007hv	-17.158	PTF12hsx	-17.331	2016ija	-17.238
2003iq	-17.347	2002gw	-16.310	2007it	-18.234	2013K	-16.430	2017it	-17.178
2004et	-17.974	2002hh	-17.107	2008K	-17.869	2013ab	-16.804	2017ahn	-18.286
2004fc	-16.642	2002hx	-17.596	2008M	-17.236	2013am	-15.958	2017eaw	-17.828
2004fx	-15.984	2003B	-15.248	2008aw	-18.181	2013bu	-16.947	2017gmr	-18.005
2005ad	-15.882	2003T	-17.131	2008bk	-15.245	2013by	-18.411	2018cuf	-17.224
2005ay	-15.912	2003Z	-14.958	2008gz	-17.679	2013ej	-17.900	2018hwm	-15.191
2006be	-16.972	2003fb	-16.582	2008in	-16.596	2013fs	-17.623	–	–
2006bp	-17.622	2003gd	-16.859	2009N	-15.609	2013hj	-18.270	–	–
2006ca	-17.202	2003hd	-17.635	2009at	-17.283	iPTF13dkz	-16.470	–	–

[†]LOSS set. Original M_R^{max} values (listed in Li et al. 2011) were recalibrated using E_{B-V}^G values from Schlafly & Finkbeiner (2011), μ estimates listed in Column 8 of Table L2, and E_{B-V}^h values reported in Column 6 of Table L3.

[‡]Our SN sample.

Table L7. Steepness parameters. The full table is available online as supplementary data.

SN	S_g	S_V	S_r	S_R	S_i	S_I	S_g^*	S_V^*	S_r^*	S_R^*	S_i^*	S_I^*
1980K	–	0.159(39)	–	–	–	–	0.149(49)	–	0.118(42)	0.134(40)	0.131(44)	0.125(37)
1991G	–	0.120(46)	–	0.089(18)	–	0.069(20)	0.109(14)	0.104(23)	0.080(14)	0.083(26)	0.086(24)	0.090(22)
1992ba	–	0.098(23)	–	–	–	0.082(25)	0.102(21)	0.108(40)	0.076(19)	0.084(23)	0.081(26)	0.079(28)

Notes. Steepness values are in mag d^{-1} units. Numbers in parentheses are 1σ errors in units of the last significant digits.
 *Values estimated from the steepnesses in other bands (see Section 4.5).

Table L8. S_b to S_x transformation parameters.

x	b	$c_{x,b}$ (mag d^{-1})	$d_{x,b}$	$\hat{\sigma}_{x,b}$ (mag d^{-1})	N	x	b	$c_{x,b}$ (mag d^{-1})	$d_{x,b}$	$\hat{\sigma}_{x,b}$ (mag d^{-1})	N
g	V	-0.008 ± 0.027	0.986 ± 0.208	0.030	15	V	g	0.015 ± 0.033	0.969 ± 0.272	0.030	15
g	r	0.004 ± 0.015	1.161 ± 0.145	0.021	15	V	r	0.026 ± 0.018	1.129 ± 0.157	0.031	18
g	R	0.042 ± 0.006	0.817 ± 0.056	0.012	8	V	R	0.017 ± 0.008	1.072 ± 0.075	0.024	29
g	i	-0.000 ± 0.025	1.118 ± 0.227	0.030	15	V	i	0.016 ± 0.010	1.099 ± 0.045	0.033	19
g	I	0.054 ± 0.016	0.677 ± 0.089	0.020	8	V	I	0.011 ± 0.011	1.187 ± 0.093	0.027	28
r	g	-0.001 ± 0.008	0.842 ± 0.017	0.018	15	R	g	-0.041 ± 0.010	1.146 ± 0.063	0.014	8
r	V	-0.014 ± 0.023	0.832 ± 0.162	0.027	18	R	V	-0.002 ± 0.010	0.853 ± 0.077	0.022	29
r	R	0.026 ± 0.011	0.686 ± 0.114	0.015	10	R	r	-0.015 ± 0.020	1.256 ± 0.198	0.021	10
r	i	-0.001 ± 0.020	0.939 ± 0.184	0.031	17	R	i	0.039 ± 0.024	0.680 ± 0.123	0.037	11
r	I	0.022 ± 0.011	0.717 ± 0.081	0.015	10	R	I	0.002 ± 0.009	1.053 ± 0.067	0.025	28
i	g	0.007 ± 0.024	0.853 ± 0.201	0.027	15	I	g	-0.040 ± 0.035	1.189 ± 0.199	0.027	8
i	V	-0.004 ± 0.009	0.848 ± 0.051	0.029	19	I	V	0.005 ± 0.010	0.755 ± 0.072	0.022	28
i	r	0.011 ± 0.010	0.986 ± 0.029	0.032	17	I	r	-0.009 ± 0.017	1.203 ± 0.145	0.020	10
i	R	0.022 ± 0.029	0.872 ± 0.291	0.042	11	I	R	0.012 ± 0.008	0.855 ± 0.055	0.022	28
i	I	0.000 ± 0.016	1.037 ± 0.109	0.028	11	I	i	0.024 ± 0.015	0.792 ± 0.084	0.024	11

Notes. $S_x = c_{x,b} + d_{x,b}S_b$.

Table L9. Absolute magnitudes at 50 d since explosion. The full table is available online as supplementary data.

SN	M_g^{50d}	M_r^{50d}	M_R^{50d}	M_i^{50d}	M_I^{50d}
1980K	$-17.099 \pm 0.429^*$	$> -18.255 \pm 0.270^*$	$> -18.385 \pm 0.253$	$> -17.897 \pm 0.219^*$	$> -18.287 \pm 0.194$
1986I	–	$-16.490 \pm 0.548^*$	-16.619 ± 0.532	$-16.739 \pm 0.489^*$	-17.129 ± 0.471
1990E	–	$-17.084 \pm 0.324^*$	-17.214 ± 0.314	$-16.915 \pm 0.302^*$	-17.304 ± 0.289

*Values estimated using photometry in other bands (see Section 4.6).

Table L10. SZB sample.

IAU SN	E_{B-V}^G (mag)	$c_{\text{helio}}^{\text{SN}}$ (km s^{-1})	μ (mag)	t_0 (MJD)	M_R^{max} (mag)	$M_{r_{\text{ZTF}}}^{50d}$ (mag)	$S_{r_{\text{ZTF}}}$ (mag d^{-1})	$\log M_{56\text{Ni}}^{\text{NMS}}$ (dex)	$\log M_{56\text{Ni}}^{\text{tail}}$ (dex)
2018ccb	0.139	4740	33.90 ± 0.12	58267.9 ± 1.4	-17.313	-16.67 ± 0.39	0.116 ± 0.009	-1.505 ± 0.145	-1.399 ± 0.162
2018fpx	0.210	7500	35.03 ± 0.09	58356.6 ± 4.0	< -18.246	-17.75 ± 0.39	0.059 ± 0.011	-1.033 ± 0.153	-0.971 ± 0.161
2018hcp	0.030	5934	34.59 ± 0.11	58377.0 ± 1.5	-17.381	-16.94 ± 0.39	0.055 ± 0.004	-1.218 ± 0.144	-1.215 ± 0.160
2019va	0.016	2637	33.03 ± 0.19	58497.6 ± 3.1	-17.488	-17.20 ± 0.41	0.065 ± 0.004	-1.205 ± 0.148	-0.962 ± 0.170
2019vb	0.011	6039	34.60 ± 0.12	58500.6 ± 1.0	-18.469	-17.88 ± 0.39	0.074 ± 0.011	-1.069 ± 0.149	-0.872 ± 0.160
2019clp	0.031	7127	35.01 ± 0.11	58569.0 ± 0.5	-18.490	-17.66 ± 0.39	0.068 ± 0.009	-1.103 ± 0.147	-1.074 ± 0.158
2019cvz	0.011	5578	34.39 ± 0.13	58577.6 ± 1.0	-17.282	-17.09 ± 0.39	0.076 ± 0.008	-1.274 ± 0.146	-1.177 ± 0.162
2019dma	0.113	4880	33.89 ± 0.15	58560.2 ± 6.4	< -17.395	-17.22 ± 0.41	0.143 ± 0.017	-1.426 ± 0.150	-1.585 ± 0.167
2019dtl	0.056	4673	33.86 ± 0.15	58584.2 ± 5.3	< -17.051	-16.88 ± 0.40	0.096 ± 0.012	-1.397 ± 0.149	-1.279 ± 0.165
2019etp	0.044	4683	33.77 ± 0.16	58607.2 ± 2.7	< -17.788	-17.45 ± 0.40	0.048 ± 0.004	-1.054 ± 0.147	-1.065 ± 0.165
2019ffn	0.102	7800	35.09 ± 0.11	58616.9 ± 0.4	-18.300	-17.81 ± 0.39	0.071 ± 0.003	-1.078 ± 0.143	-1.039 ± 0.159
2019gqk	0.079	3900	33.35 ± 0.19	58625.6 ± 4.9	< -16.894	-16.69 ± 0.42	0.056 ± 0.004	-1.288 ± 0.149	-1.247 ± 0.171
2019hhh	0.281	4500	33.72 ± 0.17	58635.4 ± 4.5	-17.059	-16.69 ± 0.42	0.081 ± 0.004	-1.395 ± 0.149	-1.254 ± 0.172
2019hkh	0.071	5400	34.17 ± 0.15	58620.6 ± 9.1	< -17.051	-16.87 ± 0.40	0.103 ± 0.008	-1.421 ± 0.146	-1.332 ± 0.167
2019iex	0.063	4211	33.54 ± 0.19	58658.9 ± 1.5	-17.503	-17.21 ± 0.41	0.173 ± 0.012	-1.486 ± 0.149	-1.339 ± 0.171
2019jyw	0.029	3489	33.16 ± 0.21	58659.5 ± 2.9	-17.850	-17.03 ± 0.43	0.070 ± 0.004	-1.269 ± 0.150	-1.140 ± 0.174
2019lhx	0.454	3000	32.81 ± 0.23	58677.0 ± 1.5	-17.220	-16.85 ± 0.47	0.052 ± 0.002	-1.229 ± 0.157	-1.224 ± 0.190
2019vus	0.025	7500	35.08 ± 0.09	58806.6 ± 1.0	< -17.374	-16.94 ± 0.38	0.057 ± 0.009	-1.224 ± 0.148	-1.174 ± 0.163
2019wvz	0.009	9571	35.61 ± 0.09	58832.5 ± 0.9	-18.031	-17.75 ± 0.38	0.071 ± 0.016	-1.086 ± 0.155	-0.878 ± 0.156
2020aem	0.034	6650	34.74 ± 0.13	58860.6 ± 6.0	-17.602	-16.87 ± 0.39	0.087 ± 0.008	-1.371 ± 0.146	-1.284 ± 0.162
2020ckb	0.075	7503	34.98 ± 0.11	58861.9 ± 4.5	< -17.867	-17.50 ± 0.39	0.159 ± 0.037	-1.383 ± 0.158	-1.188 ± 0.159
2020dpw	0.320	1424	31.68 ± 0.17	58904.8 ± 0.7	< -16.945	-16.75 ± 0.42	0.078 ± 0.004	-1.368 ± 0.150	-1.257 ± 0.174
2020dvt	0.013	4200	33.82 ± 0.18	58908.5 ± 2.0	-17.398	-16.91 ± 0.41	0.217 ± 0.023	-1.628 ± 0.150	-1.719 ± 0.168
2020ekk	0.041	4273	33.80 ± 0.16	58918.7 ± 0.6	-17.905	-17.22 ± 0.40	0.156 ± 0.020	-1.452 ± 0.150	-1.666 ± 0.165
2020gcv	0.031	8513	35.27 ± 0.10	58934.5 ± 6.5	< -17.629	-17.32 ± 0.40	0.090 ± 0.014	-1.267 ± 0.152	-1.171 ± 0.159
2020ifc	0.173	4683	33.79 ± 0.15	58930.5 ± 5.7	-15.851	-15.62 ± 0.41	0.133 ± 0.139	-1.698 ± 0.290	-1.760 ± 0.167
2020nja	0.026	5656	34.29 ± 0.15	59015.2 ± 4.9	< -16.702	-16.50 ± 0.40	0.074 ± 0.008	-1.412 ± 0.148	-1.519 ± 0.166
2020umi	0.058	5610	34.43 ± 0.15	59119.5 ± 1.0	-17.860	-17.00 ± 0.40	0.067 ± 0.018	-1.253 ± 0.163	-1.214 ± 0.169

Notes. We adopt $E_{B-V}^H = 0.16 \pm 0.15$ mag, while to estimate M_R^{max} we use $r_{\text{ZTF}} - R = 0.14$ mag.